



저작자표시-비영리-변경금지 2.0 대한민국

이용자는 아래의 조건을 따르는 경우에 한하여 자유롭게

- 이 저작물을 복제, 배포, 전송, 전시, 공연 및 방송할 수 있습니다.

다음과 같은 조건을 따라야 합니다:



저작자표시. 귀하는 원저작자를 표시하여야 합니다.



비영리. 귀하는 이 저작물을 영리 목적으로 이용할 수 없습니다.



변경금지. 귀하는 이 저작물을 개작, 변형 또는 가공할 수 없습니다.

- 귀하는, 이 저작물의 재이용이나 배포의 경우, 이 저작물에 적용된 이용허락조건을 명확하게 나타내어야 합니다.
- 저작권자로부터 별도의 허가를 받으면 이러한 조건들은 적용되지 않습니다.

저작권법에 따른 이용자의 권리는 위의 내용에 의하여 영향을 받지 않습니다.

이것은 [이용허락규약\(Legal Code\)](#)을 이해하기 쉽게 요약한 것입니다.

[Disclaimer](#)

공학박사학위논문

페로브스카이트 태양전지의 전하에 의한
열화 및 열화 해결방법 연구

Charge Induced Degradation of Perovskite Solar Cells and Its
Solution

2022년 2월

서울대학교 대학원

기계항공공학부

변준섭

페로브스카이트 태양전지의 전하에 의한 열화 및 열화 해결방법 연구

Charge Induced Degradation of Perovskite Solar Cells and Its
Solution

지도교수 최 만 수

이 논문을 공학박사 학위논문으로 제출함

2021 년 10 월

서울대학교 대학원

기계항공공학부

변 준 섭

변준섭의 공학박사 학위논문을 인준함

2021 년 12 월

위 원 장 : 이 윤 석 (인)

부위원장 : 최 만 수 (인)

위 원 : 차 석 원 (인)

위 원 : 고 승 환 (인)

위 원 : 장 세 근 (인)

Charge Induced Degradation of Perovskite Solar Cells and Its Solution

Junseop Byeon

Department of Mechanical and Aerospace Engineering

The Graduate School

Seoul National University

Abstract

Organic-inorganic lead halide perovskite solar cells have reached a power conversion efficiency of over 25% within a decade and attracted worldwide attention for next generation photovoltaics. However, there are still many issues related to operational long-term stability to overcome in perovskite solar cells. Lead halide perovskite, known as ionic crystal, are vulnerable to moisture, oxygen with the light because of weak bonding between organic and inorganic moieties. Various encapsulation techniques were used to protect the devices from the exposure of the extrinsic factors such as moisture and oxygen. However, high concentration of charge carriers is generated in solar

cells and encapsulated devices often suffer from rapid degradation under illumination conditions. These phenomena imply the irreversible degradation by intrinsic factors such as charge accumulation and charge induced state transition of ionic defects. To achieve stable operation of perovskite solar cells, it is required to understand fundamental principles of degradation mechanism by intrinsic degradation factors and to devise solutions to enhance stability of perovskite solar cells based on the understanding of degradation principle in perovskite solar cells. This dissertation aims to elucidate mechanism on charge induced degradation in perovskite solar cells and to propose novel operational technique to enhance the stability in perovskite solar cells by suppressing charges accumulation and formation of deep level defects.

First, the correlation between charges accumulation and device degradation was investigated. To investigate the correlation, perovskite solar cells with different electron transporting layer were employed. Perovskite solar cells shows a dominant p-n junction (high degree of band bending) occurred at the specific interface depending on electron transporting layers, and charge accumulation is mainly localized at the corresponding dominant junction where degradation is initiated. Profiles of vacuum level, E-field and charge density distribution with respect to electron-transporting layers were confirmed by electron beam induced current measurement and kelvin probe force microscopy. The amount of accumulated charges in devices was measured and devices with lowest charge accumulation showed better

stability. Time evolution of degradation process in aged perovskite solar cells demonstrated that high concentration of single-signed charges at the dominant p–n junction induced degradation. This study, for the first time, revealed that charges accumulated at the dominant p–n junction play a decisive role in device degradation.

Secondly, the soft ionic nature of the perovskite lattice induces low defect formation energies, resulting in high density of defects in perovskite. An electronic state of the ionic defects can be changed through charge-state transition under high carrier concentration conditions(light illumination). However, degradation mechanism originated from charge-induced transition of defects remain elusive. In this part, the photo-aging patterns of perovskite film with different native ionic defects is investigated without extrinsic degradation factors (O_2 and H_2O). Perovskite solar cells was fabricated by using precursor with different PbI_2 concentration to control self-doping, resulting in perovskite film with different native defects. After photo-aging of Pb-rich perovskite film, strain relaxation in perovskite lattice and increase of non-radiative recombination were observed, indicating the formation of new defect states in Pb-rich devices. Thermal admittance spectroscopy of the devices revealed that the transition to the deep-traps in the Pb-rich devices lead to irreversible degradation and could be related to the differences in the photo-aging patterns among solar cells with different conditions. This study suggests passivation of the deep defects induced by non-stoichiometry near the grain boundaries and the interface is crucial for perovskite solar cells with

long-term stability.

Thirdly, both accumulated charges and ionic defects has been considered as origins of degradation of perovskite solar cells. Pulsatile therapy (PT) was devised to prolong device lifetime by addressing accumulation of both charges and ionic defects during maximum power point tracking. In the technique, reverse biases are periodically applied for a very short time without any pause of operation, leading to stabilization of the working device. The efficacies of pulsatile therapy are delaying irreversible degradation as well as restoring degraded photocurrent during MPPT operation. *In-situ* photoluminescence and photocurrent measurements for the working device were carried out while applying the pulsatile therapy for studying defect formation during MPPT operation and defect healing by the pulsatile therapy. We suggest an integrated mechanism underlying the therapy, in which harmful deep-level defects can be cured by driving defect state transition. In the 500hr long-term test, we observed outstanding improvement of device stability and total harvesting power. This study notably proposes an unprecedented technical approach to heal perovskite solar cell devices quickly and prolong their lifetime without pause. Therefore, this technique could open up the possibility of perovskite solar cell commercialization to be raised to the full.

Keywords: Perovskite Solar Cell, Degradation, Charge accumulation, defect, Pulsatile therapy, defect healing

Student Number: 2015-22699

Table of Contents

Abstract	i
Table of Contents	v
List of Tables	ix
List of Figures	x
Nomenclature	xx
Chapter 1. Introduction	1
1.1. Background.....	1
1.2. Research objectives	6
1.3. Thesis outline.....	10
1.4. References	11
Chapter 2. Electron Transport Layer-Dependent Band bending in Perovskite Solar Cells and Its Correlation to Device Degradation	18
2.1. Introduction	18
2.2. Experimental Methods.....	21
2.2.1. Device Fabrication.....	21
2.2.2. Characterization.....	23

2.3. Results and discussion	25
2.3.1. Electron beam induced current measurement of devices with diffrenet charge selective layers.....	25
2.3.2. Kelvin probe forced microscopy measurement of devices ..	31
2.3.3. Device degradation characteristics of devices underlying different charge accumulation.....	41
2.3.4. Design of ideal n-i-p solar cells	47
2.4. Conclustion.....	50
2.5. Reference	51

Chapter 3. Investigation of Native Defects Induced Degradation in

Perovskite Solar Cells fabricated by using Control of Self- Doping Effect	62
3.1. Introduction	62
3.2. Experimental Methods.....	66
3.2.1. Fabrication of perovskite solar cells	66
3.2.2. Device characterization.....	67
3.2.3. Thin-film characterization	67
3.3. Results and discussion.....	70
3.3.1. The self-doping property of perovskite film.....	70
3.3.2. Analysis of photo-aging pattern in perovskit film	73
3.3.3. J-V characteristics and light stability of perovskite solar cells	80

3.3.4. Energetic distribution of defects and estimation of possible candidates of observed defect states	87
3.4. Conclusion.....	93
3.5. Reference.....	94
Chapter 4. Pulsatile Therapy for Perovskite Solar Cells with Improved Long-Term Stability.....	104
4.1. Introduction	104
4.2. Experimental Methods.....	108
4.2.1. Fabrication of perovskite solar cells.....	108
4.2.2. Charaterization.....	110
4.2.3. <i>In situ</i> photoluminescence and photocurrent systme.....	111
4.3. Results and discussion.....	112
4.3.1. Effect of electrical operating conditions on device degradation	112
4.3.2. Design of pulsatile therapy and its efficacies	116
4.3.3. Long-term effect of pulsatile therapy	128
4.3.4. Defect healing mechanism underlying pulsatile therapy.	137
4.4. Conclusion.....	141
4.5. References	142
Appendix	152
Acknowledgements.....	154

Abstract in Korean	155
List of Publications	158

List of Tables

Table 3.1. Atomic ratio between halide elements and lead (Pb) in both as prepared and photo-aged perovskite films with different PbI_2 concentration measured by XRF	79
Table 4.1 Time constant extracted from kinetics of PL intensity and PC during RP (30 sec) and MP (30 min) operation after RP, r respectively. During the RP step, both PL intensity and PC were fitted by bi-exponential function, in which the fast one resulted from capacitive current and the slow one resulted from field-induced ion	127
Table 4.2 Fitting parameters of double diode modeling for MPPT case at 100 h, 200 h and 500 h operation.	134
Table 4.3 Fitting parameters of simulated I-V curves for fresh (0hr) and 500-hour-aged PSCs under MPPT- and PT-condition	135

List of Figures

- Figure 2.1. J-V scan and parameters of the a) TiO₂-based device, b) TiO₂/C₆₀-based device, c) C₆₀-based device measured in reverse (full circle) and forward (hollow circle) scan, respectively.29
- Figure 2.2 (a) Illustration of EBIC measurement on a cross-sectional surface of a cleaved perovskite solar cell. Cross-sectional EBIC image overlaid with corresponding SEM image of (b) TiO₂-based, (c) TiO₂/C₆₀-based, and (d) C₆₀-based devices. Bright green color on the images indicate the high EBIC signal. Profiles of measured EBIC signals perpendicular to layers of the (e) TiO₂-based, (f) TiO₂/C₆₀-based, and (g) C₆₀-based devices. Scale bars: 500 nm..... 30
- Figure 2.3 (a) Illustration of KPFM measurements of cross-sectional plane in devices under operating conditions with light illumination. CPD distribution under illumination at open-circuit (OC) condition (red line) and at short-circuit (SC) condition (blue line) of (b) TiO₂-based and (e) C₆₀-based devices. The arrows in (b) and (e) indicate the open-circuit voltage(V_{OC}). Normalized E-field distribution under illumination at open-circuit condition of the (c) TiO₂-based and (f) C₆₀-based devices. Charge density profile calculated from potential difference between the open-circuit and short-circuit voltages (CPD_{OC} – CPD_{SC}) of (d) TiO₂-based and (g) C₆₀-based devices. 36

Figure 2.4. (a) The cross-sectional images of topography (Top), and the CPD distribution at short circuit state (middle) and at open circuit state (bottom) for the TiO₂-based device. (b) The cross-sectional images of topography (Top), and the CPD distribution at short circuit state (middle) and at open circuit state (bottom) for C₆₀-based device. KPFM measurement were conducted in all devices under LED light illumination.....37

Figure 2.5 Illustration of electronic band diagrams for (a) TiO₂-based devices and (b) C₆₀-based devices under light illumination in short-circuit (SC) state. Illustration of electronic band diagrams of the (c) TiO₂-based devices and (d) C₆₀-based devices under light illumination in open circuit (OC) state. Here, the red dotted line and blue dotted line indicate the quasi-Fermi level of electrons and quasi-Fermi level of holes, respectively. VL, HTL, V_{BI}, and V_{OC} indicate vacuum level, hole-transporting layer, built-in potential, open-circuit voltage, respectively.40

Figure 2.6 (a) Illustration of process of charge extraction measurements. (b) Sequence showing the relation in each process between illumination, measured potential and calculated charge in the charge extraction measurement (c) The quantity of extracted charges as a function of delay time up to 10s for the three different devices.....42

Figure 2.7 (a) The nyquist plot of perovskite solar cells depending on the kinds of ETLs. (b) an equivalent circuit we apply. (c) geometrical

capacitance and (d) capacitance of surface charge accumulation with different voltage bias. EIS measurements are conducted under LED light and ambient air condition. Here, R_s indicates ohmic resistance including contacts and wires, C_g and C_s is the capacitance of dielectric properties of the perovskite layer and the capacitance of surface charge accumulation at the interfaces, respectively. R_1, R_2 are associated with the resistance of recombination current flux. ...43

Figure 2.8 (a) Time dependent operational stability of un-encapsulated devices with respect to different ETLs under one sun illumination in ambient air. Time evolution of cross-sectional SEM images for degradation process in (b) TiO_2 -based, (c) TiO_2/C_{60} -based, and (d) C_{60} -based devices. Scale bars: 500 nm.46

Figure 2.9 Schematic illustrations of electronic band diagrams in solar cells with ideal N-I-P junction type under light illumination at a) short-circuit (SC) state and b) open-circuit (OC) state..49

Figure 3.1 TOF-SIMS depth profiles of as-prepared perovskite film with (a) 1.1 M-, (b) 1.3 M-, and (c) 1.5 M- PbI_2 condition. Dotted lines with different color indicate the location where element of corresponding dotted line decreases. (d) XPS spectra of as prepared perovskite thin film with different PbI_2 concentration (1.1 - 1.5 M). Interception of black dotted line with X-axis indicates the energy level difference between VB_M to E_F 72

Figure 3.2 XRD pattern of as-prepared and 200-hour photo-aged perovskite

films with (a) 1.1 M-, (b) 1.3 M-, and (c) 1.5 M- PbI_2 condition. Ultraviolet-visible absorption and steady state PL spectra of as-prepared and 200-hour aged perovskite films with (d) 1.1 M, (e) 1.3 M, and (f) 1.5 M- PbI_2 condition. The insets show photo-aging time dependent normalized PL peak intensity. Dark colored- and light colored- lines indicate the spectra of as-prepared and 200-hour aged PSCs, respectively..... 75

Figure 3.3 XPS spectra of as-prepared and 200-hour photo-aged perovskite films with (a) 1.1 M-, (b) 1.3 M-, and (c) 1.5 M- PbI_2 condition near the valance band (VB) region. Dark colored- and light colored- lines indicate as-prepared and 200-hour aged PSCs, respectively. Photo-aging time dependent atomic ratio of halide to Pb in perovskite with (d) 1.1 M-, (e) 1.3 M-, and (f) 1.5 M- PbI_2 condition by XRF measurement... .. 78

Figure 3.4. (a) statistical parameters of photovoltaic performance for the fabricated PSCs with different PbI_2 concentration. (b) J-V curves of best performing PSCs by reverse scan. (c) EQE spectra and related integrated short-circuit current density (J_{SC}) of PSCs with different PbI_2 condition. Colored line and dotted line indicate EQE spectra and integrated J_{SC} , respectively. (d) Operational stability of PSCs with different PbI_2 concentration under continuous 1-Sun illumination. All PSCs were encapsulated in N_2 atmosphere. 82

Figure 3.5 (a-c) Nyquist plots of the as prepared and 100-hour photo-aged

PSCs with (a) 1.1 M-, (b) 1.3 M-, and (c) 1.5 M- PbI_2 condition, respectively. Inset shows an equivalent circuit we employed. (d-f) the recombination resistance (R_{rec}) and (g-i) the geometrical capacitance (C_g) of the as-prepared and 100-hour photo-aged PSCs with (d, g) 1.1 M-, (e, h) 1.3 M-, and (f, i) 1.5 M- PbI_2 condition, respectively. 83

Figure 3.6 Cross-sectional SEM images of as-prepared PSCs with (a) 1.1 M-, (b) 1.3 M-, and (c) 1.5 M- PbI_2 condition. Cross-sectional SEM images of 200-hour photo-aged PSCs with (d) 1.1 M-, (e) 1.3 M-, and (f) 1.5 M- PbI_2 condition. The structure of PSCs is ITO/SnO₂/perovskite/Spiro-MeOTAD/Au. The thickness of SnO₂ layer, as-prepared perovskite layer, Spiro-MeOTAD layer, and Au layer are 30, 600, 200, and 50 nm, respectively. All scale bars 500 nm. 86

Figure 3.7 Mott-Schottky plots obtained from capacitance–voltage (C-V) scan for the as-prepared and 200-hour aged PSCs with (a) 1.1 M- and (b) 1.3 M- PbI_2 condition. Temperature dependent capacitance-frequency spectra (T-C-F) of (c) as-prepared and (d) 200-hour aged PSCs with 1.1M- PbI_2 condition. Temperature dependent capacitance-frequency spectra (T-C-F) of (e) as-prepared and (f) 200-hour aged PSCs with 1.3M- PbI_2 condition. 89

Figure 3.8 Arrhenius plot of characteristic transition frequencies to extract defect activation energies for as-prepared and 200-hour aged PSCs

with (a) 1.1 M- and (b) 1.3 M-PbI₂ condition. Trap-density-of-states(tDOS) profiles for as-prepared and 200-hour aged PSCs with (c) 1.1 M- and (d) 1.3 M-PbI₂ condition, showing energetic distribution of defect states in each device. Dotted lines indicate the peak of spectra. Line and symbols with dark color and light color indicate as-prepared and 200-hour aged PSCs, respectively. 90

Figure 4.1. (a) Time evolution of the normalized power of three different types of encapsulated devices measured at SC (short circuit), MPPT (maximum power point tracking) and OC (open circuit) condition under one sun illumination in ambient condition (30% of Relative humidity). I-V scans were done every five hours. (b) Time evolution of the normalized power of the device type 3 measured at four different voltage biases around MPP (maximum power point). 0.5 V (black), 0.65 V (red), 0.75 V (blue), 0.8V (green). (c) A schematic illustration describing the effect of voltage bias on charge accumulation, ion migration, and the resulting degradation. All devices were glass-encapsulated in N₂-filled glove box. 114

Figure 4.2 J-V characteristics of (a) device type 1 (ITO/C₆₀/MAPbI₃/HTL/Au) (b) device type 2 (ITO/SnO₂/MAPbI₃/HTL/Au), (b) device type 3 (ITO/SnO₂/Triple-perovskite/HTL/Au) measured under both reverse (full circle) and forward (hollow circle) scan. Spiro-MeOTAD was employed as hole transporting layers (HTLs) for all devices. Photovoltaic parameters are summarized in the bottom table... 115

Figure 4.3. (a) A schematic illustration of our novel system for pulsatile therapy and its basic algorithm. Therapy consist of I-V scans, maximum power point tracking (MPPT), and short pulsatile therapy (PT). (b) The profile of applied bias voltage and corresponding photocurrent over time stored in our system. To heal a working device, the reverse pulses ($V_{RP} = -I_{sc} \cdot R_s$) were applied during the middle of MPPT. V_{MP} : Maximum power point voltage, T_{MP} : Time duration for maximum power point voltage, V_{RP} : Reverse pulse voltage, T_{RP} : Time duration for reverse pulse voltage. I_{sc} : short-circuit current, R_s : series resistance 118

Figure 4.4. A simple equivalent circuit including a parallel capacitor corresponding accumulation of charged ones..... 119

Figure 4.5 (a) Time evolution of normalized power for MPPT (black)- and PT (red)-tested cells. Profiles of normalized power for PT- and MPPT- tested cells during (b) 2-3 h of operation time. and (c) 16-17 h of operation time. The inset image is the magnified profile of the selected region showing the effect of short pulse. In this test, the I-V sweep was done every 5 hours to update I-V characteristics of the target device. The sudden change of normalized power at around 5 h occurred due to the significant change in maximum power point of the target device. 122

Figure 4.6 (a) Time-evolution of normalized power of the $C_{60}/MAPbI_3/Spiro-$ MeOTAD device (device type 1) tested under PT (red)- and MPPT

(black)- conditions. (b)The profiles of normalized power of the $C_{60}/MAPbI_3/Spiro-MeOTAD$ device tested under PT-condition during 16-18 h of operation time. (c) Time-evolution of normalized power the $SnO_2/MAPbI_3/Spiro-MeOTAD$ device (device type 2) under PT (red)- and MPPT (black)- condition..... 123

Figure. 4.7 (a) A schematic illustration of in-situ photoluminescence (PL) and photocurrent (PC) measurements combined with the PT system. (b) Dynamics of PL intensity (black) and PC (blue) of the device operating under MPPT condition for over 4000 seconds. (c) Dynamics of PL intensity (gray) and PC (cyan) of the PT-tested device during 30 seconds of pulsatile therapy after 30 minutes of MPPT operation. Both profiles for PL intensity (black) and PC (blue) were fitted by bi-exponential components with similar time-constants. (d) Overall kinetics of PL intensity and PC during the pulsatile therapy ($V_{MP}-V_{RP}-V_{MP}$). Black and blue arrows point out restoration of PL intensity and PC, respectively, indicating device healing induced by short reverse pulses. 126

Figure. 4.8. (a) Time evolution of normalized power and total gain (violet) of the representative test set of total test sets working for 500 h under MPPT (black), PT (red) under one sun illumination. (b) A statistical plot of total test sets for relative improvements (RI) of operational stability by pulsatile therapy. A blue dashed line indicates the best-performing PT. (c) A statistical plot for total energy gain of the PT.

Total energy gain is defined as a relative improvement of total harvested energy of the PT as compared to the MPPT case. Measured I-V curves (solid lined) and simulated I-V curves of the devices tested under the MPPT operation (d) and the PT operation (e) at 0 h (black) and 500 h (blue), together with corresponding conductance-voltage curves to certify a peculiar I-V shape with two deflections. I-V simulation was conducted based on our equivalent circuit modeling. The I-V curve with two deflections (500 h, MPPT) requires double diodes for its simulation, while the other curves are simulated with a single diode..... 131

Figure 4.9 Equivalent circuit based on (a) double diode and (b) single diode modeling. I_{gen} , R_s , I_{ph} , R_{sh} , I_{sh} , and I_{d1} indicate source current, series resistance, photocurrent, shunt resistance, shunt current and diode current, respectively..... 133

Figure 4.10 (a) X-ray diffraction (XRD) patterns of the fresh (black), the 300 h PT-tested (red), and the 300 h MPPT-tested devices, respectively. Intensities are normalized to the maximal peak. (b) Magnified XRD patterns at angles corresponding to the (100) and (200) lattices of the cubic phase of the fresh (black), the 300 h PT-tested (red), and the 300 h MPPT-tested devices, respectively. Surface scanning electron microscopy (SEM) images of (c) the fresh, (d) the 300 h PT-tested, and (d) the 300 h MPPT-tested. (f) An illustration for an irreversible degradation process based on a charge-state transition of halide

defects occurring during continuous MPPT operation. The neutral interstitial defects are main sources to produce stable chemical compounds, meaning permanent material degradation. (g) An illustration to describe reversible recoveries based on healing of deep-level neutral defects toward shallow-level defects in the PT system. Periodic relaxations of localized charges and ions by reverse pulses trigger reverse charge-state transition, suppressing accumulation of deep-level defects..... 139

Nomenclature

Alphabetical

C	Capacitance
C_g	Geometrical Capacitance
C_s	Capacitance of surface charge accumulation.
CB	Conduction Band
CPD	Contact Potential Difference
d	Thickness of perovskite layer
DFE	Defect formation energy
E	Electric-field
$EBIC$	Electron beam induced current
E_{CB}	Energy level of conduction band
E_{VB}	Energy level of valence band
ETL	Electron transport layer
E_F	Fermi-level
E_A	Activation energy
E_o	Demarcation energy
FF	Fill Factor
HTL	Hole Transport layer
J_{sc}	Short Circuit Current
K	Boltzmann Constant

<i>KPFM</i>	Kelvin Probe Force Microscopy
<i>MPPT</i>	Maximum Power Point Tracking
N_t	Trap density
<i>OC</i>	Open Circuit
<i>PCE</i>	Power Conversion Efficiency
<i>PSC</i>	Perovskite Solar Cell
<i>PT</i>	Pulsatile Therapy
q	Elementary charge
<i>RP</i>	Reverse Pulse
R_{rec}	Recombination resistance
<i>SC</i>	Short Circuit
T	Temperature
<i>tDOS</i>	Trap Density of States.
V_{bi}	Built in voltage
V_{MP}	Voltage at maximum power point
V_{RP}	Voltage at reverse pulse
V_{oc}	Open Circuit Voltage
<i>VL</i>	Vacuum Level
W	Depletion width

Greek letters

ρ	Charge density
ε_0	Absolute permittivity (dielectric constant of vacuum)
ε_r	Dielectric constant of perovskite
ω	Applied angular frequency
ω_T	Characteristic transition frequencies
ν_0	Attempt to escape frequency

Chapter 1. Introduction

1.1. Background

1.1.1 Organic inorganic lead halide perovskite solar cell

Recently, as climate change due to global warming has become severe, global interest in the environment is continuously rising. Continuous usage of fossil fuels and their byproduct have caused environmental pollution such as harmful gas emission and global warming [1], many scientists have strived to develop renewable energy that can replace fossil fuels [2]. Among many candidates, solar energy has prominent advantage over others because it has infinite energy sources and does not emit harmful substances during the energy conversion process. [3,4] Solar cells have been developed in various types, such as silicon thin film [5], CIGS [6], GaAS [7], CdTE thin film solar cells [8], dye-sensitized [9] and organic solar cells [10], depending on types of active material that absorbs light.

Among the various types of solar cells, Si solar cells are representative photovoltaics as commercialized photovoltaics. However, commercialized solar cells still have disadvantage in high production cost and difficulties in applying them to flexible solar cells, limiting their various applications. [11]

Perovskite solar cells (PSCs) are in the spotlight as a next-generation

solar cell. The perovskite structure consists of ABX_3 in which organic and inorganic materials are mixed, leading to have various constitutional combinations [A =MA, FA, alkali metals, B= Pb, Sn, X= halide]. [12] The perovskite materials have superior opto-electronic properties such as tunable optical bandgap, high absorption coefficient, high carrier mobility and long carrier diffusion length. [13-16]

Unlike the existing inorganic thin film solar cells, PSCs utilize perovskite material as a light absorber which can be processed at low temperatures and can be solution processed [17], thereby allowing cost competitive and various applications of PSCs, such as to flexible solar cells [18] and semi-transparent solar cell [19]. Owing to superior properties and economic benefit, the world-wide interest on perovskite solar cell have drastically increased, and expectation of replacing expensive inorganic thin film photovoltaics have soared.

A $CH_3NH_3PbI_3$ (MAPbI₃)-based solar cells were first reported for the first time in 2009 from a group of Miyasaka. [20] However, there was a disadvantage of using perovskite as a light dye in electrolyte based on dye-sensitized solar cell, leading to reaction with the internal electrolyte and perovskite MAPbI₃ materials. In 2012, A group of Park and another group of Snaith developed a perovskite solar cell with improved efficiency and stability by replacing an electrolyte with a solid-state charge transporting layer. [21,22] Afterwards, tremendous progress on improving PSCs has been achieved. State of the art PSCs has reached 25.2% in single junction solar

cell.[23-25]

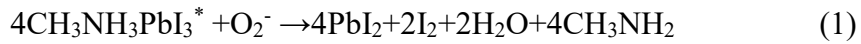
1.1.2 Device structure and fabrication of perovskite solar cells

Generally, Perovskite solar cell is n-i-p junction solar cell. PSCs have multi-layers including transparent conductive oxide (TCO) as an electrode, a n-type semiconductor as electron transport layer (ETL), perovskite as light absorber, a p-type semiconductor as hole transport layer (HTL), metal electrode. Perovskite solar cells (PSCs) can be categorized into 2 types of device structure, which depends on the direction where the device absorbs light. [26] Normal structure (n-i-p) indicates types of devices which absorb light in the direction of TCO and ETL. PSCs with normal structure consist of TCO/ETL/perovskite/HTL/metal. On the other hands, in inverted structure where devices absorb light in the direction of TCO and HTL, PSCs in inverted structure is composed of TCO/HTL/perovskite/ETL/metal. [26]

1.1.3 Oxygen and moisture stability of perovskite solar cell

Perovskite films suffer from rapid degradation when exposed to light and oxygen. [27-29] It has been studied that oxygen induced degradation is the governing process in dictating device stability compared to moisture induced degradation under ambient atmosphere. [28]. Oxygen molecules can easily diffuse into perovskite film. When the perovskite film is illuminated from

light, reactive superoxide(O_2^-) can form due to favorable transfer of electron from conduction band of the perovskite to oxygen molecules. [29] The superoxide is reactive and leads to decomposition of perovskite film. Thus, this oxide initiates decomposition of perovskite crystal lattice. MA^+ cation, water moisture, iodine, lead-iodide, and gas phase of methylamine was left as product. [29]



In terms of moisture induced degradation, it has been studied that water molecules, likewise oxygen, easily infiltrate into perovskite film. the water molecules can hydrate the perovskite crystal structure, leading to formation of an intermediate mono-hydrate phase or di-hydrate phase. [30] However, mono-hydrated and di-hydrated perovskite films stored in inert atmosphere reversibly convert back to their dehydrated phase. [30]



However, moisture induced degradation was observed in un-encapsulated perovskite solar cell stored in under high relative humidity over 50% for few hundred hours. [31-33] Water molecules have strong polarity and can interact with organic cation in perovskite due to strong hydrogen bonds, weakening

the ionic bonding between the organic cation and the inorganic PbI_6 octahedral structure [31,32]. As a result, moisture leads to fast deprotonation of the organic cation and decomposition of perovskite materials, leaving volatile hydroiodic acid (HI) and lead iodide (PbI_2). [31,32]

1.2. Research objectives

As mentioned above, perovskite solar cells have reached high certified performance around 25% comparable to commercialized Si solar cell. [25] However, operational stability issue has not been solved yet. In dissertation, deterioration of perovskite solar cells induced by photo-generated charges are investigated with respect to charges accumulation and defect formation, respectively. Furthermore, based on the understanding of charge induced degradation, the dissertation describes novel operational system which regulates dynamics of both charges and defects to enhance device stability of perovskite photovoltaics.

Firstly, presence of accumulated photo-carriers has been considered one of factors to weaken ionic bonding in perovskite film. The decomposition of polycrystalline perovskite film was initiated at grain boundaries of perovskite, attributing to charges along grain boundaries. [34] However, the effect of accumulated charges on the degradation of perovskite solar cells remains unclear. Unlike perovskite film itself, perovskite solar cells have different carrier dynamics due to introduction of charge transporting layers. In this study, perovskite solar cells with TiO_2 , C_{60} and $\text{TiO}_2/\text{C}_{60}$ bilayer were fabricated to examine effect of charge accumulation on device degradation. For TiO_2 -based device, dominant p-n junction was observed at TiO_2 /perovskite interface and large amount of positive charges mainly remains at the TiO_2 /perovskite interface, On the other hands, In C_{60} -based device,

dominant junction appeared at perovskite/spiro-MeOTAD interface and relatively small quantity of negative charges were accumulated at the corresponding dominant junction. The lifetime of the devices under light illumination was highly dependent on location of dominant p-n junction and the amount of accumulated charges at the corresponding interface. The devices with lowest charge accumulation showed better stability. This study revealed that charges accumulated at the dominant p-n junction play a decisive role in device degradation.

Secondly, perovskite materials have various unique properties. One of them is self-doping effect which indicate that the kinds of native defects in perovskite film can be tuned by controlling stoichiometry between organic and inorganic elements. [35] The another one is defect tolerant properties which shows efficient charge generation and charge transfer in pristine perovskite film despite of high trap density compared with conventional semiconductors such as Si, CdTe and GaAs films. [36,37] However, despite defect tolerant property of perovskite materials, their thin-film solar cells often exhibit rapid degradations rate in power conversion efficiencies under condition with high carrier concentration at N₂ atmosphere. The effects of charge induced transition of ionic defects on the deterioration of perovskite solar cell devices are rarely investigated. In this study, degradation mechanism of PSCs under illumination (high excess charges) is investigated, excluding extrinsic degradation factors by encapsulation and N₂-filled chamber. The perovskite films were fabricated by controlling self-doping

effect through precursors with different PbI_2 concentration. Perovskite solar cells with different PbI_2 condition show similar performance of 21%, but different degradation patterns. The relatively Pb-deficient solar cells exhibit an improved defect-tolerant property under light illumination, retaining over 90% of its initial power conversion efficiency during 500 hours of continuous 1-Sun illumination. On the contrary, the solar cells with relatively Pb-rich case show significant performance drop, combining with the result of strain relaxation and increased non-radiative recombination. Additionally, the charge induced transition to the deep-traps in the Pb-rich devices lead to irreversible degradation. This study proposed that passivation of defects induced by deep trap near grain boundaries and interface are crucial for fabrication of solar cells with long-term stability.

Lastly, operational system was developed to enhance the stability of perovskite solar cell based on the understanding of charge and ionic defects induced degradation. Pulsatile therapy (PT) was developed by mitigating the accumulation of both trapped charges and ions in the perovskite solar cell device during the middle of maximum power point tracking (MPPT) for prolonging device lifetime. In the technique, reverse biases are repeatedly applied for a very short time to eliminate the charges accumulated and re-distribute the ions migrated during power harvesting. Particularly, the therapy is not only delaying irreversible degradation, but also, restoring the degraded power right after applying reverse bias in very short time. Perovskite solar cell operated under pulsatile therapy led to improvement of total harvested

energy gain by up to 11.3% for 500 h-long operation compared to devices under conventional MPPT operation. Furthermore, all devices with different charge selective layer and different perovskite composition operated by Pulsatile therapy showed better stability. This pulsatile therapy is reported as the first technical approach to revive the device without any pause of operation, as well as effectively benefit from total harvested energy gain regardless of inherent device quality.

1.3 Thesis outline

This dissertation is organized of 4 chapters. This chapter outlines overall introduction of this thesis.

Chapter 2 focuses on the charge transporting layer dependent degradation of perovskite solar cell by electronic band bending and charge accumulation. This chapter examines appearance of dominant p-n junction, and correlation between charge accumulation at the p-n junction and device degradation.

Chapter 3 describes effect of native defects on stability of perovskite solar cells under light illumination condition with high concentration of charges. This chapter shows change of opto-electric properties and electronic structure by light exposure in perovskite solar cells. In this chapter, it also confirmed that transition to deep level defects in photo-aged devices is the main reason in dictating device stability.

Chapter 4 deals with demonstration of pulsatile therapy relieving the accumulation of both trapped charges and ions in the perovskite solar cell. This chapter describes the efficacy of pulsatile therapy and healing mechanism underlying defect physics. Model considering trap-assisted recombination support explanation on the efficacy of the therapy.

1.4 References

- [1] S. Shafiee, E. Topal, When will fossil fuel reserves be diminished?, *Energy Policy* 2009, 37, 181.
- [2] Q. Schiermeier, J. Tollefson, T. Scully, A. Witze, O. Morton, Energy alternatives: Electricity without carbon, *Nature* 2008, 454, 816.
- [3] M. Z. Jacobson, M. A. Delucchi, Providing all global energy with wind, water, and solar power, Part I: Technologies, energy resources, quantities and areas of infrastructure, and materials, *Energy Policy* 2011, 39, 1154
- [4] F. Creutzig, P. Agoston, J. C. Goldschmidt, G. Luderer, G. Nemet, R. C. Pietzcker, The underestimated potential of solar energy to mitigate climate change, *Nat. Energy* 2017, 2, 17140
- [5] K. Yoshikawa, H. Kawasaki, W. Yoshida, T. Irie, K. Konishi, K. Nakano, T. Uto, D. Adachi, M. Kanematsu, H. Uzu, K. Yamamoto, Silicon heterojunction solar cell with interdigitated back contacts for a photoconversion efficiency over 26%, *Nat. Energy* 2017, 2, 17032
- [6] M. Nakamura, K. Yamaguchi, Y. Kimoto, Y. Yasaki, T. Kato, H. Sugimoto, Cd-Free Cu(In,Ga)(Se,S)₂ Thin-Film Solar Cell With Record Efficiency of 23.35%, *IEEE Journal of Photovoltaics* 2019, 9, 1863.
- [7] W. Metaferia, K. L. Schulte, J. Simon, S. Johnston, A. J. Ptak, Gallium arsenide solar cells grown at rates exceeding 300 $\mu\text{m h}^{-1}$ by

- hydride vapor phase epitaxy, *Nat. Commun.* 2019, 10, 3361.
- [8] T. A. M. Fiducia, B. G. Mendis, K. Li, C. R. M. Grovenor, A. H. Munshi, K. Barth, W. S. Sampath, L. D. Wright, A. Abbas, J. W. Bowers, J. M. Walls, Understanding the role of selenium in defect passivation for highly efficient selenium-alloyed cadmium telluride solar cells, *Nature Energy* 2019, 4, 504.
- [9] K. Kakiage, Y. Aoyama, T. Yano, K. Oya, J. Fujisawa, M. Hanaya, Highly-efficient dye-sensitized solar cells with collaborative sensitization by silyl-anchor and carboxy-anchor dyes, *Chem Commun (Camb)* 2015, 51, 15894.
- [10] H. Chen, R. Zhang, X. Chen, G. Zeng, L. Kobera, S. Abbrent, B. Zhang, W. Chen, G. Xu, J. Oh, S.-H. Kang, S. Chen, C. Yang, J. Brus, J. Hou, F. Gao, Y. Li, Y. Li, A guest-assisted molecular-organization approach for >17% efficiency organic solar cells using environmentally friendly solvents, *Nat. Energy* 2021, 10.1038
- [11] T. Ibn-Mohammed, S. C. L. Koh, I. M. Reaney, A. Acquaye, G. Schileo, K. B. Mustapha, R. Greenough, Perovskite solar cells: An integrated hybrid lifecycle assessment and review in comparison with other photovoltaic technologies, *Renewable and Sustainable Energy Reviews* 2017, 80, 1321.
- [12] Y. Zhao, K. Zhu, Organic–inorganic hybrid lead halide perovskites for optoelectronic and electronic applications, *Chem Soc Rev* 2016, 45, 655.

- [13] G. E. Eperon, S. D. Stranks, C. Menelaou, M. B. Johnston, L. M. Herz, H. J. Snaith, Formamidinium lead trihalide: a broadly tunable perovskite for efficient planar heterojunction solar cells, *Energy Environ. Sci.* 2014, 7,982
- [14] J. H. Noh, S. H. Im, J. H. Heo, T. N. Mandal, S. I. Seok, Chemical Management for Colorful, Efficient, and Stable Inorganic– Organic Hybrid Nanostructured Solar Cells, *Nano Lett.* 2013, 13, 1764;
- [15] D. Stranks Samuel, E. Eperon Giles, G. Grancini, C. Menelaou, J. P. Alcocer Marcelo, T. Leijtens, M. Herz Laura, A. Petrozza, J. Snaith Henry, Electron-Hole Diffusion Lengths Exceeding 1 Micrometer in an Organometal Trihalide Perovskite Absorber, *Science* 2013, 342, 341;
- [16] Q. Dong, Y. Fang, Y. Shao, P. Mulligan, J. Qiu, L. Cao, J. Huang, Electron-hole diffusion lengths $>175\mu\text{m}$ in solution-grown $\text{CH}_3\text{NH}_3\text{PbI}_3$ single crystals, *Science* 2015, 347, 967.
- [17] N. J. Jeon, J. H. Noh, Y. C. Kim, W. S. Yang, S. Ryu, S. I. Seok, Solvent engineering for high-performance inorganicorganic hybrid perovskite solar cells, *Nat. Mater.* 2014, 13, 897.
- [18] G. Lee, M.-c. Kim, Y. W. Choi, N. Ahn, J. Jang, J. Yoon, S. M. Kim, J.-G. Lee, D. Kang, H. S. Jung, M. Choi, Ultra-flexible perovskite solar cells with crumpling durability: toward a wearable power source, *Energy Environ. Sci.* 2019, 12, 3182.
- [19] H. Wang, H. A. Dewi, T. M. Koh, A. Bruno, S. Mhaisalkar, N.

- Mathews, Bifacial, Color-Tunable Semitransparent Perovskite Solar Cells for Building-Integrated Photovoltaics, *ACS Appl. Mater. Interfaces* 2020, 12, 484.
- [20] A. Kojima, K. Teshima, Y. Shirai, T. Miyasaka, Organometal Halide Perovskites as Visible-Light Sensitizers for Photovoltaic Cells, *J. Am. Chem. Soc* 2009, 131, 6050.
- [21] H. S. Kim, C. R. Lee, J. H. Im, K. B. Lee, T. Moehl, A. Marchioro, S. J. Moon, R. Humphry-Baker, J. H. Yum, J. E. Moser, M. Gratzel, N. G. Park, Lead Iodide Perovskite Sensitized All-Solid-State Submicron Thin Film Mesoscopic Solar Cell with Efficiency Exceeding 9%, *Sci Rep* 2012, 2, 591;
- [22] M. Lee Michael, J. Teuscher, T. Miyasaka, N. Murakami Takuro, J. Snaith Henry, Efficient Hybrid Solar Cells Based on Meso-Superstructured Organometal Halide Perovskites, *Science* 2012, 338, 643.
- [23] J. Burschka, N. Pellet, S. J. Moon, R. Humphry-Baker, P. Gao, M. K. Nazeeruddin, M. Gratzel, Sequential deposition as a route to high-performance perovskite-sensitized solar cells, *Nature* 2013, 499, 316;
- [24] N. J. Jeon, J. H. Noh, W. S. Yang, Y. C. Kim, S. Ryu, J. Seo, S. I. Seok, Compositional engineering of perovskite materials for high-performance solar cells, *Nature* 2015, 517, 476;
- [25] J. Jeong, M. Kim, J. Seo, H. Lu, P. Ahlawat, A. Mishra, Y. Yang, M. A. Hope, F. T. Eickemeyer, M. Kim, Y. J. Yoon, I. W. Choi, B. P.

- Darwich, S. J. Choi, Y. Jo, J. H. Lee, B. Walker, S. M. Zakeeruddin, L. Emsley, U. Rothlisberger, A. Hagfeldt, D. S. Kim, M. Gratzel, J. Y. Kim, Pseudo-halide anion engineering for α -FAPbI₃ perovskite solar cells, *Nature* 2021, 592, 381.
- [26] J.-P. Correa-Baena, M. Saliba, T. Buonassisi, M. Grätzel, A. Abate, W. Tress, A. Hagfeldt, Promises and challenges of perovskite solar cells, *Science* 2017, 358, 739.
- [27] A. J. Pearson, G. E. Eperon, P. E. Hopkinson, S. N. Habisreutinger, J. T. W. Wang, H. J. Snaith, N. C. Greenham, Oxygen Degradation in Mesoporous Al₂O₃/CH₃NH₃PbI_{3-x}Cl_x Perovskite Solar Cells: Kinetics and Mechanisms, *Adv. Energy Mater.* 2016, 6.
- [28] D. Bryant, N. Aristidou, S. Pont, I. Sanchez-Molina, T. Chotchunangatchaval, S. Wheeler, J. R. Durrant, S. A. Haque, Light and oxygen induced degradation limits the operational stability of methylammonium lead triiodide perovskite solar cells, *Energy Environ. Sci.* 2016, 9, 1655.
- [29] N. Aristidou, C. Eames, I. Sanchez-Molina, X. Bu, J. Kosco, M. S. Islam, S. A. Haque, Fast oxygen diffusion and iodide defects mediate oxygen-induced degradation of perovskite solar cells, *Nat. Commun.* 2017, 8, 15218.
- [30] A. M. A. Leguy, Y. Hu, M. Campoy-Quiles, M. I. Alonso, O. J. Weber, P. Azarhoosh, M. van Schilfgaarde, M. T. Weller, T. Bein, J. Nelson, P. Docampo, P. R. F. Barnes, Reversible Hydration of CH₃NH₃PbI₃

- in Films, Single Crystals, and Solar Cells, *Chem. Mater.* 2015, 27, 3397.
- [31] W. Huang, J. S. Manser, P. V. Kamat, S. Ptasinska, Evolution of Chemical Composition, Morphology, and Photovoltaic Efficiency of $\text{CH}_3\text{NH}_3\text{PbI}_3$ Perovskite under Ambient Conditions, *Chem. Mater.* 2015, 28, 303.
- [32] J. A. Christians, P. A. Miranda Herrera, P. V. Kamat, Transformation of the Excited State and Photovoltaic Efficiency of $\text{CH}_3\text{NH}_3\text{PbI}_3$ Perovskite upon Controlled Exposure to Humidified Air, *J. Am. Chem. Soc.* 2015, 137, 1530.
- [33] J. S. Yun, J. Kim, T. Young, R. J. Patterson, D. Kim, J. Seidel, S. Lim, M. A. Green, S. Huang, A. Ho-Baillie, Humidity-Induced Degradation via Grain Boundaries of $\text{HC}(\text{NH}_2)_2\text{PbI}_3$ Planar Perovskite Solar Cells, *Adv. Funct. Mater.* 2018, 28, 1705363
- [34] N. Ahn, K. Kwak, M. S. Jang, H. Yoon, B. Y. Lee, J. K. Lee, P. V. Pikhitsa, J. Byun, M. Choi, Trapped charge-driven degradation of perovskite solar cells, *Nat. Commun.* 2016, 7, 13422.
- [35] Q. Wang, Y. Shao, H. Xie, L. Lyu, X. Liu, Y. Gao, J. Huang, Qualifying composition dependent p and n self-doping in $\text{CH}_3\text{NH}_3\text{PbI}_3$, *Appl. Phys. Lett.* 2014, 105, 163508
- [36] D. Meggiolaro, S. G. Motti, E. Mosconi, A. J. Barker, J. Ball, C. Andrea Riccardo Perini, F. Deschler, A. Petrozza, F. De Angelis, Iodine chemistry determines the defect tolerance of lead-halide

perovskites, *Energy Environ. Sci.* 2018, 11, 702.

- [37] H. Jin, E. Debroye, M. Keshavarz, I. G. Scheblykin, M. B. J. Roeffaers, J. Hofkens, J. A. Steele, It's a trap! On the nature of localised states and charge trapping in lead halide perovskites, *Mater. Horiz.* 2020, 7, 397.

Chapter 2. Electron transport Layer-Dependent Band Bending in Perovskite Solar Cells and Its Correlation to Device Degradation

2.1 Introduction.

Photovoltaics have evolved from costly silicon solar cells to inorganic or organic thin-film solar cells that are sustainable energy-generation devices. Among various types of solar cells, perovskite solar cells (PSCs) have attracted worldwide attention in recent years because of their soaring performance. The power-conversion efficiency (PCE) of the PSC quickly and remarkably exceeded that of its direct predecessors (dye-sensitized solar cells and organic photovoltaics). [1] In a PSC, a perovskite layer sandwiched by n-type and p-type semiconducting layers has excellent properties in carrier generation and transfer, which can qualify the PSC as the next-generation photovoltaic devices [1,2].

Understanding the working principle of a PSC is essential to improvements in its photovoltaic performance. The researchers described the carrier dynamics in a PSCs based on semiconductor physics as they consider perovskite layer as an intrinsic layer. [3,4]. However, several studies reported

that perovskite layers behave as different types of semiconductor (p, i, or n) depending on their ionic composition [5-8], the types of adjacent charge-selective layers [9] and kinds of metal electrode [10]. These studies suggested the different semiconductor properties of perovskite layers can cause unexpected effects of photo-carrier dynamics.

Research on improving the stability of PSCs is treated as the utmost matter, producing many experimental results. [11-21] It has been suggested that O₂ and H₂O molecules are the extrinsic origins of device degradation. [11-14] Also, charges such as photo-carriers and ions have been identified as intrinsic sources of device degradation. [15-19] Although extrinsic origins can be protected to some extent by encapsulation techniques [20,21], It is impossible to completely block them for ensuring a long-term stability comparable to commercialized solar cells and the encapsulation itself could not prevent intrinsic degradation source such as the charge trapping behavior. As charge behaviors including charge accumulation have a close correlation with the working principle, it is imperative not only to understand the precise fundamentals of PSCs, but also identify a clear relationship between working mechanism and degradation of PSCs.

Herein, we revealed that solar cells using methylammonium lead iodide (MAPbI₃ or CH₃NH₃PbI₃) are always not represented an ideal p-i-n junction, but a p-n junction dominating at a specific interface depending on the kind of electron transport layers. Different location of dominant p-n junction (high degree of band bending) with respect to electron transporting

layers is deeply related with charge accumulation behavior in the PSCs that affects degradation process. Locations of band bending, polarity of charges and charge density distribution in the devices with different ETLs are analyzed by using electron-beam-induced current (EBIC) and Kelvin probe force microscopy (KPFM) measurements. In addition, we measured the amount and types of accumulated charges when different types of ETLs were employed. We analyzed degradation process of PSCs that aged under light illumination by using cross-sectional scanning electron microscope (SEM) images. The obtained results indicate that the dominant p-n junction appeared at the different interface depending on the kind of ETL and the charges mainly accumulate at the dominant p-n junction, leading to decomposition of perovskite materials. We verified, for the first time, the charges accumulated at the dominant p-n junction play a critical role in device degradation. From all these observation and analysis, we propose that ideal n-i-p junction PSC can be realized for long-term stability by designing to minimize band bending at the interfaces.

2.2 Experimental Methods

2.2.1 Device fabrication

Fluorine-doped tin oxide (FTO) glass substrates (AMG, Korea) were cleaned by sonicating in acetone, isopropanol, and deionized water. For TiO₂-based perovskite solar cells (PSCs), a planar TiO₂ layer was spin-coated on the FTO/glass substrate using 0.15 M solution with titanium di-isopropoxide (75 wt% in isopropanol, Sigma-Aldrich, USA) in 1-butanol solvent at 1,000 rpm for 10 s and then at 2,000 rpm for 40 s. After the spin-coating process, the TiO₂ film was annealed twice at 125 °C for 5 min and then calcinated at 500 °C for 1 h. The thickness of the TiO₂ layer was around 40 nm. TiO₂/C₆₀ based PSCs, a TiO₂ layer was fabricated on the FTO by using the same procedure, and a thin 20nm fullerene(C₆₀) layer was evaporated on the TiO₂ layer. For the PSCs with C₆₀ as the ETL, a C₆₀ layer (40 nm) was deposited on the FTO/glass substrate. In cross-sectional experimental results for the PSCs via the EBIC and KPFM measurements, a thick TiO₂ layer (~100 nm) was formed using 0.3 M titanium di-isopropoxide for the TiO₂-based devices, and C₆₀ layers with the thickness of 40 and 80 nm were deposited for the TiO₂/C₆₀-based and C₆₀-based devices, respectively.

A precursor solution of methylammonium lead iodide (MAPbI₃) was prepared by dissolving 461 mg of PbI₂ (Alfa Aesar, USA) and 159 mg of methylammonium iodide (MAI; Xian Polymer Light Technology, China)

using mixed adducts comprising 78 mg of dimethyl sulfoxide (DMSO; Sigma-Aldrich, USA) with 5mol% urea in 0.55 mL of N,N-dimethylformamide (DMF; Sigma-Aldrich, USA). The perovskite precursor solution was spin-coated on the ETL layer at 4,000 rpm for 20 s, and 0.5 mL of diethyl ether was dropped on the film. A transparent adduct film was annealed at 115 °C for 20 min. The Spiro-MeOTAD hole transporting layer was deposited by spin coating a precursor solution consisting of 72.3 mg of 2,2',7,7'-tetrakis(N,N'-di-p-methoxyphenylamine)-9,9'-spirobifluorene (spiro-MeOTAD; Merck KGaA, Germany) in 1 mL of chlorobenzene (Sigma-Aldrich, USA) at 2,000 rpm for 30 s. 28.8 µL of 4-tert-butyl pyridine and 17.5 µL of lithium bis(trifluoromethanesulfonyl)imide from a stock solution (520 mg of lithium bis(trifluoromethanesulfonyl)imide in 1 mL of acetonitrile, 99.8% purity, Sigma-Aldrich, USA) were added as a dopant to the mixture. A 50nm Au layer was deposited as an electrode on the HTL by using the thermal evaporator. All spin-coating processes were conducted in a dry room (<15% relative humidity, at room temperature).

2.2.2 Characterization

The J–V characteristics of PSCs were measured using a source meter (2400, Keithley, USA). AM 1.5G at 100 mW cm^{-2} one sun condition was realized using a solar simulator (Sol3A, Oriel, USA) with Si reference cell (Rc-1000-TC-KG5-N, VLSI Standards, USA) at room temperature inside a N₂ filled glove box. The active area of PSCs is 0.0729 cm^2 by using photo mask with same aperture area. All EBIC measurements were conducted with a field-emission scanning electron microscope (FE-SEM; Inspect F, FEI Corp., USA) with an EBIC system (DISS 5, Point Electronic GmbH, Germany). For cross-sectional EBIC imaging, an accelerating voltage of 2 kV and a working distance of 11–12 mm were used. A beam current in the range of 8–25 pA. The PSCs were mechanically cleaved for the cross-sectional EBIC analysis. The cleaved surface of each device was polished with a focused ion beam (FIB) treatment employing the system (Quanta 3D FEG, FEI Corp., USA) for the KPFM analysis [34-36]. The cross-sectional surface potential of the PSCs was examined with a KPFM system (Park NX10, Park Systems), using two types of Si tip coated with Cr–Au (NSC 36, Mikromasch, Germany), which had resonance frequencies of 90 kHz and spring constants of 1 N m^{-1} , at a scanning rate of 0.3 Hz and an AC tip voltage bias of 3V at 17 kHz. Tip-sample distance was less than 20nm. A white light-emitting diode (LED) with a luminous flux of 160 lm (DML 802, Makita, Japan) was used as the light source. The cross-sectional images of the PSCs were

obtained using a high-resolution SEM with a FIB system (AURIGA, Carl Zeiss, Germany, or Helios 650, FEI, USA). The KPFM measurements of the devices were performed with orthogonal tip orientation to two electrodes. To minimize error of measurement affected by apex of measuring tips, we scanned the same region several times. We carried out the charge extraction measurement with different delay times ranging from 0.3 ms to 180 s, and a cluster of white LEDs with a power density of 100 mW cm^{-2} was used as the light source. Electrochemical Impedance spectroscopy (EIS) measurements were performed at the frequency range of 0.1 Hz to 1.0 MHz under ambient conditions. White LEDs with a power density of 100 mW cm^{-2} was used as the light source. We applied the bias voltage ranging from 0.0 to 1.0 V in steps of 0.2 V during EIS measurement. The impedance spectra were fitted using Z View software (Scribner Associates, USA). The charge extraction and EIS analysis were conducted by using an electrochemical workstation (Autolab 320N, Metrohm, Switzerland) with an Autolab LED Driver Kit (Metrohm, Switzerland).

2.3 Result and discussion

2.3.1 Electron beam induced current measurement of devices with different charge selective layers

The band diagram which describe the electronic band structure of semiconductors in solar cells is a very useful visual tool to understand the working principles of the device. The generation, recombination, and flow of photo-carriers in a solar cell can be easily predicted using the band diagram. Band bending usually appears at a junction of two different semiconductor layers when they align their Fermi levels. To verify the working mechanism of the solar cell, it is required to understand a precise band diagram including band bending at all junctions. Cross-sectional EBIC measurements is widely used as the method to measure the junction structures in the photovoltaics, [10,22,23] and the detected current signals can give information on the depletion region, location of defects, and diffusion length of photo-carriers. [24-26]

In perovskite solar cells (PSCs), a titanium dioxide (TiO_2) and a fullerene (C_{60}) materials were widely used as ETLs and these two ETLs show different characteristics in terms of J-V hysteresis and operational stability [15, 27-29]. Although PSCs with TiO_2 as ETL showed quite high PCE, it was usually accompanied by large J-V hysteresis and unstable operation under light exposure, especially ultraviolet light. [15,27] On the other hands,

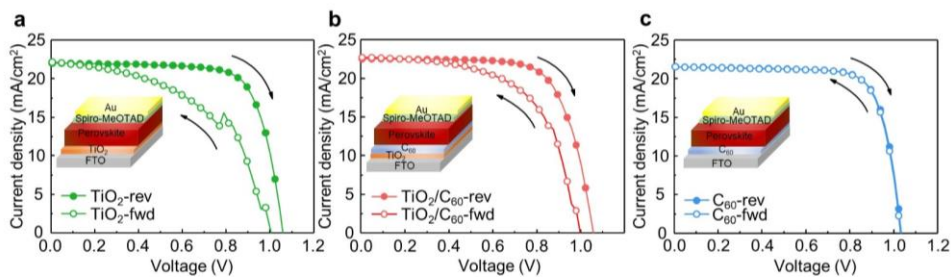
perovskite solar cells containing with C_{60} as ETLs showed less J-V hysteresis and better operational stability under light. [15,28,29]

To confirm a fundamental reason for such ETL-dependent device characteristics, we carried out cross-sectional EBIC measurements for PSCs fabricated with three different ETLs: a titanium dioxide (TiO_2) layer, a fullerene (C_{60}) layer, and a TiO_2/C_{60} bilayer. (see **Figure 2.1**) The other layers, such as the perovskite ($MAPbI_3$) layer and the hole-transporting layer (spiro-MeOTAD with doping), were the same for all three devices. The device structure was FTO/ETL/ $MAPbI_3$ /HTL/Au (where FTO means fluorine-doped tin oxide). During the measurements, an electron-beam (E-beam) was focused on the cross-sectional plane of the cleaved devices to generate electron-hole pairs. The generated charges transport to respective metal electrode and finally flowed through the external circuit. The quantity of extracted charges was measured as a total current at the same time, as illustrated in **Figure 2.2a**. The values of generated current by the E-beam and their corresponding locations can be visualized simultaneously by overlapping the cross-sectional SEM image and the measured beam induced current signals. **Figure 2.2b–d** show combined images with the EBIC results and their corresponding cross-sectional SEM images of devices with different ETLs. All EBIC measurements were performed at the unexposed regions by the electron beam to prevent devices from electron beam damage. [30-32] The bright green color inside a perovskite layer indicates higher intensity of EBIC signals. In the TiO_2 -based device, shown in **Figure 2.2b**, the highest EBIC signal was

observed mostly at the MAPbI₃/TiO₂ interface, while weak EBIC signal were obtained across the entire perovskite layer. The results of high EBIC signals at the interface between the perovskite layer and the TiO₂ layer shows good consistency with previous studies. [22,33] On the contrary, in the case of the C₆₀-based and TiO₂/C₆₀-based devices, high intensity of EBIC signal was mainly observed at interface with perovskite near the spiro-MeOTAD layer, as shown in **Figure 2.2c** and **2.2d**. Note that the current signals and the brightness of the green color present the relative value of current, not the absolute values of the current. As the EBIC signals can identify the location where dominant junction (high degree of band bending) appear [23], line profiles of EBIC signals perpendicular to the layers were obtained to analyze the junction structure in the device with the different ETL layers (see **Figure 2.2 e–g**).

In the TiO₂ ETL based device, unlike the weak EBIC signals at the MAPbI₃/spiro-MeOTAD interface, the EBIC signals were extremely focused at the TiO₂/MAPbI₃ interface (**Figure 2.2e**). This implies that a substantial amount of the generated electron-hole pairs adjacent to the TiO₂ interface were dissociated and transferred to the electron-transport layer (ETL). In other words, as compared to interface between MAPbI₃ and spiro-MeOTAD layers, there was dominant p-n junction (depletion region) at the interface between TiO₂ and MAPbI₃ layers due to appearance of strong built in electric field. On the other hands, for the TiO₂/C₆₀-based and C₆₀-based devices, EBIC signals with relatively high intensity obtained in the MAPbI₃ layer near the

spiro-MeOTAD interface. These results indicate that the dominant p-n junction (depletion region) appears at the perovskite/spiro-MeOTAD interface when the MAPbI₃ layer is inserted with C₆₀ as ETL and spiro-MeOTAD layers as HTL (**Figure 2.2f** and **2.2g**, respectively). We confirmed that the specific location of the dominant p-n junction changes depending on the usage of different kinds of ETL materials. The EBIC signals of the C₆₀-based device were uniformly distributed across entire MAPbI₃ layer compared to signals of the other devices (**Figure 2.2g**). These results imply that a thick depletion region with uniform electric field is formed in perovskite layers in C₆₀-based devices.



	V_{oc} (V)	J_{sc} (mA/cm ²)	FF(%)	Efficiency(%)
TiO ₂ -rev	1.06	22.02	73.84	17.20
TiO ₂ -fwd	1.00	22.08	55.54	12.31
TiO ₂ /C ₆₀ -rev	1.02	22.25	76.72	17.38
TiO ₂ /C ₆₀ -fwd	1.00	22.30	65.93	14.64
C ₆₀ -rev	1.04	20.52	76.57	17.08
C ₆₀ -fwd	1.03	21.52	76.58	17.04

Figure 2.1. J-V scan and parameters of the a) TiO₂-based device, b) TiO₂/C₆₀-based device, c) C₆₀-based device measured in reverse (full circle) and forward (hollow circle) scan, respectively.

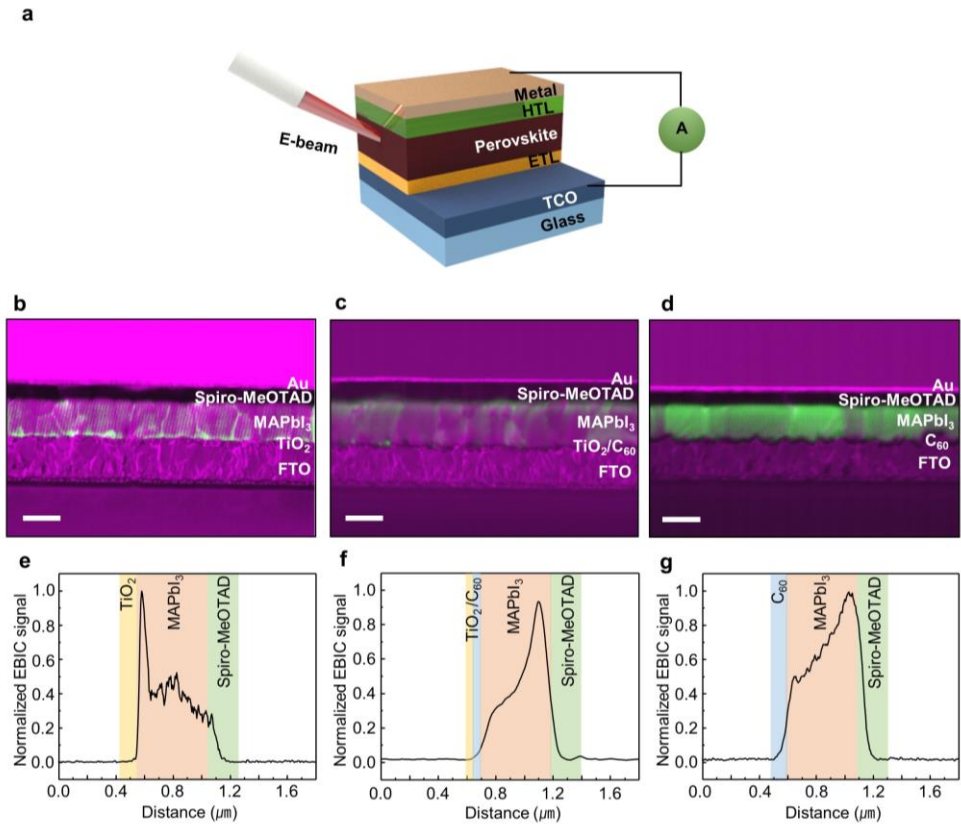


Figure 2.2 (a) Illustration of EBIC measurement on a cross-sectional surface of a cleaved perovskite solar cell. Cross-sectional EBIC image overlaid with corresponding SEM image of (b) TiO₂-based, (c) TiO₂/C₆₀-based, and (d) C₆₀-based devices. Bright green color on the images indicate the high EBIC signal. Profiles of measured EBIC signals perpendicular to layers of the (e) TiO₂-based, (f) TiO₂/C₆₀-based, and (g) C₆₀-based devices. Scale bars: 500 nm.

2.3.2. Kelvin probe forced microscopy measurement of devices

To understand the comprehensive solar-cell physics it is required to investigate the more detailed electrical properties across the device. The local contact potential differences (CPDs) of cross-sectional surface in the cleaved devices with different ETLs (TiO_2 and C_{60}) were measured by kelvin probe forced microscopy (KPFM), as depicted in **Figure 2.3a**. The cross-sectional surfaces in all devices were treated by focused ion beam (FIB) milling to remove signal errors by the artifacts. The KPFM measurements in the devices were performed using LED as a light source in both the open-circuit (OC) state and short-circuit (SC) state. **Figure 2.3b** and **2.3e** show obtained CPD profiles across the all layers of the devices at OC (red line) and SC (blue line) states for the TiO_2 -based and C_{60} -based devices, respectively. Both topographic (top) and CPD images at SC and OC states (middle and bottom) of the two devices are shown in **Figure 2.4**. Their topographic images(top) show low surface roughness implying less artifact in the cross-sectional plane. [34-36]

When two semiconducting materials with different Fermi levels is contact each other, the vacuum level (VL) is shifted aligning two different Fermi levels to make equilibrium in two semiconductor materials. VL shift formed coincides with an electrical built-in potential (V_{BI}) at the junction, which can be directly measured from CPD in the SC state in both dark and light illuminated conditions. [36,37] **Figure.2.3** shows the CPD profiles at the

SC state decreased from the ETL toward the HTL while, for the OC state, it gradually increased from the ETL toward the HTL as a result of separate quasi-Fermi levels caused by increase carrier concentration in both TiO₂ and C₆₀-based devices. For the TiO₂-based device (**Figure 2.3b**), the CPD measured under light illumination in the SC state (blue line) decreased mainly at the TiO₂/MAPbI₃ interface. The CPD profile in the OC state showed a steeply increased at the TiO₂/MAPbI₃ interface, while CPD in the spiro-MeOTAD interface showed a slight increase (**Figure 2.3b**), implying that the formation of a dominant p–n junction (large vacuum level shift) at the TiO₂ interface. On the contrary, the C₆₀-based device showed a larger CPD change (VL shift) at the spiro-MeOTAD side in both OC and SC states as compared to the C₆₀ interface (**Figure 2.3e**). These results indicate the dominant p–n junction at the spiro-MeOTAD interface in the C₆₀-based device. Especially the CPD distribution in the OC state exhibited a relatively uniform increase in the MAPbI₃ layer, which imply that the C₆₀-based device, rather than TiO₂-based device, could behave like ideal p–i–n solar cell with uniform electric field in entire perovskite. These results are consistent with in the results of EBIC measurements (**Figure 2.2**).

Additionally, as CPD at the FTO electrode in both OC and SC states is the same values, the discrepancies between CPD in the OC and SC states at the gold electrode correspond to an actual V_{oc} in the devices [34,36] and it was ~670mV and ~740 mV in the TiO₂-based and C₆₀-based devices, respectively. V_{oc} measured by KPFM under LED light exposure shows

similar V_{OC} measured from one-sun illumination, as shown in **Figure 2.1**. In both devices, The V_{OC} values from the KPFM measurements, however, were smaller than the values measured under one-sun irradiation possibly because of the artifacts by tip orientation, tip convolution effect[38,39], and different light intensities compared to intensity of one sun (**Figure 2.1**).

Vacuum level shift at the junction is accompanied with an electrical built-in potential (V_{BI}). To identify the location of dominant p-n junction, relative magnitude of the E-field across the device should be determined. We calculated the normalized E-field from the CPD distribution measured in the OC state under illumination conditions based on the following equation (**Figure 2.3c and 2.3f**) [34-36];

$$E(x) = -\frac{d}{dx}CPD(x) \quad (1)$$

For the TiO_2 -based device, a strong E-field appeared at the $MAPbI_3/TiO_2$ interface, while a weak E-field was uniformly distributed in the $MAPbI_3$ layer and at the $MAPbI_3/spiro-MeOTAD$ interface, as shown in **Figure 2.3c**. On the other hand, for the C_{60} -based device, there was a strong E-field at the $MAPbI_3/spiro-MeOTAD$ interface rather than at the $C_{60}/MAPbI_3$ interface, as shown in **Figure 2.3f**. Compared to the device with the TiO_2 as an ETL, which had a large difference between the E-field magnitude of the two interfaces, there was only a small difference between

the magnitude of E-field of both interfaces of the device with the C₆₀ as an ETL. It is worth noting that the E-field in the C₆₀ -based devices was formed throughout the CH₃NH₃PbI₃ layer without a distinctive peak field strength, which appeared in the device with the TiO₂ ETL. This implies that the CH₃NH₃PbI₃ layer relatively acted as an intrinsic semiconductor with uniform electric field the device with the C₆₀ ETL.

Using the following Poisson's equation, we also calculated the charge-density distribution inside the devices from the KPFM results [35,36]

$$\rho(x) = \varepsilon_0 \varepsilon_r \frac{d}{dx} E(x) = -\varepsilon_0 \varepsilon_r \frac{d^2}{dx^2} \Delta\text{CPD}(x) \quad (2)$$

where $\rho(x)$ is the charge density, $E(x)$ is the E-field, ΔCPD is the difference between CPD values measured at the SC and OC states, ε_0 and ε_r are the dielectric constants of vacuum and perovskite (MAPbI₃) layer, respectively. **Figure 2.3d** and **Figure 2.3g** shows the charge density profiles from the TiO₂-based and C₆₀-based devices, respectively. For the TiO₂-based device, holes remained at the TiO₂ interface, and the net charge in the MAPbI₃ perovskite layer was also positive due to this large hole accumulation (**Figure 2.3d**). The charge-density distribution profile of the TiO₂-based device exhibited a similar result to those of previous study. [36] However, the distribution profile of the C₆₀-based device depicted that electrons mainly accumulated at the spiro-MeOTAD interface rather than at the C₆₀ interface.

The net charge of the entire MAPbI₃ layer in the C₆₀-based device was negative and its absolute value was lower than that of the TiO₂-based device.

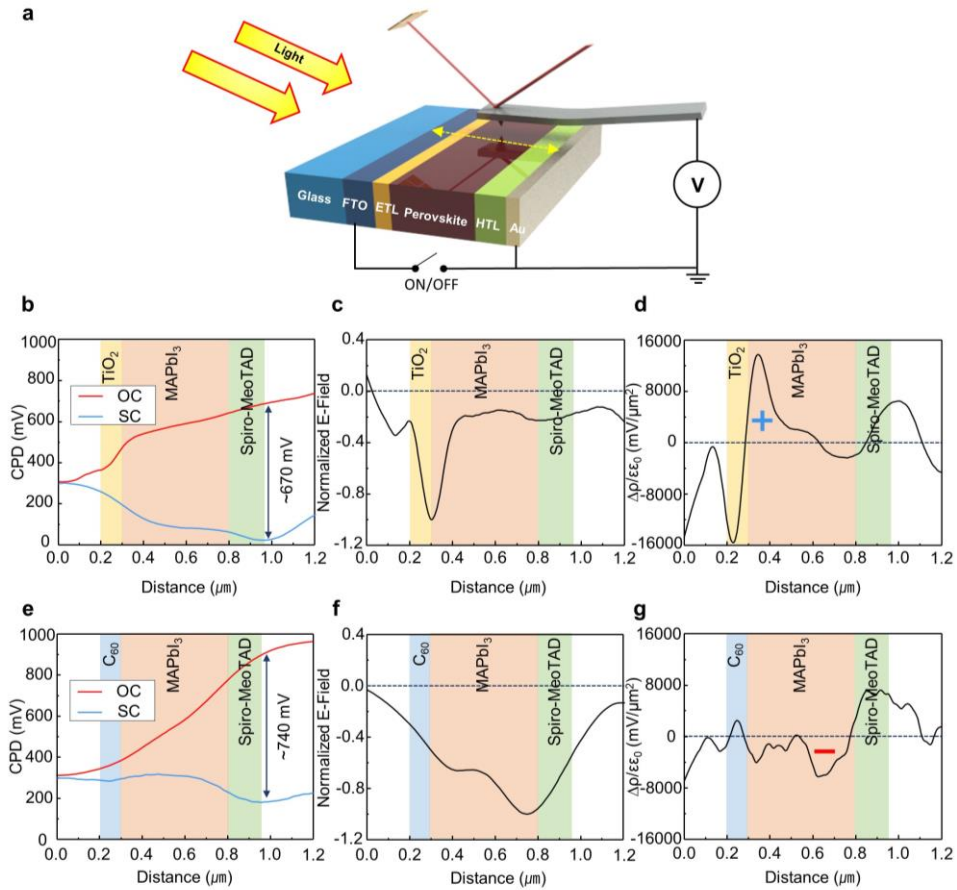


Figure 2.3 (a) Illustration of KPFM measurements of cross-sectional plane in devices under operating conditions with light illumination. CPD distribution under illumination at open-circuit (OC) condition (red line) and at short-circuit (SC) condition (blue line) of (b) TiO_2 -based and (e) C_{60} -based devices. The arrows in (b) and (e) indicate the open-circuit voltage, V_{OC} . Normalized E-field distribution under illumination at open-circuit condition of the (c) TiO_2 -based and (f) C_{60} -based devices. Charge density profile calculated from potential difference between the open-circuit and short-circuit voltages ($\text{CPD}_{\text{OC}} - \text{CPD}_{\text{SC}}$) of (d) TiO_2 -based and (g) C_{60} -based devices.

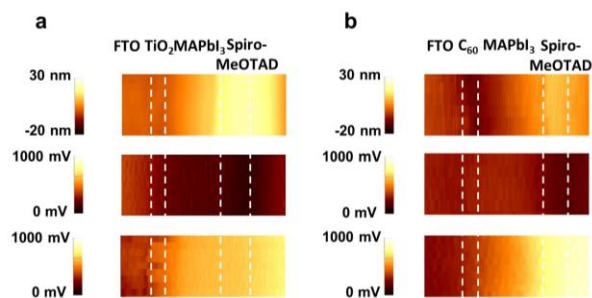


Figure 2.4 (a) The cross-sectional images of topography (Top), and the CPD distribution at short circuit state (middle) and at open circuit state (bottom) for the TiO₂-based device. (b) The cross-sectional images of topography (Top), and the CPD distribution at short circuit state (middle) and at open circuit state (bottom) for C₆₀-based device. KPFM measurement were conducted in all devices under LED light illumination

From the EBIC and KPFM experimental results, we explored the location of the dominant junction (large VL shift), E-field distribution, and charge density distribution in the device under illumination. We confirmed that the carrier dynamics in the devices depended on the adjacent electron-transporting layers with perovskite layer and there was dominant P-N junction at specific interface with respect to different ETLs.

Figure 2.5 showed electronic band diagrams of two different devices with TiO₂ and C₆₀- in both SC and OC states; the band bending to align the different Fermi levels of the two semiconducting materials were taken into consideration. Fermi level of ETL (C₆₀ and TiO₂) is close to the conduction band edge because N-type semiconductors is used as an ETL. For TiO₂ device, the higher energy level of the conduction band (~ Fermi level) in the TiO₂ ETL than that in the C₆₀ ETL leads to larger band bending between perovskite and ETLs in the TiO₂-based device [40,41] In the SC state, the built-in potential by band bending affect the separation and transport of photo-generated charge carriers. In the TiO₂-based device, the TiO₂/MAPbI₃ interface was the region where the dominant carrier transfer is drift (**Figure 2.5a**). On the contrary, in the C₆₀-based device, carrier drift occurred mainly at the MAPbI₃/spiro-MeOTAD interface (**Figure 2.5b**). In the OC state, while hole accumulation at the ETL/MAPbI₃ interface in the TiO₂-based device (**Figure 2.5c**), electrons accumulation at the MAPbI₃/HTL interface in the C₆₀-based device (**Figure 2.5d**). Especially, many holes accumulated at the TiO₂/MAPbI₃ interface, while a small number of electrons were left at the

MAPbI₃/HTL interface in the TiO₂-based device. In contrast, in the C₆₀-based device, more electrons piled up at the MAPbI₃/HTL interface than the number of holes accumulating at the C₆₀/MAPbI₃ interface.

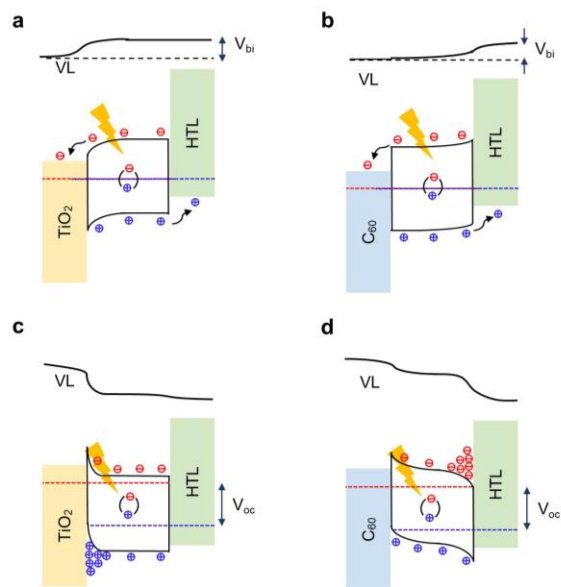


Figure 2.5 Illustration of electronic band diagrams for (a) TiO₂-based devices and (b) C₆₀-based devices under light illumination in short-circuit (SC) state. Illustration of electronic band diagrams of the (c) TiO₂-based devices and (d) C₆₀-based devices under light illumination in open circuit (OC) state. Here, the red dotted line and blue dotted line indicate the quasi-Fermi level of electrons and quasi-Fermi level of holes, respectively. VL, HTL, V_{BI} , and V_{OC} indicate vacuum level, hole-transporting layer, built-in potential, open-circuit voltage, respectively.

2.3.3. Device degradation characteristics of devices underlying different charge accumulation

To estimate the absolute quantity of accumulated charges in the working device during transition from the OC state under light illumination to SC state in dark, we directly measured the amount of accumulated charges in the three different devices by employing charge-extraction method. [42-44] The accumulated charges in a device in the OC state under illumination were extracted after a certain delay period, switching to the SC state and dark conditions. **Figure 2.6 a** and **b** shows illustration of process of extraction charge measurement. The quantity of the extracted charges depending on delay time for the three different devices is shown in **Figure 2.6c**. The TiO₂-based device possessed the largest amount of extracted charges regardless of the delay time compared to other devices, which is good agreement with the KPFM results in **Figure 2.3d** and **2.3g**. It is known that charge accumulation is closely related to the capacitance of surface charge accumulation (C_s). [45, 46] Thus, we additionally investigated the surface charge capacitance using Electrochemical impedance spectroscopy (EIS) (**Figure 2.7**). [47] The capacitance of surface charge accumulation in the TiO₂-based device exhibited the highest value compared to the C₆₀-based and TiO₂/C₆₀-based devices, which is also consistent with the results of charge extraction measurement.

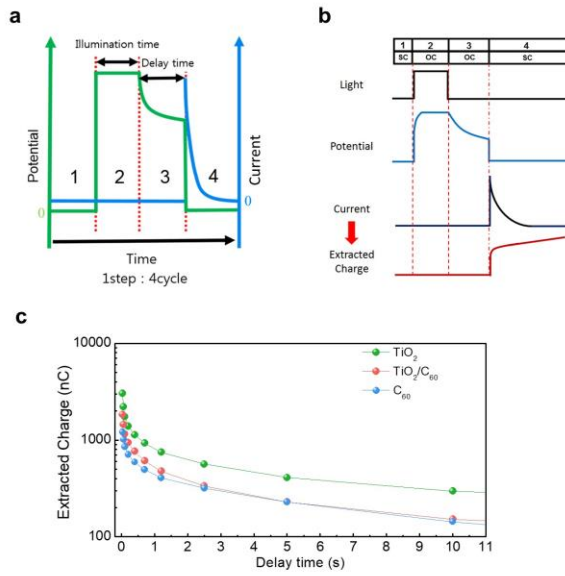


Figure 2.6. (a) Illustration of process of charge extraction measurements. (b) Sequence showing the relation in each process between illumination, measured potential and calculated charge in the charge extraction measurement (c) The quantity of extracted charges as a function of delay time up to 10s for the three different devices.

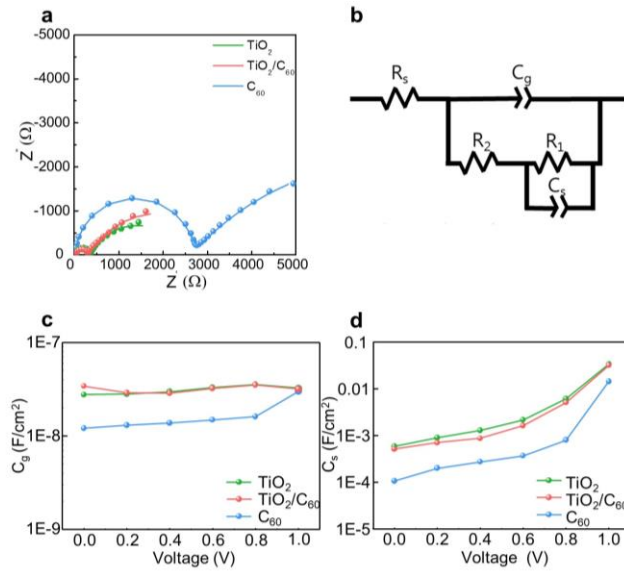


Figure 2.7. (a) The nyquist plot of perovskite solar cells depending on the kinds of ETLs. (b) an equivalent circuit we apply. (c) geometrical capacitance and (d) capacitance of surface charge accumulation with different voltage bias. EIS measurements are conducted under LED light and ambient air condition. Here, R_s indicates ohmic resistance including contacts and wires, C_g and C_s is the capacitance of dielectric properties of the perovskite layer and the capacitance of surface charge accumulation at the interfaces, respectively. R_1, R_2 are associated with the resistance of recombination current flux.

We measured the time dependent operational stability for three un-encapsulated devices under one sun illumination and ambient conditions (**Figure 2.8a**). The devices were measured in the OC state and thus had accumulated charges during the measurements as shown in **Figure 2.3** and **Figure.2.8a**. The results exhibit a close correlation between the quantity, polarity of accumulated charges and light-induced stability in air. As can be seen in **Figure 2.7c** and **Figure 2.8a**, the PCE decrease is the smallest for C₆₀-based device that had less accumulated charges while PCE drop is the largest for TiO₂-based device that possessed the large amount of charges in charge extraction measurement. Additionally, we investigated the effect of the accumulated charges on the device stability by tracking the degradation patterns of cross-sectional surface in the devices using FIB-SEM measurements. **Figure 2.8b**, **2.8c**, and **2.8d** show the time evolution of light induced degradation process of the TiO₂-based, TiO₂/C₆₀-based, and C₆₀-based devices under ambient air, respectively. These SEM images shows clear differences in the region where degradation is initiated in the perovskite layer among the three devices. In the TiO₂-based device, the perovskite layer starts to be decomposed mostly near the TiO₂/ perovskite interface (**Figure 2.8b**). On the contrary, the perovskite layer in the TiO₂/C₆₀-based and C₆₀-based devices starts to be degraded near the interface with the spiro-MeOTAD layer (**Figure 2.8c** and **2.8d**). Interestingly, the region at which deterioration began were the same with the location of the dominant p-n junctions where charges were mainly accumulated (**Figures 2.2** and **2.3**). These results clearly

revealed that the localization of excess charges in the perovskite layer at specific interface were deeply correlated with perovskite degradation, which weakened E-field at the interface. Depending on different ETLs, the dominant p-n junction formed at the specific interface which has higher degree of band bending than the other interface. Most of charges are localized at the corresponding junction where the degradation was initiated. Previous studies reported that selective contact layers with different capacitive and transport properties causes imbalanced charge accumulation in the perovskite material. Such excess charges affect ion instability and result in promoting irreversible chemical reactions of perovskite. [15-17,19,48-52]

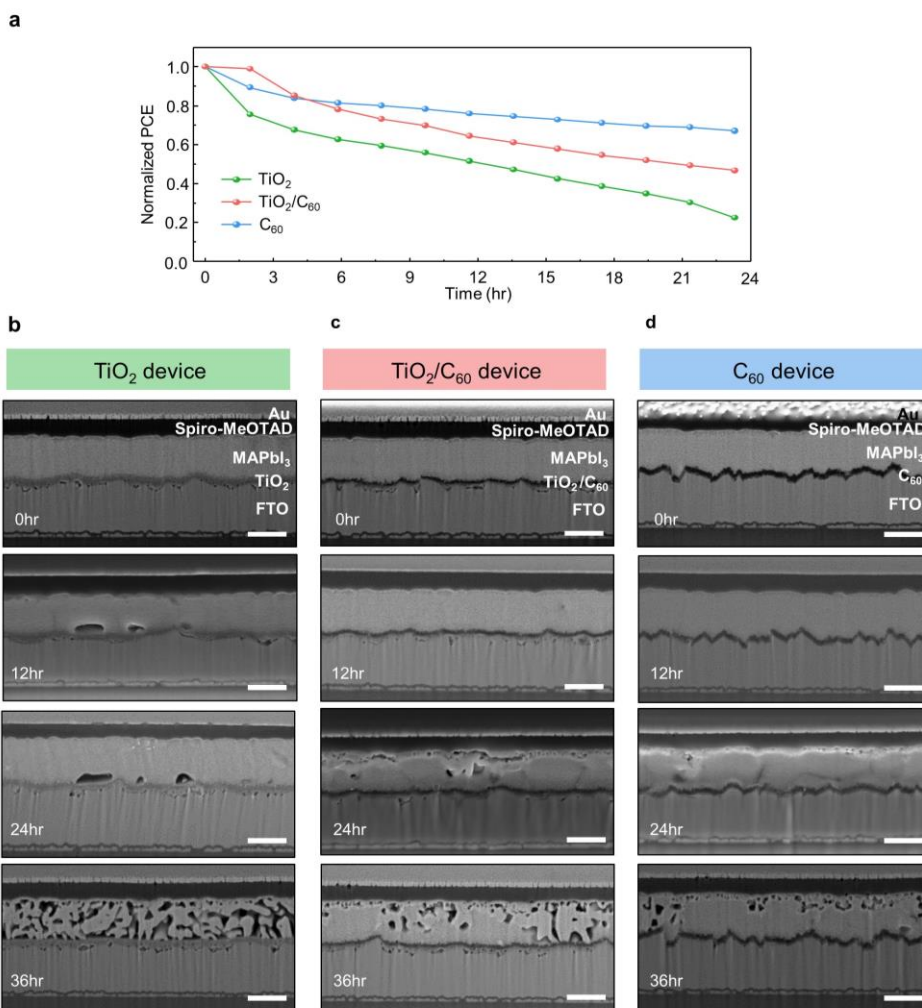


Figure 2.8 (a) Time dependent operational stability of un-encapsulated devices with respect to different ETLs under one sun illumination in ambient air. Time evolution of cross-sectional SEM images for degradation process in (b) TiO₂-based, (c) TiO₂/C₆₀-based, and (d) C₆₀-based devices. Scale bars: 500 nm

2.3.4. Design of ideal n-i-p solar cells

Finally, we suggest a model of an ideal solar cells in terms of both high performance and stability (see **Figure 2.9**). The energy band diagram of an ideal p-i-n PSC is similar with that of an a-Si:H/ μ c-Si:H solar cell with n-i-p structure (a-Si:H stands for hydrogenated amorphous silicon; μ c-Si:H stands for hydrogenated microcrystalline silicon). [53, 54] The ideal p-i-n perovskite solar cell is expected to exhibit high performance and stability because there is a uniform electric field across the entire perovskite at operation condition. When the whole perovskite layer acts as an intrinsic layer (depletion region), we can not only expect that uniform electric field make the efficient carrier separation and extraction, but also that the degradation rate slows down due to the absence of region where ions and carriers were highly concentrated. To fabricate PSC with ideal n-i-p structure, it is imperative to employ perovskite materials with low defect density and proper charge transport layer having high conductivity and high compatibility in energy band. As defects are known to be the origin of ion migration and charge trapping, native defects in perovskite films apparently have a negative influence on device degradation. [55-59] An ideal approach to fabricated n-i-p perovskite solar cells is to employ perovskite films close to single crystalline film or mixed perovskite composition with triple or quadruple cation because they have low defect level, long carrier diffusion length and stabilized perovskite phase. [60-64] At the same time, charge selective layers

(ETLs and HTLs) should not only have favorable energy level alignment with perovskite layer for charge extraction but also good ability of charge transporting charge to prevent charge accumulation. When the PSCs operate as ideal p-i-n solar cell using several approaches, we can expect both efficient carrier extraction and less degradation owing to the absence of regions with high density of accumulated charges. The perovskite layer with high crystalline phase and selection of proper charge selective contacts is essential to achieve the long-term stability.

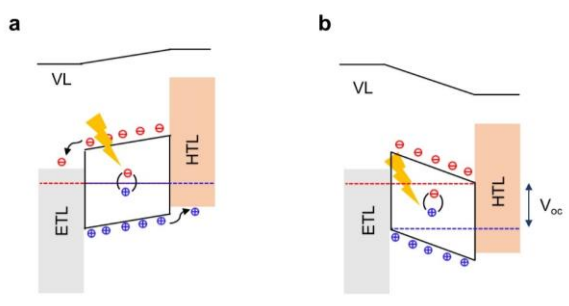


Figure 2.9 Schematic illustrations of electronic band diagrams in solar cells with ideal N-I-P junction type under light illumination at a) short-circuit (SC) state and b) open-circuit (OC) state.

2.4 conclusion

This study revealed the degradation mechanism by charge accumulation where electronic band bending occurred and device degradation in device with different ETLs using TiO_2 , $\text{TiO}_2/\text{C}_{60}$, C_{60} layer. The results of the EBIC measurements showed that the location of the dominant p–n junction depends on the charge selective contacts. The vacuum level profiles, E-field and charge- density distribution in the devices were analyzed using the cross-sectional KPFM data. We found that charges mainly accumulated at the specific location of dominant p–n junction in the device with different ETLs and obtained the quantity of the accumulated charges using the charge extraction measurement. Throughout the photo-aging process under a one-sun illumination, device degradation is initiated at the position where charge mainly accumulated, resulting in different light induced degradation patterns in the device. These results provide clear evidence that there was a strong correlation between the ETLs dependent working mechanism of PSCs and degradation of devices. Our study proposed design principle for ensuring both high performance and stability through fabrication of ideal p-i-n type PSC that minimize band bending at the interfaces by employing high crystalline perovskite materials and seeking proper selective contacts.

2.5 references.

- [1] Q. Jiang, Y. Zhao, X. Zhang, X. Yang, Y. Chen, Z. Chu, Q. Ye, X. Li, Z. Yin and J. You, Surface passivation of perovskite film for efficient solar cells *Nature Photonics*, 2019, 13, 460-466
- [2] E. H. Jung, N. J. Jeon, E. Y. Park, C. S. Moon, T. J. Shin, T.-Y. Yang, J. H. Noh and J. Seo, Efficient, stable and scalable perovskite solar cells using poly(3-hexylthiophene), *Nature*, 2019, 567, 511-515.
- [3] M. M. Lee, J. Teuscher, T. Miyasaka, T. N. Murakami and H. J. Snaith, Efficient Hybrid Solar Cells Based on Meso-Superstructured Organometal Halide Perovskites, *Science*, 2012, 338, 643.
- [4] W.-J. Yin, T. Shi and Y. Yan, Unique Properties of Halide Perovskites as Possible Origins of the Superior Solar Cell Performance, *Adv. Mater.*, 2014, 26, 4653-4658.
- [5] P. Cui, D. Wei, J. Ji, H. Huang, E. Jia, S. Dou, T. Wang, W. Wang and M. Li, Planar p–n homojunction perovskite solar cells with efficiency exceeding 21.3%, *Nature Energy*, 2019, 4, 150-159.
- [6] B. Dänekamp, C. Müller, M. Sendner, P. P. Boix, M. Sessolo, R. Lovrincic and H. J. Bolink, J., Perovskite–Perovskite Homojunctions via Compositional Doping, *Phys. Chem. Lett.*, 2018, 9, 2770-2775.
- [7]. Q. Wang, Y. Shao, H. Xie, L. Lyu, X. Liu, Y. Gao and J. Huang, Qualifying composition dependent p and n self-doping in $\text{CH}_3\text{NH}_3\text{PbI}_3$, *Appl. Phys. Lett.*, 2014, 105, 163508.

- [8]. Q. Ou, Y. Zhang, Z. Wang, J. A. Yuwono, R. Wang, Z. Dai, W. Li, C. Zheng, Z.-Q. Xu, X. Qi, S. Duhm, N. V. Medhekar, H. Zhang and Q. Bao, Strong Depletion in Hybrid Perovskite p–n Junctions Induced by Local Electronic Doping. *Adv. Mater.*, 2018, 30, 1705792.
- [9] S. Olthof and K. Meerholz, Substrate-dependent electronic structure and film formation of MAPbI₃ perovskites, *Scientific Reports*, 2017, 7, 40267.
- [10] N. Kedem, M. Kulbak, T. M. Brenner, G. Hodes and D. Cahen, Type-inversion as a working mechanism of high voltage MAPbBr₃(Cl)_{3-x} based halide perovskite solar cells, *Phys. Chem. Chem. Phys.*, 2017, 19, 5753-5762
- [11] A. J. Pearson, G. E. Eperon, P. E. Hopkinson, S. N. Habisreutinger, J. T.-W. Wang, H. J. Snaith and N. C. Greenham, Oxygen Degradation in Mesoporous Al₂O₃/CH₃NH₃PbI_{3-x}Cl_x Perovskite Solar Cells: Kinetics and Mechanisms, *Adv. Energy Mater.*, 2016, 6, 1600014
- [12] N. Aristidou, C. Eames, I. Sanchez-Molina, X. Bu, J. Kosco, M. S. Islam and S. A. Haque, A., Fast oxygen diffusion and iodide defects mediate oxygen-induced degradation of perovskite solar cells, *Nat. Commun.*, 2017, 8, 15218.
- [13]. J. S. Yun, J. Kim, T. Young, R. J. Patterson, D. Kim, J. Seidel, S. Lim, M. A. Green, S. Huang and A. Ho-Baillie, Humidity-Induced Degradation via Grain Boundaries of HC(NH₂)₂PbI₃ Planar Perovskite Solar Cells, *Adv. Funct. Mater.*, 2018, 28, 1705363.

- [14] D. Bryant, N. Aristidou, S. Pont, I. Sanchez-Molina, T. Chotchunangatchaval, S. Wheeler, J. R. Durrant and S. A. Haque, Light and oxygen induced degradation limits the operational stability of methylammonium lead triiodide perovskite solar cells, *Energy Environ. Sci.*, 2016, 9, 1655-1660.
- [15] N. Ahn, K. Kwak, M. S. Jang, H. Yoon, B. Y. Lee, J.-K. Lee, P. V. Pikhitsa, J. Byun and M. Choi, Trapped charge-driven degradation of perovskite solar cells, *Nat. Commun.*, 2016, 7, 13422.
- [16] M.-c. Kim, N. Ahn, E. Lim, Y. U. Jin, Peter V. Pikhitsa, J. Heo, S. K. Kim, H. S. Jung and M. Choi, Degradation of $\text{CH}_3\text{NH}_3\text{PbI}_3$ perovskite materials by localized charges and its polarity dependency, *J. Mater. Chem. A.*, 2019, 7, 12075-12085.
- [17] K. Kwak, E. Lim, N. Ahn, J. Heo, K. Bang, S. K. Kim and M. Choi, An atomistic mechanism for the degradation of perovskite solar cells by trapped charge, *Nanoscale*, 2019, 11, 11369-11378.
- [18] T. Zhang, X. Meng, Y. Bai, S. Xiao, C. Hu, Y. Yang, H. Chen and S. Yang, Profiling the organic cation-dependent degradation of organolead halide perovskite solar cells, *J. Mater. Chem. A.*, 2017, 5, 1103-1111.
- [19] Y. Lin, B. Chen, Y. Fang, J. Zhao, C. Bao, Z. Yu, Y. Deng, P. N. Rudd, Y. Yan, Y. Yuan and J. Huang, Excess charge-carrier induced instability of hybrid perovskites, *Nat. Commun.*, 2018, 9, 4981.
- [20] Y. Han, S. Meyer, Y. Dkhissi, K. Weber, J. M. Pringle, U. Bach, L.

- Spiccia and Y.-B. Cheng, Degradation observations of encapsulated planar $\text{CH}_3\text{NH}_3\text{PbI}_3$ perovskite solar cells at high temperatures and humidity, *J. Mater. Chem. A.*, 2015, 3, 8139-8147.
- [21] F. Matteocci, L. Cinà, E. Lamanna, S. Cacovich, G. Divitini, P. A. Midgley, C. Ducati and A. Di Carlo, Encapsulation for long-term stability enhancement of perovskite solar cells, *Nano Energy*, 2016, 30, 162-172.
- [22] E. Edri, S. Kirmayer, A. Henning, S. Mukhopadhyay, K. Gartsman, Y. Rosenwaks, G. Hodes and D. Cahen, Why Lead Methylammonium Tri-Iodide Perovskite-Based Solar Cells Require a Mesoporous Electron Transporting Scaffold (but Not Necessarily a Hole Conductor), *Nano Letters*, 2014, 14, 1000-1004.
- [23] N. Kedem, T. M. Brenner, M. Kulbak, N. Schaefer, S. Levchenko, I. Levine, D. Abou-Ras, G. Hodes and D. Cahen, Light-Induced Increase of Electron Diffusion Length in a p-n Junction Type $\text{CH}_3\text{NH}_3\text{PbBr}_3$ Perovskite Solar Cell, *J. Phys. Chem. Lett.*, 2015, 6, 2469-2476.
- [24] W. S. Lau, D. S. H. Chan, J. C. H. Phang, K. W. Chow, K. S. Pey, Y. P. Lim, V. Sane and B. Cronquist, Quantitative imaging of local defects in very thin silicon dioxide films at low bias voltage by true oxide electron-beam-induced current, *J. Appl. Phys.*, 1995, 77, 739-746.
- [25] O. Breitenstein, J. Bauer, M. Kittler, T. Arguirov and W. Seifert,

- EBIC and luminescence studies of defects in solar cells, *Scanning*, 2008, 30, 331-338.
- [26] M. Kulbak, I. Levine, E. Barak-Kulbak, S. Gupta, A. Zohar, I. Balberg, G. Hodes and D. Cahen, Control over Self-Doping in High Band Gap Perovskite Films, *Adv. Energy Mater.*, 2018, 8, 1800398.
- [27] T. Leijtens, G. E. Eperon, S. Pathak, A. Abate, M. M. Lee and H. J. Snaith, Overcoming ultraviolet light instability of sensitized TiO₂ with meso-superstructured organometal tri-halide perovskite solar cells, *Nat. Commun.*, 2013, 4, 2885.
- [28] W. Ke, D. Zhao, C. R. Grice, A. J. Cimaroli, J. Ge, H. Tao, H. Lei, G. Fang and Y. Yan, Efficient planar perovskite solar cells using room-temperature vacuum-processed C₆₀ electron selective layers, *J. Mater. Chem. A.*, 2015, 3, 17971-17976.
- [29] H. Yoon, S. M. Kang, J.-K. Lee and M. Choi, Hysteresis-free low-temperature-processed planar perovskite solar cells with 19.1% efficiency, *Energy Environ. Sci.*, 2016, 9, 2262-2266.
- [30] N. Klein-Kedem, D. Cahen and G. Hodes, Effects of Light and Electron Beam Irradiation on Halide Perovskites and Their Solar Cells, *Acc Chem. Res.*, 2016, 49, 347-354.
- [31] C. Xiao, Z. Li, H. Guthrey, J. Moseley, Y. Yang, S. Wozny, H. Moutinho, B. To, J. J. Berry, B. Gorman, Y. Yan, K. Zhu and M. Al-Jassim, Mechanisms of Electron-Beam-Induced Damage in Perovskite Thin Films Revealed by Cathodoluminescence

- Spectroscopy, *J. Phys. Chem. C.*, 2015, 119, 26904-26911.
- [32] B. W. Park, N. Kedem, M. Kulbak, D. Y. Lee, W. S. Yang, N. J. Jeon, J. Seo, G. Kim, K. J. Kim, T. J. Shin, G. Hodes, D. Cahen and S. I. Seok, Understanding how excess lead iodide precursor improves halide perovskite solar cell performance, *Nat. Commun.*, 2018, 9, 3301.
- [33] O. Hentz, P. Rekemeyer and S. Gradečak, Effects of Voltage Biasing on Current Extraction in Perovskite Solar Cells., *Adv. Energy Mater.*, 2018, 8, 1701378.
- [34] V. W. Bergmann, S. A. L. Weber, F. Javier Ramos, M. K. Nazeeruddin, M. Grätzel, D. Li, A. L. Domanski, I. Lieberwirth, S. Ahmad and R. Berger, Real-space observation of unbalanced charge distribution inside a perovskite-sensitized solar cell, *Nat. Commun.*, 2014, 5, 5001.
- [35] S. A. L. Weber, I. M. Hermes, S.-H. Turren-Cruz, C. Gort, V. W. Bergmann, L. Gilson, A. Hagfeldt, M. Graetzel, W. Tress and R. Berger, How the formation of interfacial charge causes hysteresis in perovskite solar cells, *Energy Environ. Sci.*, 2018, 11, 2404-2413.
- [36] V. W. Bergmann, Y. Guo, H. Tanaka, I. M. Hermes, D. Li, A. Klasen, S. A. Bretschneider, E. Nakamura, R. Berger and S. A. L. Weber, Local Time-Dependent Charging in a Perovskite Solar Cell, *ACS Appl. Mater. Interfaces*, 2016, 8, 19402-19409.
- [37] Q. Chen, L. Mao, Y. Li, T. Kong, N. Wu, C. Ma, S. Bai, Y. Jin, D. Wu,

- W. Lu, B. Wang and L. Chen, Quantitative operando visualization of the energy band depth profile in solar cells, *Nat. Commun.*, 2015, 6, 7745.
- [38] Chen, Q.; Ye, F.; Lai, J.; Dai, P.; Lu, S.; Ma, C.; Zhao, Y.; Xie, Y.; Chen, L., Energy band alignment in operando inverted structure P3HT:PCBM organic solar cells. *Nano Energy* 2017, 40, 454-461.
- [39] Charrier, D. S.; Kemerink, M.; Smalbrugge, B. E.; de Vries, T.; Janssen, R. A., Real versus measured surface potentials in scanning Kelvin probe microscopy. *ACS Nano* 2008, 2 (4), 622-6.
- [40] Sista, S.; Yao, Y.; Yang, Y.; Tang, M. L.; Bao, Z., Enhancement in open circuit voltage through a cascade-type energy band structure. *Appl. Phys. Lett.* 2007, 91 (22), 223508.
- [41] Y. Li, Y. Zhao, Q. Chen, Y. M. Yang, Y. Liu, Z. Hong, Z. Liu, Y. T. Hsieh, L. Meng, Y. Li and Y. Yang, Multifunctional Fullerene Derivative for Interface Engineering in Perovskite Solar Cells, *J. Am. Chem. Soc.*, 2015, 137, 15540-15547.
- [42] J. Bisquert, F. Fabregat-Santiago, I. Mora-Seró, G. Garcia-Belmonte and S. Giménez, Electron Lifetime in Dye-Sensitized Solar Cells: Theory and Interpretation of Measurements, *J. Phys. Chem. C.*, 2009, 113, 17278-17290.
- [43] R. K. Misra, S. Aharon, M. Layani, S. Magdassi and L. Etgar, A mesoporous-planar hybrid architecture of methylammonium lead iodide perovskite based solar cells, *J. Mater. Chem. A.*, 2016, 4,

14423-14429.

- [44] F. Giordano, A. Abate, J. P. Correa Baena, M. Saliba, T. Matsui, S. H. Im, S. M. Zakeeruddin, M. K. Nazeeruddin, A. Hagfeldt and M. Graetzel, Enhanced electronic properties in mesoporous TiO₂ via lithium doping for high-efficiency perovskite solar cells, *Nat. Commun.*, 2016, 7, 10379.
- [45] H.-S. Kim, I.-H. Jang, N. Ahn, M. Choi, A. Guerrero, J. Bisquert and N.-G. Park, Control of I–V Hysteresis in CH₃NH₃PbI₃ Perovskite Solar Cell, *J. Phys. Chem. Lett.*, 2015, 6, 4633-4639.
- [46] I. Zarazua, J. Bisquert and G. Garcia-Belmonte, Light-Induced Space-Charge Accumulation Zone as Photovoltaic Mechanism in Perovskite Solar Cells, *J. Phys. Chem. Lett.*, 2016, 7, 525-528.
- [47] I. Zarazua, G. Han, P. P. Boix, S. Mhaisalkar, F. Fabregat-Santiago, I. Mora-Sero, J. Bisquert and G. Garcia-Belmonte, Surface Recombination and Collection Efficiency in Perovskite Solar Cells from Impedance Analysis, *J. Phys. Chem. Lett.*, 2016, 7, 5105-5113.
- [48] E. Bi, H. Chen, F. Xie, Y. Wu, W. Chen, Y. Su, A. Islam, M. Grätzel, X. Yang and L. Han, Diffusion engineering of ions and charge carriers for stable efficient perovskite solar cells, *Nat. Commun.*, 2017, 8, 15330.
- [49] H.-S. Kim, I. Mora-Sero, V. Gonzalez-Pedro, F. Fabregat-Santiago, E. J. Juarez-Perez, N.-G. Park and J. Bisquert, Mechanism of carrier accumulation in perovskite thin-absorber solar cells, *Nat. Commun.*,

2013, 4, 2242

- [50] W. Nie, J.-C. Blancon, A. J. Neukirch, K. Appavoo, H. Tsai, M. Chhowalla, M. A. Alam, M. Y. Sfeir, C. Katan, J. Even, S. Tretiak, J. J. Crochet, G. Gupta and A. D. Mohite, Light-activated photocurrent degradation and self-healing in perovskite solar cells, *Nat. Commun.*, 2016, 7, 11574.
- [51] L. Zhang and P. H. L. Sit, Ab initio study of the role of iodine in the degradation of $\text{CH}_3\text{NH}_3\text{PbI}_3$, *J. Mater. Chem. A.*, 2017, 5, 9042-9049.
- [52] S. G. Motti, D. Meggiolaro, A. J. Barker, E. Mosconi, C. A. R. Perini, J. M. Ball, M. Gandini, M. Kim, F. De Angelis and A. Petrozza, Controlling competing photochemical reactions stabilizes perovskite solar cells, *Nature Photonics*, 2019, 13, 532-539.
- [53] G. Ahmad, S. Mandal, A. K. Barua, T. K. Bhattacharya and J. N. Roy, Band Offset Reduction at Defect-Rich p/i Interface Through a Wide Bandgap a-SiO:H Buffer Layer, *IEEE Journal of Photovoltaics*, 2017, 7, 414-420.
- [54] T. Söderström, F. J. Haug, V. Terrazzoni-Daudrix and C. Ballif, Optimization of amorphous silicon thin film solar cells for flexible photovoltaics, *J. Appl. Phys.*, 2008, 103, 114509.
- [55] T. Leijtens, G. E. Eperon, A. J. Barker, G. Grancini, W. Zhang, J. M. Ball, A. R. S. Kandada, H. J. Snaith and A. Petrozza, Carrier trapping and recombination: the role of defect physics in enhancing the open circuit voltage of metal halide perovskite solar cells, *Energy Environ.*

- Sci.*, 2016, 9, 3472-3481.
- [56] J. M. Azpiroz, E. Mosconi, J. Bisquert and F. De Angelis, Defect migration in methylammonium lead iodide and its role in perovskite solar cell operation, *Energy Environ. Sci.*, 2015, 8, 2118-2127.
- [57] D. Yang, W. Ming, H. Shi, L. Zhang and M.-H. Du, Fast Diffusion of Native Defects and Impurities in Perovskite Solar Cell Material $\text{CH}_3\text{NH}_3\text{PbI}_3$, *Chem. Mater.*, 2016, 28, 4349-4357.
- [58] A. Walsh and S. D. Stranks, Taking Control of Ion Transport in Halide Perovskite Solar Cells, *ACS Energy Lett.*, 2018, 3, 1983-1990.
- [59] T. S. Sherkar, C. Momblona, L. Gil-Escrig, J. Avila, M. Sessolo, H. J. Bolink and L. J. A. Koster, Recombination in Perovskite Solar Cells: Significance of Grain Boundaries, Interface Traps, and Defect Ions, *ACS Energy Lett.*, 2017, 2, 1214-1222.
- [60] D. Shi, V. Adinolfi, R. Comin, M. Yuan, E. Alarousu, A. Buin, Y. Chen, S. Hoogland, A. Rothenberger, K. Katsiev, Y. Losovyj, X. Zhang, P. A. Dowben, O. F. Mohammed, E. H. Sargent and O. M. Bakr, Low trap-state density and long carrier diffusion in organolead trihalide perovskite single crystals, *Science*, 2015, 347, 519.
- [61] Q. Han, S. H. Bae, P. Sun, Y. T. Hsieh, Y. M. Yang, Y. S. Rim, H. Zhao, Q. Chen, W. Shi, G. Li and Y. Yang, Single Crystal Formamidinium Lead Iodide (FAPbI₃): Insight into the Structural, Optical, and Electrical Properties, *Adv. Mater.*, 2016, 28, 2253-2258.
- [62] H. Tan, F. Che, M. Wei, Y. Zhao, M. I. Saidaminov, P. Todorovic, D.

- Broberg, G. Walters, F. Tan, T. Zhuang, B. Sun, Z. Liang, H. Yuan, E. Fron, J. Kim, Z. Yang, O. Voznyy, M. Asta and E. H. Sargent, Dipolar cations confer defect tolerance in wide-bandgap metal halide perovskites., *Nat. Commun.*, 2018, 9, 3100.
- [63] D. Y. Son, S. G. Kim, J. Y. Seo, S. H. Lee, H. Shin, D. Lee and N. G. Park, Universal Approach toward Hysteresis-Free Perovskite Solar Cell via Defect Engineering, *J. Am. Chem. Soc.*, 2018, 140, 1358-1364.
- [64] A. Solanki, P. Yadav, S.-H. Turren-Cruz, S. S. Lim, M. Saliba and T. C. Sum, Cation influence on carrier dynamics in perovskite solar cells, *Nano Energy*, 2019, 58, 604-611.
- [65] C. Yi, J. Luo, S. Meloni, A. Boziki, N. Ashari-Astani, C. Grätzel, S. M. Zakeeruddin, U. Röhrlisberger and M. Grätzel, Entropic stabilization of mixed A-cation ABX₃ metal halide perovskites for high performance perovskite solar cells, *Energy Environ. Sci.*, 2016, 9, 656-662

Chapter 3. Investigation of Native Defects Induced Degradation in Perovskite Solar Cells Fabricated by using Control of Self-Doping Effect

3.1 Introduction.

Power conversion efficiency (PCE) of Organic-inorganic hybrid halide perovskite solar cells (PSCs) have soared over 25% and emerged as a desirable candidate as alternative of traditional photovoltaics owing to their excellent opto-electronic properties such as the tunable bandgap and long charge-carrier diffusion length from the simple fabrication method.[1-7] Despite these outstanding properties of organic-inorganic hybrid halide perovskite materials as usage of photovoltaics, PSCs suffer from instability related with decomposition of perovskite under working condition.

Oxygen and moisture have been known to be extrinsic factors of the degradation of PSCs. [8-13] To block the exposure of the external factors to PSCs, various encapsulation techniques have been employed. [14-16] Unfortunately, even encapsulated PSCs still suffer from rapid degradation, particularly under illumination conditions, implying the importance of another key factors stems from intrinsic factors in degradation. Previous studies have suggested that the trapping of excess charge-carriers and the

migration of ion are major intrinsic origins of degradation. [17-21] Illuminated conditions accelerated charge-induced ion migration and phase transformation in perovskite film. [22-25] Despite understanding that instabilities of perovskites solar cells are devoted to the excess charge-carriers and ion migrations, it is required to investigate how these intrinsic stimuli have an influence on change of intrinsic properties of perovskite at high carrier concentration condition (e.g. light illumination condition).

The soft ionic nature of the perovskite lattice induces relatively low defect formation energies, which implies significant amounts of defects in perovskite film. These defects of perovskite can be controlled to some extent depending on the fabrication method and environment. [26-30] Several studies have shown that the Fermi level (E_F) of the perovskite layer can be tuned by controlling types of defects, known as the self-doping effect. The self-doping effect in perovskites can be observed in perovskite with non-stoichiometric composition between cations and anions, fabricated by various method such as spin coating and thermal evaporation. [29-34] Though previous studies have been focused on control of the self-doping effect to employ the enhancement of PCE, its effect does not necessarily correlate with the stability of PSCs. Recent studies suggest that growth condition of perovskite material that enhance performance of PSCs may deteriorate stability. [35] Therefore, it is required to understand the impact of intrinsic native defects on long-term stability under light illumination.

Here in, we verify the charge induced photo-aging mechanism by

exploring the time dependent change of intrinsic properties of perovskite with different initial defect states. To investigate the impact of the intrinsic degradation stimuli on the photo-aging pattern, we prevent the devices from the exposure of oxygen and water moisture by using encapsulated PSCs or PSCs stored in a chamber with inert atmosphere. We fabricate perovskite films with different PbI_2 molarity of precursor to make a difference in stoichiometry, resulting in a Fermi level shift to the conduction band edge of perovskite for the Pb-rich condition. Interestingly, the fabricated PSCs with different PbI_2 molarity show similar PCEs, but different photo-aging patterns. We systematically investigate the changes in their opto-electronic properties, and difference in defect formation process between the PSCs under illumination accompanied with high carrier concentration. During charge induced aging, strain relaxation of perovskite lattice and Fermi level shift to conduction band are observed in the Pb-rich PSCs, implying the formation of defects with different energy states. Additionally, in the Pb-rich perovskite, transition of defect with shallow trap state to deep level state is observed and the formation of a deep-level defect leads to irreversible degradation, showing different photo-aging trends between the prepared PSCs. These results reveal that the PSCs with relatively rich Pb show increased non-radiative recombination and faster degradation rate by the formation of deep-level defects as the PSCs aged, whereas the relatively Pb-deficient PSCs were more defect-tolerant. The different photo-aging patterns depending on the Pb- rich and Pb-deficient condition could be attributed to the formation of the deep-

level defects related to Pb-I related defects. This study proposes importance of passivation of the deep level defect (e.g. Pb-related defects) and suggest the design principle of PSCs to be commercialized.

3.2 Experimental methods.

3.2.1 Fabrication of perovskite solar cells

Pre-patterned indium-tin-oxide (ITO) coated glass substrates ($9.5 \Omega \cdot \text{sq.}^{-1}$) were sequentially sonicated by using acetone, isopropanol alcohol (IPA), and de-ionized water for 15 min. The substrates were stored in an oven ($100 \text{ }^\circ\text{C}$) for 1 hour, followed by UV-ozone treatment for 20 min to remove organic residual. SnO_2 precursor solution was prepared by diluting a SnO_2 colloid solution (tin (IV) oxide, 15% in H_2O , Alfa Aesar) in de-ionized water (1:4 v/v). A SnO_2 layer was spin-coated on the substrate at 4000 rpm for 30 s and was then annealed on the hot plate at $150 \text{ }^\circ\text{C}$ for 1 hr. Cs-doped triple halide perovskite layer was fabricated by 2-step sequential spin-coating method. PbI_2 solution was prepared with different PbI_2 molarity (1.1 – 1.5 M). 1.1-1.5 M of PbI_2 (Dyesol) with 5 mol% of CsCl in mixed solvent DMSO and DMF (0.05 ml : 0.95 ml). 30 μl of PbI_2 precursor solution was spin-coated onto the SnO_2 at 2,500 rpm for 30 s. After spin coating process of PbI_2 layer, 300 μl mixture solution with 75 mg of FAI, 7.5mg of MABr, and 7.5mg of MACl in 1ml IPA was spin-coated at 5000 rpm for 30 s, and then annealed at $150 \text{ }^\circ\text{C}$ for 30 min. A Spiro-MeOTAD solution was prepared by mixing 72.3 $\text{mg} \cdot \text{ml}^{-1}$ of spiro-MeOTAD (Merck) in 1 ml chlorobenzene (Sigma-Aldrich)) with 28.8 μl of 4-tert-butyl pyridine(*t*-BP) and 17.5 μl of lithium bis(trifluoromethanesulfonyl)imide precursor solution ($520 \text{ mg} \cdot \text{ml}^{-1}$ of

lithium bis(trifluoromethanesulfonyl)imide in acetonitrile). 30 μl of Spiro solution was spin-coated by drop-casting at 3000 rpm for 30 s. All spin-coating processes were conducted under a relative humidity less than 10%. A 50-nm Au counter electrode was thermal evaporated. Fabricated PSCs were then encapsulated with cover glass by using UV-curable epoxy resin (XNR5570, NAGASE) in N_2 atmosphere. To fabricate electron only device for Space charge limited current (SCLC) measurement, 30nm C_{60} was deposited on FTO substrate by thermal evaporation and the perovskite films were fabricated with the same methods. C_{60} (30nm) and Au (50nm) were deposited sequentially by thermal evaporation.

3.2.2 Device characterization

The current–voltage characteristics of solar cells were measured using source-meter (Keithley 2400) and a solar simulator (Newport Oriel Sol3A Class AAA) under AM 1.5G ($100 \text{ mW} \cdot \text{cm}^{-2}$). Simulated AM 1.5G was calibrated by using a Si- cell (Rc-1000-TC-KG5-N, VLSI Standards). During measurement, all devices were covered with thin mask (active area 0.0729 cm^2). The external quantum efficiency (EQE) spectra were measured by using an internal quantum efficiency system (IQE-200B, Oriel) with 100W- Xe lamp. The long-term light stability test was carried out in reliability measurement system (K3600, McScience) which measures current–voltage characteristics every 5 minutes.

3.2.3 Thin-film characterization

The crystal structure was analyzed by using X-ray diffraction (D8-Advance, Bruker) with monochromatic Cu-K α radiation. The steady-state photoluminescence (SSPL) and time-resolved photoluminescence (TRPL) spectra of the perovskite films on glass substrate were conducted using a FluoroMax-4 spectrofluorometer (Horiba). Excitation sources were selected with a wavelength of 463 nm from a Xe-arc lamp (150W) in SSPL and 463 nm laser in TRPL, respectively. The optical properties of the perovskite film were measured using Cary 5000 UV-VIS spectrophotometer (Agilent Technologies). The Fermi level (E_F) of perovskite film were measured using X-ray photoelectron spectra (Nexsa, Thermo Fisher Scientific). To avoid sample charging, carbon peak at 248.80 eV were used as a reference standard. Atomic ratio of component in perovskite film was analyzed using X-ray fluorescence measurement (Shimadzu, XRF-1800). Depth Profile of halide ions and organic cations in perovskite were carried out using TOF-SIMS analysis (ION-TOF, TOF.SIMS 5). Bi³⁺ primary ion beam (30 keV, 0.6 pA) was used for analysis and Cs⁺ sputter beam (1 keV, 6 nA, approximately 1.1×10^{17} ions·cm⁻² dose density) was used to minimize beam induced damage. Element of ¹³CH(NH₂)₂ (Carbon-13 FA), CH₃NH₃ (MA), ²⁰⁶Pb (Pb isotope) were measured to prevent detector saturation issues and Si was selected to distinguish the interface between perovskite film and glass substrate. Cross-sectional SEM images of solar cells were obtained using FE-SEM (Nova

Nanolab, FEI). 1 nm of Pt was sputtered to avoid sample charging. Space charge limited current (SCLC) measurement was performed by Electrochemical workstation (Autolab 320N, Metrohm) with voltage range 0V to 2V. Electrochemical impedance spectroscopy (EIS) measurements were measured by using Electrochemical workstation (Autolab 320N, Metrohm) with an Autolab LED Driver Kit (Metrohm) with an AC frequency ranging from 10 to 10^6 Hz. White LEDs with intensity of $100 \text{ mW} \cdot \text{cm}^{-2}$ was used as the light source. Bias voltage ranging from 0.0 to 0.4 V was applied with 0.2 V steps. Thermal admittance spectroscopy (TAS) measurement was conducted using an Agilent 4284A precision LCR meter with a Linkam LTSE350-P probe stage. The amplitude of the AC signal was 20 mV and AC frequency ranging from 20 to 10^6 Hz was applied.

3.3 Result and discussion

3.3.1 The self-doping property of perovskite film

The self-doping effect in perovskites can be observed in perovskite with non-stoichiometric composition between cations and anions. Non-stoichiometric composition affects defect formation energy (DFE) of defects in perovskite, resulting in Fermi level (E_F) of the perovskite layer can be shifted depending on the types of native defects. [29-34] To control the kinds of native defects, we employ the self-doping effect in lead halide perovskite. Additionally, we fabricated perovskite films using a two-step sequential deposition method. Several previous studies reported that the a two-step sequential deposition method could mitigate formation of interstitial iodine in perovskite film and manage defects in the perovskite film by using tri-iodide ion additive. [36,37] We fabricated FA-based perovskite thin film using precursor solution with different PbI_2 concentration (1.1 M, 1.3 M and 1.5 M) and maintained the concentration of the organic salt in IPA. Hereafter, the fabricated perovskite films are designated by the concentration of the PbI_2 solution, respectively. By maintaining concentration of organic salt and varying the concentration of PbI_2 , the films with relatively Pb-rich and Pb-deficient condition could be fabricated. To confirm depth dependent composition difference, the depth distributions of the element in perovskite with different PbI_2 concentration were analyzed by time-of-flight secondary-

ion mass spectroscopy (TOF-SIMS). Depth-profiling of the organic cation (FA and MA) and inorganic component such as Pb and I was conducted. As shown in **Figure 3.1 a-c**, characteristics of element distribution in Pb-rich or Pb-deficient films are mainly clearly exhibited at the interface between the perovskite and glass substrate. The film with 1.1 M PbI_2 shows relatively Pb-deficient and organic cation (FA and MA)-rich at the perovskite/glass interface. On the other hands, the 1.3 M and 1.5 M films are Pb-rich and organic cation (FA and MA)-deficient in the perovskite adjacent to glass substrate. These results indicate that lattice termination of perovskite is different depending on the PbI_2 molarity. Additionally, X-ray photoelectron spectroscopy (XPS) analysis was conducted to confirm self-doping effect in fabricated perovskite films with different PbI_2 concentration. **Figure 3.1d** show distance between Fermi level (E_F) and valance band maxima (VB_M) is increase as the PbI_2 concentration is increased from 1.1 M to 1.5 M, resulting in a shift of Fermi level (E_F) shift to the conduction band edge. The results of Femi level shift to conduction band for PbI_2 rich condition are consistent with previous studies. [29-34] Thus, we confirmed the two-step sequential deposition method using precursor with the controlled PbI_2 concentration effectively induced change of elemental distribution and Fermi level in the films through self-doping effect.

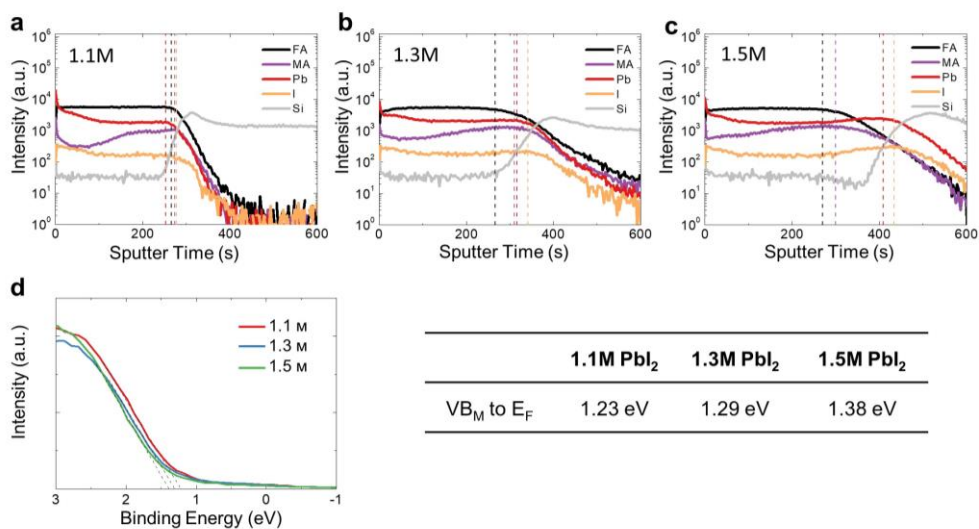


Figure 3.1 TOF-SIMS depth profiles of as-prepared perovskite film with (a) 1.1 M-, (b) 1.3 M-, and (c) 1.5 M- PbI₂ condition. Dotted lines with different color indicate the location where element of corresponding dotted line decreases. (d) XPS spectra of as prepared perovskite thin film with different PbI₂ concentration (1.1 - 1.5 M). Interception of black dotted line with X-axis indicates the energy level difference between VB_M to E_F

3.3.2. Analysis of photo-aging pattern in perovskite film

To unveil the origin of the different photo-aging mechanism in the perovskite film with different amount of Pb, the crystal structure of the perovskite films was analyzed using as prepared-film and photo aged-film in a N₂ filled chamber. As shown in **Figure 3.2a-c**, X-ray diffraction (XRD) pattern of the as-prepared and 200-hour aged perovskite films with 1.1M, 1.3M, and 1.5 M PbI₂ condition was used. All films show a diffraction peak at 12.5° corresponding to (100) PbI₂ indicating the remained PbI₂ and increases in the intensities as PbI₂ concentration becomes high. For the perovskite film with 1.1M- PbI₂ condition, the peak intensity at 14° assigned to (100) plane of α -FAPbI₃ is much higher than the peak intensity at 12.5° corresponding to (100) of PbI₂ in both the as-prepared and 200-hour photo-aged PSCs. However, both films with 1.3 M- and 1.5 M- conditions show higher peak intensity of PbI₂, indicating large amount of PbI₂ is remained in the film. After 200 hours of light illumination, all the films show a diminished peak intensity of the α -FAPbI₃ phase, indicating amorphization or phase change to inactive phase due to partial collapse of the perovskite lattice or side reaction. Particularly, in the photo-aged perovskitefilm with 1.3 M- and 1.5 M-PbI₂, magnified diffraction peaks at 28° assigned to the (200) crystal planes of the α -FAPbI₃ show shifts to low diffraction angle, implying the strain relaxation *via* defect formation. [39]

Ultraviolet-visible (UV-Vis) absorption and photoluminescence (PL)

spectra was measured to confirm changes in the optical properties of the perovskite films during the photo-aging process. During photo aging process, all films were stored in an N₂-filled chamber under 1-Sun illumination for 250 hours. The optical bandgap of perovskite was slightly enlarged as the PbI₂ concentration was increased, following previous studies (**Figure 3.2d-f**). [40,41] The opto-electrical characteristics of the perovskite film with 1.1M-PbI₂ condition was barely changed by the light compared to the high PbI₂ concentration condition. For film with 1.1 M condition, compared to as prepared film with 1.1M condition, the optical absorption spectra and PL intensity maintained the initial intensity under 1-Sun illumination after 250 hours. In addition, the increase of the PL intensity for 50hr illumination was observed. This result can be attributed to light-induced lattice expansion of perovskite or iodine related Frenkel defect (V_I⁺/ I_i⁻) annihilation. [42-44] On the contrary, the film with 1.3 M- and 1.5 M- condition exhibited decreased absorption spectra and drastic drop in the PL intensity for the same 250hr aging, indicating partial collapse of perovskite lattice and decrease of the radiative recombination due to the deep-level defect formation. [43,45,46] These observations suggest that the 1.1 M thin-film is more tolerant to the formation of deep-traps by photo-aging compared to the films fabricated with higher PbI₂ conditions.

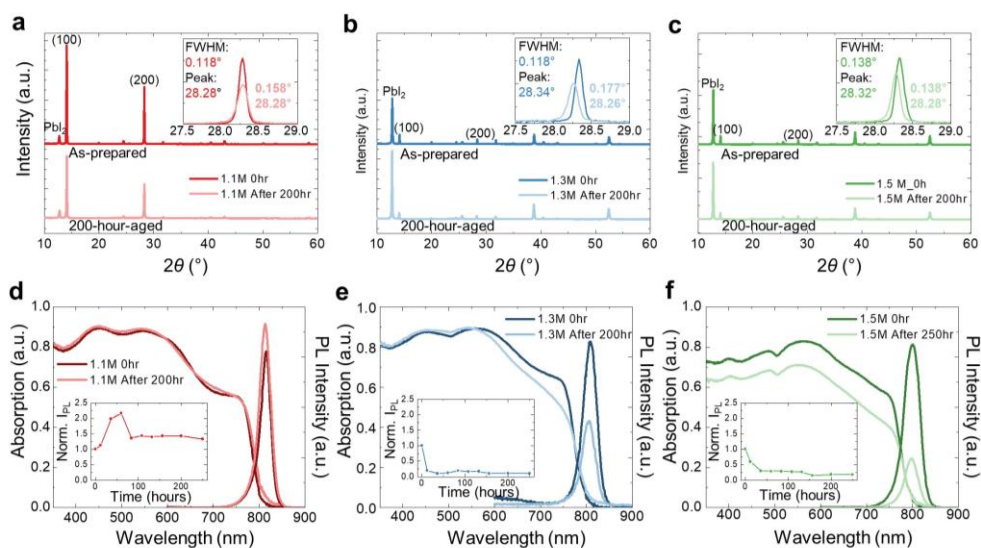


Figure 3.2. XRD pattern of as-prepared and 200-hour photo-aged perovskite films with (a) 1.1 M-, (b) 1.3 M-, and (c) 1.5 M- PbI_2 condition. Ultraviolet-visible absorption and steady state PL spectra of as-prepared and 200-hour aged perovskite films with (d) 1.1 M, (e) 1.3 M, and (f) 1.5 M- PbI_2 condition. The insets show photo-aging time dependent normalized PL peak intensity. Dark colored- and light colored- lines indicate the spectra of as-prepared and 200-hour aged PSCs, respectively.

To examine the photo-aging effect on the electronic structure of the perovskite films, X-ray photoelectron spectroscopy (XPS) measurements were conducted. As shown in **Figure 3.3a-c**, For the as-prepared thin-films, the energy difference from the valence band maximum (VB_M) to Fermi-level (E_F) in 1.1 M, 1.3 M and 1.5 M film are 1.23, 1.29, and 1.38 eV, respectively. The shift of E_F closer to conduction band is also consistent with the previous studies which reported Pb-rich perovskite layer showed donor type (n-type). [26,27,48,49] Comparing the change of E_F location in the band gap of the as-prepared film and the 200-hour aged film, the gap of the energy level between VB_M and E_F of the film with 1.1 M PbI_2 maintained after 200 hours. However, the energy level difference of photo-aged film with 1.3 M- and 1.5 M- PbI_2 condition became larger than the difference of as prepared films from 1.29 to 1.33 eV and from 1.38 to 1.48 eV, respectively, implying the formation of donor-type defects. Interestingly, although PbI_2 typically have p-type properties, E_F shift close to conduction bands after the photo-aging in Pb-rich condition was observed. Thus, E_F shift is not simply due to the PbI_2 as product, but could be attributed to the change in the energetic and spatial distribution of the defects due to the formation of a new donor-type defect state.

To investigate photo-aging induced changes in the atomic ratio of the perovskite constituent, X-ray fluorescence (XRF) measurements were carried out. **Figure 3.3d-f** and **Table 3.1** shows the photo-aging time dependent atomic ratio between halide with respect to Pb in the perovskite thin-films. As shown in **Figure 3.3d-f**, the I / Pb and Br / Pb ratios decrease as PbI_2

concentration increase in as prepared films. All 200-hour aged thin-films shows decreases in the I to Pb ratio due to the light induced iodine loss by I₂-vaporization. The I₂-vapor could be generated by charge related formation of neutral iodine interstitial defects and migration of defects. [43] On the other hands, the Br / Pb ratio barely changes during photo-aging process, possibly due to a stronger interaction between Br and Pb compared to interaction of I and Pb. [49] These results suggest that iodide vaporization in perovskite film induces formation of n-type defect, leading to the decomposition of perovskite lattice.

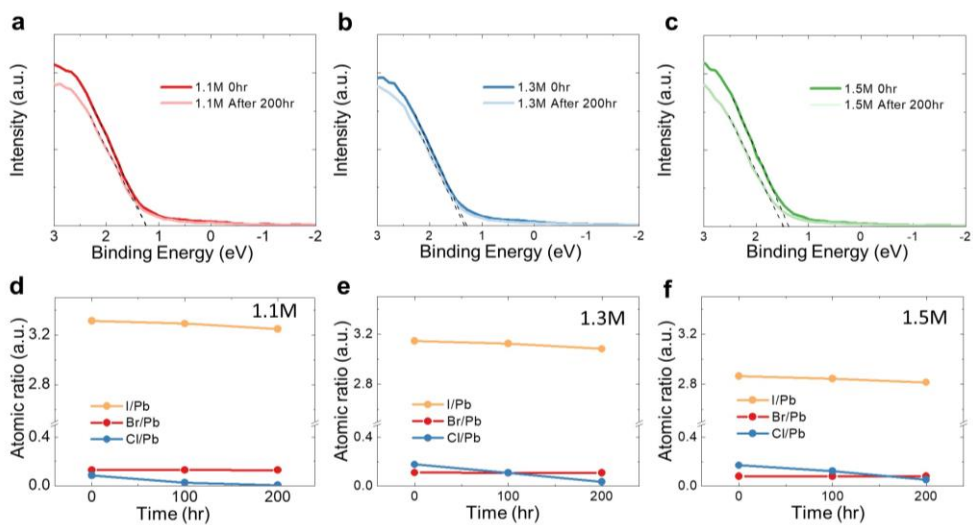


Figure 3.3 XPS spectra of as-prepared and 200-hour photo-aged perovskite films with (a) 1.1 M-, (b) 1.3 M-, and (c) 1.5 M- PbI_2 condition near the valance band (VB) region. Dark colored- and light colored- lines indicate as-prepared and 200-hour aged PSCs, respectively. Photo-aging time dependent atomic ratio of halide to Pb in perovskite with d) 1.1 M-, (e) 1.3 M-, and (f) 1.5 M- PbI_2 condition by XRF measurement.

	Time (Hours)	I/Pb	Br/Pb	Cl/Pb
1.1 M	0	3.314	0.128	0.084
1.1 M	100	3.291	0.128	0.024
1.1 M	200	3.249	0.127	0.004
1.3 M	0	3.146	0.110	0.177
1.3 M	100	3.126	0.110	0.108
1.3 M	200	3.083	0.108	0.036
1.5 M	0	2.867	0.079	0.170
1.5 M	100	2.845	0.079	0.121
1.5 M	200	2.816	0.079	0.052

Table 3.1 Atomic ratio between halide elements and lead (Pb) in both as prepared and photo-aged perovskite films with different PbI_2 concentration measured by XRF

3.3.3 J-V characteristics and light stability of perovskite solar cells

We fabricated PSCs with a planar n-i-p structure by using perovskite film with different PbI_2 concentration (1.1 M, 1.3 M, 1.5M condition). The device structure is ITO / SnO_2 / FA-base perovskite / Spiro-OMeTAD / Au. **Figure 3.4a** shows the statistical parameters of photovoltaic performance for the fabricated PSCs under each condition. The average power conversion efficiencies (PCEs) of the as prepared PSCs with 1.1 M, 1.3 M, and 1.5 M PbI_2 -concentration were shown to be 20.6%, 20.2%, and 17.3%, respectively. The J-V curves of best performing PSCs at reverse scan for the 1.1 M, 1.3 M, and 1.5 M PSCs are shown in **Figure 3.4b**. The PCEs of best performing cells (0.0729cm^2) for 1.1 M, 1.3 M, and 1.5 M PSCs is 21.4%, 21.2%, and 18.4%, respectively. While 1.5 M PSCs shows slightly lower performance, both the as prepared 1.1 M and 1.3 M PSCs exhibits similar performances. In **Figure 3.4c**, integrated short circuit current density (J_{SC}) calculated from the external quantum efficiency (EQE) measurement also show a similar trend with the measured J_{SC} of the PSCs under one sun illumination. There is a small difference between the J_{SC} from EQE measurement and the measured J_{SC} under one sun because EQE measurement didn't cover whole one sun spectrum (loss of wavelength range 300nm~350nm).

The fabricated PSCs were glass-encapsulated in a N_2 -atmosphere, and operational light stability of PSCs was tracked under a one sun illumination condition (**Figure 3.4d**). The PCE of the PSCs with 1.1 M- PbI_2

condition slightly rose up to 100 hours and maintained 90% of the initial PCEs after 500 hours under one sun illumination. On the contrary, the PCEs of the PSCs with 1.3 M- and 1.5 M- PbI_2 condition shows drastic decrease to 75% and 20% of initial PCEs after 30 hours, respectively. Particularly, although the as-prepared 1.1M and 1.3 M PSCs show similar initial PCEs, the long-term light stability of the two PSCs show significantly different patterns. These results not only imply PSCs exhibiting high performance is not directly correlated with the long-term light stability of PSCs, but also infer intrinsic factors in the PSCs with different PbI_2 concentration affect different aspect of degradation. Additionally, Electrochemical Impedance Spectroscopy (EIS) measurements were conducted to analyze the time dependent electrical characteristics in all the PSCs (**Figure 3.5**). EIS measurements of the PSCs show that the recombination resistance (R_{rec}) values in the as-prepared PSCs with 1.1 M- and 1.3 M- PbI_2 condition showed the large value compared to that of the PSCs with 1.5 M- PbI_2 condition, which implies an efficient extraction of charge carriers. After photo-aging, while the value of R_{rec} was retained in the PSC with 1.1M- PbI_2 condition, the value of R_{rec} in the PSCs with 1.3 M- and 1.5 M- PbI_2 condition showed substantial decreases of the value. Moreover, in geometric capacitances (C_g) associated with dielectric properties of the perovskite layer, C_g also showed a change in the PSCs with 1.3 M- and 1.5 M- PbI_2 condition as photo-aging time increased, indicating dielectric property in the perovskites layer increased during aging. These results are consistent with results of time evolution of PCEs.

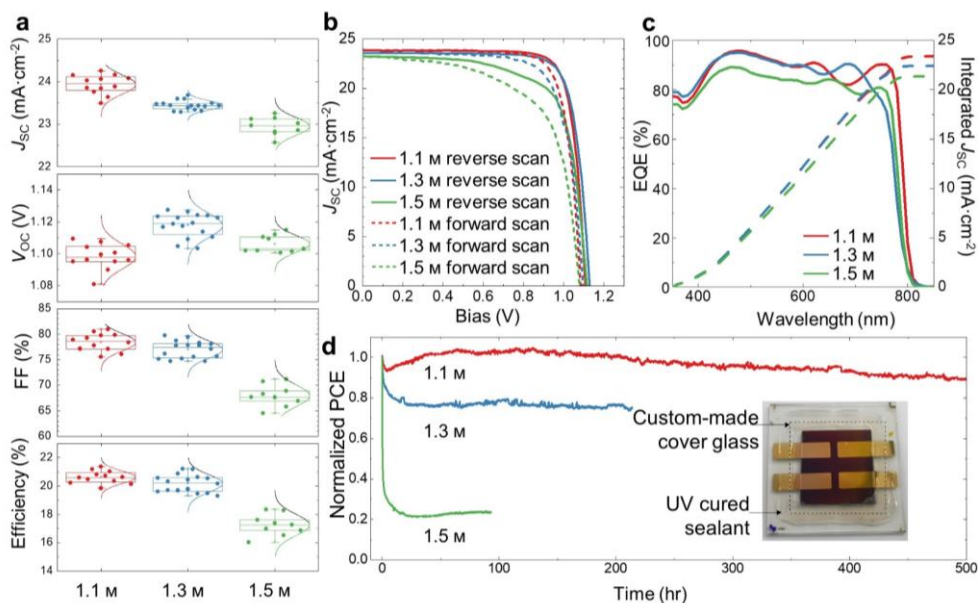


Figure 3.4. (a) statistical parameters of photovoltaic performance for the fabricated PSCs with different PbI_2 concentration. (b) J-V curves of best performing PSCs by reverse scan. (c) EQE spectra and related integrated short-circuit current density (J_{sc}) of PSCs with different PbI_2 condition. Colored line and dotted line indicate EQE spectra and integrated J_{sc} , respectively. (d) Operational stability of PSCs with different PbI_2 concentration under continuous 1-Sun illumination. All PSCs were encapsulated in N_2 atmosphere.

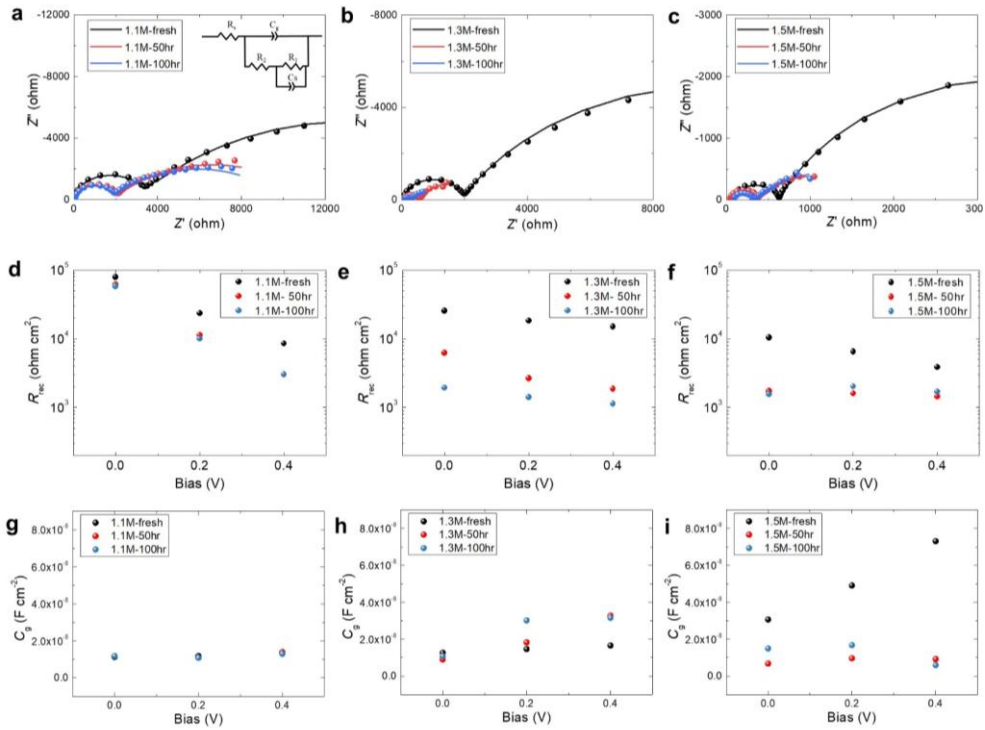


Figure 3.5 (a-c) Nyquist plots of the as prepared and 100-hour photo-aged PSCs with (a) 1.1 M-, (b) 1.3 M-, and (c) 1.5 M- PbI_2 condition, respectively. Inset shows an equivalent circuit we employed. (d-f) the recombination resistance (R_{rec}) and (g-i) the geometrical capacitance (C_g) of the as-prepared and 100-hour photo-aged PSCs with (d, g) 1.1 M-, (e, h) 1.3 M-, and (f, i) 1.5 M- PbI_2 condition, respectively.

To investigate the degradation pattern and location where degradation initiated depending on the perovskite with different PbI_2 condition, cross-sectional scanning electron microscopy (SEM) was carried out (**Figure 3.6**). For 1.1M PSCs, both as-prepared and 200-hr photo-aged PSCs with 1.1M- PbI_2 condition did not show any significant change in all layers. However, the 200-hour aged PSC shows appearance voids and PbI_2 which is indicated by black and red circle in SEM images, respectively. The voids and PbI_2 formation are observed mainly at the grain boundaries of perovskite and interfaces between perovskite and SnO_2 layer in the 200-hour aged 1.5 M perovskite layer. Previous study reported that lattice termination with MAI induces more defect-tolerant property of perovskite than a lattice terminated with PbI_2 . [50] Obtained SEM images of as-prepared and photo-aged PSCs showing degradation patterns are consistent with results of TOF-SIMS and time evolving PCEs as shown in **Figure 3.1d** and **Figure 3.2d**. In particularly, the formation of voids and PbI_2 in perovskite films with excessive PbI_2 was observed. Halide ionic defects and vacancies in the perovskite layer can interact with charges carrier, known as charged state transition, and these defects migrate from perovskite bulk to grain boundaries and surface under the illuminated condition, resulting in formation of I_2 or PbI_2 . [18,43,51,52] Therefore, after photo aging process, voids and a new phase such as PbI_2 at the grain boundaries and interfaces of perovskite also represent the existence of newly formed defects in the intra-grain region.[43] These experimental results revealed that the migration of halide ionic defects

and the halide vaporization by light illumination is closely related to the defect formation, resulting in increase of non-radiative recombination centers as observed previous results of the V_{OC} and PL decrease.[43,45,46]

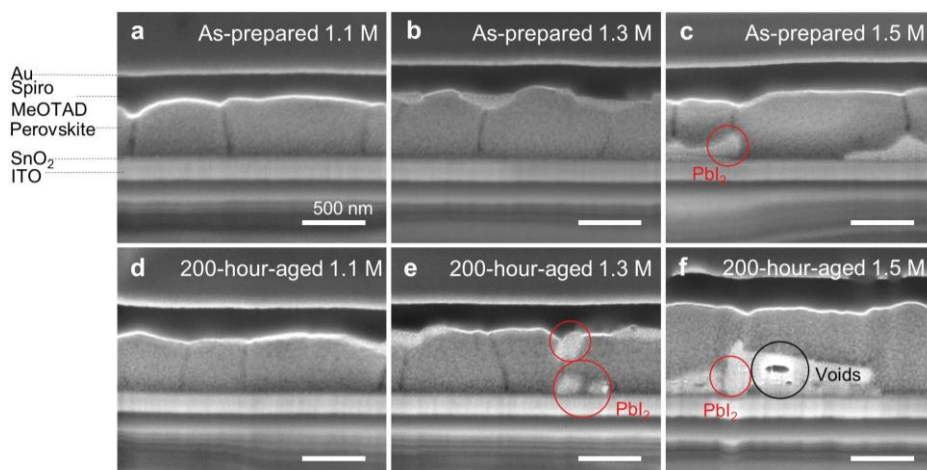


Figure 3.6 Cross-sectional SEM images of as-prepared PSCs with (a) 1.1 M-, (b) 1.3 M-, and (c) 1.5 M-PbI₂ condition. Cross-sectional SEM images of 200-hour photo-aged PSCs with (d) 1.1 M-, (e) 1.3 M-, and (f) 1.5 M- PbI₂ condition. The structure of PSCs is ITO/SnO₂/perovskite/Spiro-MeOTAD/Au. The thickness of SnO₂ layer, as-prepared perovskite layer, Spiro-MeOTAD layer, and Au layer are 30, 600, 200, and 50 nm, respectively. All scale bars 500 nm.

3.3.4 Energetic distribution of defects and estimation of possible candidates of observed defect states

Thermal admittance spectroscopy (TAS) was conducted to investigate the energetic distribution and the quantity of the defects in both as prepared- and photo-aged PSCs. [53-55] PSCs were glass-encapsulated at a N₂-atmosphere and stored in a dark for 1 hour, and then, the capacitance-frequency (C-F) curves of the PSCs were measured by applying frequencies from 100 Hz to 1 MHz with a temperature ranging from 160 to 340 K. (see **Figure 3.7**) The trap-density-of-state (tDOS) and activation energy of defect (E_A) were determined from the derivative of capacitance-frequency curves at each temperature. The activation energy (E_A) of the defect state can be deduced by fitting the corresponding Arrhenius plots from the temperature-dependent capacitance-frequency (C-F-T) spectra using the following equation:

$$\omega_T = 2\nu_0 \exp\left(-\frac{E_A}{KT}\right) \quad (1)$$

, where ω_T , ν_0 and K are characteristic transition frequencies, the attempt-to-escape frequency and the Boltzmann constant, respectively.

the energetic distribution of tDOS was obtained using the following equations:

$$E_\omega = KT \ln\left(\frac{2\nu_0}{\omega}\right) \quad (2)$$

$$N_T = -\frac{V_{bi}}{qW} \frac{dC}{d\omega} \frac{\omega}{KT} \quad (3)$$

, where E_{ω} , ω , V_{bi} , q , and W are the demarcation energy, applied angular frequency, built-in-potential of devices, elementary charge and width of depletion region obtained from the capacitance-voltage plots (Mott-Schottky analysis) (**Figure 3.7**), respectively. As shown in **Figure 3.8**, shallow trap states are located at 0.179 eV and 0.190 eV from the band edge for the as-prepared PSCs with 1.1 M- and 1.3 M- PbI_2 condition, respectively. After aging for 200 hours, the energetic distribution of tDOS for the PSC with 1.1M- PbI_2 condition show similar profiles with as prepared PSCs with 1.1M PbI_2 . For 200-hour aged 1.1M PSC, energy level of traps is located at 0.183 eV from the band edge and the tDOS near trap energy level of 200-hour photo-aged PSCs with 1.1M- PbI_2 is around $\sim 1.7 \times 10^{17} \text{ cm}^{-3} \cdot \text{eV}^{-1}$ without significant change. In contrast, the PSCs with 1.3 M- PbI_2 condition show disappearance of signal from the states at 0.190 eV and an appearance of a new defect state with relatively deep level at 0.384 eV after the 200-hour photo-aging. The trap density of the state decreases from $\sim 1.4 \times 10^{17}$ to $\sim 1.1 \times 10^{16} \text{ cm}^{-3} \cdot \text{eV}^{-1}$, showing the consistency with previous reports of a decrease of trap states after photo-aging. [55,56]

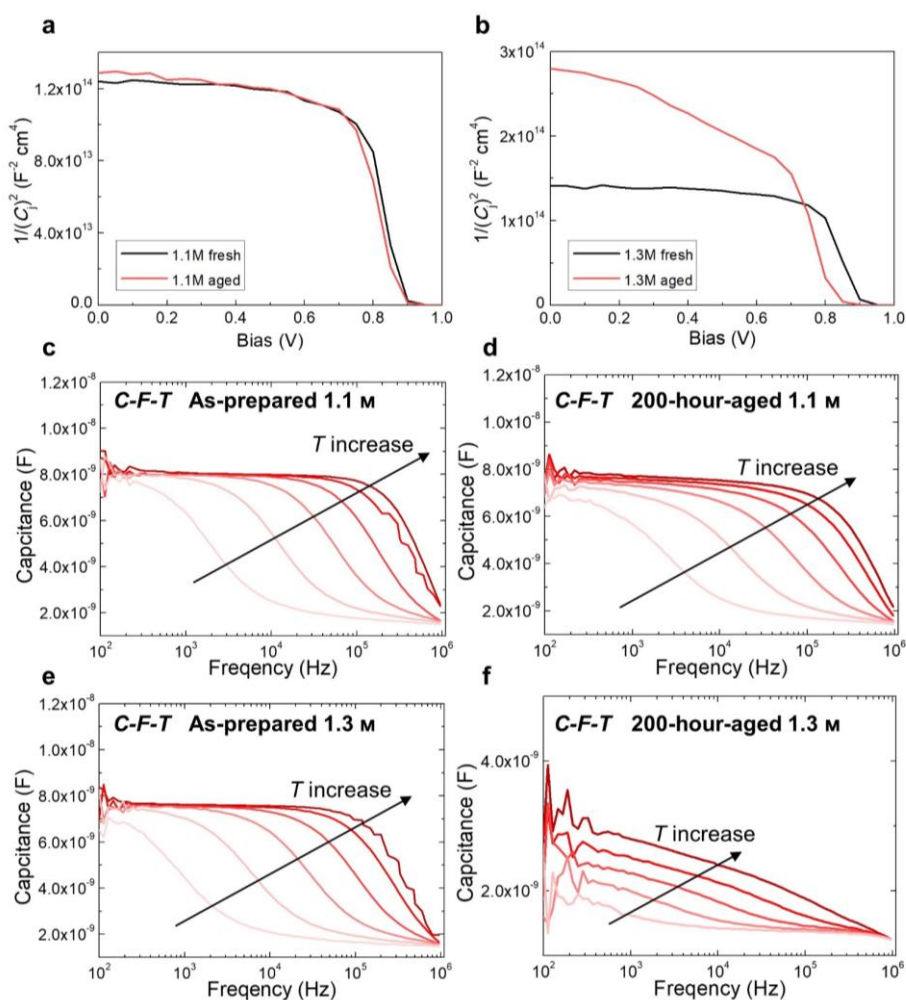


Figure 3.7 Mott-Schottky plots obtained from capacitance–voltage (C-V) scan for the as-prepared and 200-hour aged PSCs with (a) 1.1 M- and (b) 1.3 M- PbI_2 condition. Temperature dependent capacitance–frequency spectra (T-C-F) of (c) as-prepared and (d) 200-hour aged PSCs with 1.1M- PbI_2 condition. Temperature dependent capacitance–frequency spectra (T-C-F) of (e) as-prepared and (f) 200-hour aged PSCs with 1.3M- PbI_2 condition.

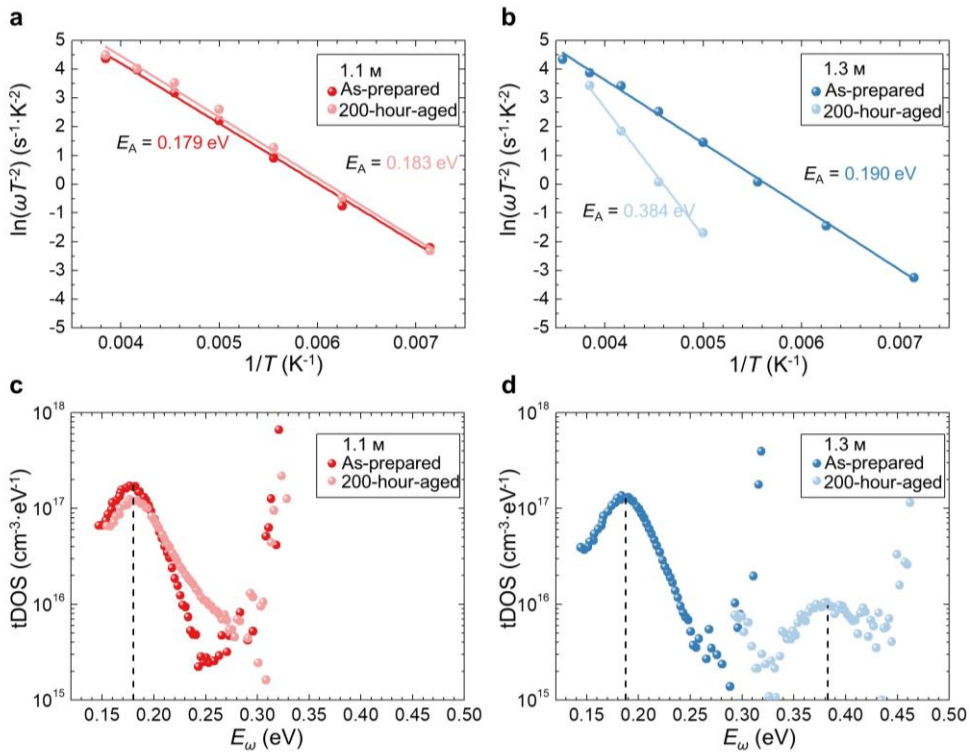


Figure 3.8 Arrhenius plot of characteristic transition frequencies to extract defect activation energies for as-prepared and 200-hour aged PSCs with (a) 1.1 M- and (b) 1.3 M-PbI₂ condition. Trap-density-of-states(tDOS) profiles for as-prepared and 200-hour aged PSCs with (c) 1.1 M- and (d) 1.3 M-PbI₂ condition, showing energetic distribution of defect states in each device. Dotted lines indicate the peak of spectra. Line and symbols with dark color and light color indicate as-prepared and 200-hour aged PSCs, respectively.

Previous studies on density functional theory (DFT) calculations are employed to estimate possible candidates for each obtained trap energy level. [47,48] Defects with low defect formation energy (DFE) have high probability of existence, and the defect formation energy depends on the composition (e.g., I-rich, Pb-rich). Based on DFT calculations, the shallow traps at 0.18 eV in PSC with a relatively Pb-deficient condition (1.1M PbI₂) can be attributed to iodine interstitial defects with acceptor type due to low DFE of iodine interstitial defects in Pb-deficient case. However, in the as-prepared PSC with a relatively Pb-rich condition (1.3 M PbI₂), the shallow traps located at 0.19eV from band edge can be associated with donor-type defects including halide vacancies (V_I), anti-site defects (FA_I), with low DFE in Pb-rich case. [48,57] For the 200-hour aged PSCs with 1.3M-PbI₂ condition, the trap state at 0.38 eV from band edge can be considered donor-type defects including anti-site defects (Pb_I) affected by iodine ionic defects migration to the interfaces, shifting Fermi level toward the conduction band edge. These under-coordinated Pb atoms and Pb-I anti-site defects at the grain boundaries and interface is known to be possible sources of the deep-level trap states. [58-60] Therefore, through our XRF measurement, TOF-SIMS depth profiling results and cross sectional-SEM images, voids and the formation of PbI₂ near the grain boundaries and interface of perovskite could be caused by the formation of Pb-I anti-site defects and uncoordinated Pb atoms. These observations reveal that the donor-type shallow defect states (e.g., V_I and FA_I) are transited to deep-trap states (e.g., Pb_I, uncoordinated Pb)

due to excess charge induced defect formation at the region where non-stoichiometry occurs (e.g. the interface and grain boundaries), and these evolved Pb- related deep level defects such as Pb_i and uncoordinated Pb deteriorate long-term stability of PSCs.

3.4 conclusion

We reveal that a perovskite solar cell (PSCs) with Pb-rich perovskite film is vulnerable to the formation of deep-trap states under light illumination condition, leading to operational instability of PSCs. Although organic-inorganic lead halide perovskite material is known to have defect-tolerant characteristics in terms of the performances, this study suggests that transition to deep level defect of perovskite in Pb-rich condition can deteriorate long-term stability of PSCs. During light illumination, donor-type (n-type) defects could be formed and these newly formed defects cause strain relaxation in perovskite lattice and increased non-radiative recombination which emit the energy in the form of phonons. The evolutions of energetic distribution of trap and the quantity of trap states suggest that the instability of PSCs in the Pb-rich condition is possibly due to the formation of Pb-I anti-site defects and uncoordinated Pb with deep donor-type defects. Particularly, although the as-prepared PSCs with Pb-rich and Pb-deficient perovskite film show similar initial performances, PSCs with Pb-deficient perovskite absorber shows an improved operational stability (90% for 500 hours) with a PCE over 21%. This study provides an understanding on the fundamental degradation mechanism of perovskite with self-doping effect based on defect dynamics and proposes rational design of perovskite solar cells for ensuring long term stability.

3.5 References

- [1] National Renewable Energy Laboratory, Best research-cell efficiency chart (2020); www.nrel.gov/pv/assets/pdfs/bestresearch-cell-efficiencies.20200218.pdf
- [2] Q. Jiang, Y. Zhao, X. Zhang, X. Yang, Y. Chen, Z. Chu, Q. Ye, X. Li, Z. Yin, J. You, Surface passivation of perovskite film for efficient solar cells, *Nat. Photonics* 2019, 13, 460.
- [3] G. Kim, H. Min, K. S. Lee, D. Y. Lee, S. M. Yoon, S. I. Seok, Impact of strain relaxation on performance of α -formamidinium lead iodide perovskite solar cells, *Science* 2020, 370, 108.
- [4] M. Jeong, I. W. Choi, E. M. Go, Y. Cho, M. Kim, B. Lee, S. Jeong, Y. Jo, H. W. Choi, J. Lee, J.-H. Bae, S. K. Kwak, D. S. Kim, C. Yang, Stable perovskite solar cells with efficiency exceeding 24.8% and 0.3-V voltage loss, *Science* 2020, 369, 1615.
- [5] G. E. Eperon, S. D. Stranks, C. Menelaou, M. B. Johnston, L. M. Herz, H. J. Snaith, Formamidinium lead trihalide: a broadly tunable perovskite for efficient planar heterojunction solar cells, *Energy Environ. Sci.* 2014, 7, 982
- [6] Q. Dong, Y. Fang, Y. Shao, P. Mulligan, J. Qiu, L. Cao, J. Huang, Electron-hole diffusion lengths $> 175 \mu\text{m}$ in solution-grown $\text{CH}_3\text{NH}_3\text{PbI}_3$ single crystals, *Science* 2015, 347, 967.

- [7] Y. Chen, H. T. Yi, X. Wu, R. Haroldson, Y. N. Gartstein, Y. I. Rodionov, K. S. Tikhonov, A. Zakhidov, X. Y. Zhu, V. Podzorov, Extended carrier lifetimes and diffusion in hybrid perovskites revealed by Hall effect and photoconductivity measurements, *Nat. Commun.* 2016, 7, 12253.
- [8] D. Bryant, N. Aristidou, S. Pont, I. Sanchez-Molina, T. Chotchunangatchaval, S. Wheeler, J. R. Durrant, S. A. Haque, Light and oxygen induced degradation limits the operational stability of methylammonium lead triiodide perovskite solar cells, *Energy Environ. Sci.* 2016, 9, 1655.
- [9] N. Aristidou, C. Eames, I. Sanchez-Molina, X. Bu, J. Kosco, M. S. Islam, S. A. Haque, Fast oxygen diffusion and iodide defects mediate oxygen-induced degradation of perovskite solar cells, *Nat. Commun.* 2017, 8, 15218.
- [10] Z. Song, A. Abate, S. C. Wathage, G. K. Liyanage, A. B. Phillips, U. Steiner, M. Graetzel, M. J. Heben, Perovskite Solar Cell Stability in Humid Air: Partially Reversible Phase Transitions in the $\text{PbI}_2\text{-CH}_3\text{NH}_3\text{I-H}_2\text{O}$ System, *Adv. Energy Mater.* 2016, 6, 1600846
- [11] J. S. Yun, J. Kim, T. Young, R. J. Patterson, D. Kim, J. Seidel, S. Lim, M. A. Green, S. Huang, A. Ho-Baillie, Humidity-Induced Degradation via Grain Boundaries of $\text{HC}(\text{NH}_2)_2\text{PbI}_3$ Planar Perovskite Solar Cells, *Adv. Funct. Mater.* 2018, 28, 1705363
- [12] G. Divitini, S. Cacovich, F. Matteocci, L. Cinà, A. Di Carlo, C. Ducati,

In situ observation of heat-induced degradation of perovskite solar cells, *Nat. Energy* 2016, 1,15012

- [13] J. Yang, X. Liu, Y. Zhang, X. Zheng, X. He, H. Wang, F. Yue, S. Braun, J. Chen, J. Xu, Y. Li, Y. Jin, J. Tang, C. Duan, M. Fahlman, Q. Bao, Comprehensive understanding of heat-induced degradation of triple-cation mixed halide perovskite for a robust solar cell, *Nano Energy* 2018, 54, 218.
- [14] F. Matteocci, L. Cinà, E. Lamanna, S. Cacovich, G. Divitini, P. A. Midgley, C. Ducati, A. Di Carlo, Encapsulation for long-term stability enhancement of perovskite solar cells, *Nano Energy* 2016, 30, 162.
- [15] R. Cheacharoen, N. Rolston, D. Harwood, K. A. Bush, R. H. Dauskardt, M. D. McGehee, Design and understanding of encapsulated perovskite solar cells to withstand temperature cycling, *Energy Environ. Sci.* 2018, 11, 144.
- [16] Y. Jiang, L. Qiu, E. J. Juarez-Perez, L. K. Ono, Z. Hu, Z. Liu, Z. Wu, L. Meng, Q. Wang, Y. Qi, Reduction of lead leakage from damaged lead halide perovskite solar modules using self-healing polymer-based encapsulation, *Nat. Energy* 2019, 4, 585.
- [17] N. Ahn, K. Kwak, M. S. Jang, H. Yoon, B. Y. Lee, J. K. Lee, P. V. Pikhitsa, J. Byun, M. Choi, Trapped charge-driven degradation of perovskite solar cells, *Nat. Commun.* 2016, 7, 13422.
- [18] Y. Lin, B. Chen, Y. Fang, J. Zhao, C. Bao, Z. Yu, Y. Deng, P. N. Rudd,

- Y. Yan, Y. Yuan, J. Huang, Excess charge-carrier induced instability of hybrid perovskites, *Nat. Commun.* 2018, 9, 4981.
- [19] J. Byeon, J. Kim, J.-Y. Kim, G. Lee, K. Bang, N. Ahn, M. Choi, Charge Transport Layer-Dependent Electronic Band Bending in Perovskite Solar Cells and Its Correlation to Light-Induced Device Degradation, *ACS Energy Lett.* 2020, 5, 2580.
- [20] T. Zhang, X. Meng, Y. Bai, S. Xiao, C. Hu, Y. Yang, H. Chen, S. Yang, Profiling the organic cation-dependent degradation of organolead halide perovskite solar cells, *J. Mater. Chem. A* 2017, 5, 1103.
- [21] D. Di Girolamo, N. Phung, F. U. Kosasih, F. Di Giacomo, F. Matteocci, J. A. Smith, M. A. Flatken, H. Köbler, S. H. Turren Cruz, A. Mattoni, L. Cinà, B. Rech, A. Latini, G. Divitini, C. Ducati, A. Di Carlo, D. Dini, A. Abate, Ion Migration-Induced Amorphization and Phase Segregation as a Degradation Mechanism in Planar Perovskite Solar Cells, *Adv. Energy Mater.* 2020, 10, 2000310
- [22] C. Eames, J. M. Frost, P. R. Barnes, B. C. O'Regan, A. Walsh, M. S. Islam, Ionic transport in hybrid lead iodide perovskite solar cells, *Nat. Commun.* 2015, 6, 7497.
- [23] W. Nie, J. C. Blancon, A. J. Neukirch, K. Appavoo, H. Tsai, M. Chhowalla, M. A. Alam, M. Y. Sfeir, C. Katan, J. Even, S. Tretiak, J. J. Crochet, G. Gupta, A. D. Mohite, Light-activated photocurrent degradation and self-healing in perovskite solar cells, *Nat. Commun.* 2016, 7, 11574.

- [24] Y. Liu, A. V. Ievlev, N. Borodinov, M. Lorenz, K. Xiao, M. Ahmadi, B. Hu, S. V. Kalinin, O. S. Ovchinnikova, Direct Observation of Photoinduced Ion Migration in Lead Halide Perovskites, *Adv. Funct. Mater.* 2021,31, 2008777
- [25] J. Yang, Q. Bao, L. Shen, L. Ding, Potential applications for perovskite solar cells in space, *Nano Energy* 2020, 76, 105019
- [26] W. J. Yin, T. Shi, Y. Yan, Unique Properties of Halide Perovskites as Possible Origins of the Superior Solar Cell Performance, *Adv. Mater.* 2014, 26, 4653.
- [27] Q. Wang, Y. Shao, H. Xie, L. Lyu, X. Liu, Y. Gao, J. Huang, Qualifying composition dependent p and n self-doping in $\text{CH}_3\text{NH}_3\text{PbI}_3$, *Appl. Phys. Lett.* 2014, 105, 163508
- [28] L. A. Frolova, N. N. Dremova, P. A. Troshin, The chemical origin of the p-type and n-type doping effects in the hybrid methylammonium–lead iodide (MAPbI_3) perovskite solar cells, *Chem. Commun. (Camb)* 2015, 51, 14917.
- [29] P. Cui, D. Wei, J. Ji, D. Song, Y. Li, X. Liu, J. Huang, T. Wang, J. You, M. Li, Highly Efficient Electron-Selective Layer Free Perovskite Solar Cells by Constructing Effective p–n Heterojunction, *Solar RRL* 2017, 1,1600027
- [30] P. Cui, D. Wei, J. Ji, H. Huang, E. Jia, S. Dou, T. Wang, W. Wang, M. Li, Planar p–n homojunction perovskite solar cells with efficiency exceeding 21.3%, *Nat. Energy* 2019, 4, 150.

- [31] A. Zohar, I. Levine, S. Gupta, O. Davidson, D. Azulay, O. Millo, I. Balberg, G. Hodes, D. Cahen, What Is the Mechanism of MAPbI₃ p-Doping by I₂? Insights from Optoelectronic Properties, *ACS Energy Lett.* 2017, 2, 2408.
- [32] T. Bu, X. Liu, R. Chen, Z. Liu, K. Li, W. Li, Y. Peng, Z. Ku, F. Huang, Y.-B. Cheng, J. Zhong, Organic/inorganic self-doping controlled crystallization and electronic properties of mixed perovskite solar cells, *J. Mater. Chem. A* 2018, 6, 6319.
- [33] B. Danekamp, C. Muller, M. Sendner, P. P. Boix, M. Sessolo, R. Lovrincic, H. J. Bolink, Perovskite–Perovskite Homojunctions via Compositional Doping, *J. Phys. Chem. Lett.* 2018, 9, 2770.
- [34] S. Xiong, Y. Dai, J. Yang, W. Xiao, D. Li, X. Liu, L. Ding, P. Gao, M. Fahlman, Q. Bao, Surface charge-transfer doping for highly efficient perovskite solar cells, *Nano Energy* 2021, 79, 105505
- [35] Y. Deng, Z. Ni, A. F. Palmstrom, J. Zhao, S. Xu, C. H. Van Brackle, X. Xiao, K. Zhu, J. Huang, J Reduced Self-Doping of Perovskites Induced by Short Annealing for Efficient Solar Modules, *Joule* 2020, 4, 1949.
- [36] W. S. Yang, B.-W. Park, E. H. Jung, N. J. Jeon, Y. C. Kim, D. U. Lee, S. S. Shin, J. Seo, E. K. Kim, J. H. Noh, S. I. Seok, Iodide management in formamidinium-lead-halide–based perovskite layers for efficient solar cells, *Science* 2017, 356, 1376.
- [37] D. G. Lee, D. H. Kim, J. M. Lee, B. J. Kim, J. Y. Kim, S. S. Shin, H.

- S. Jung, High Efficiency Perovskite Solar Cells Exceeding 22% via a Photo-Assisted Two-Step Sequential Deposition, *Adv. Funct. Mater.* 2020. 2006718
- [38] O. Gunawan, S. R. Pae, D. M. Bishop, Y. Virgus, J. H. Noh, N. J. Jeon, Y. S. Lee, X. Shao, T. Todorov, D. B. Mitzi, B. Shin, Carrier-resolved photo-Hall effect, *Nature* 2019, 575, 151.
- [39] M. I. Saidaminov, J. Kim, A. Jain, R. Quintero-Bermudez, H. Tan, G. Long, F. Tan, A. Johnston, Y. Zhao, O. Voznyy, E. H. Sargent, Suppression of atomic vacancies via incorporation of isovalent small ions to increase the stability of halide perovskite solar cells in ambient air, *Nat. Energy* 2018, 3, 648.
- [40] J. Chang, H. Zhu, J. Xiao, F. H. Isikgor, Z. Lin, Y. Hao, K. Zeng, Q.-H. Xu, J. Ouyang, Enhancing the planar heterojunction perovskite solar cell performance through tuning the precursor ratio, *J. Mater. Chem. A* 2016, 4, 7943.
- [41] Q. Jiang, Z. Chu, P. Wang, X. Yang, H. Liu, Y. Wang, Z. Yin, J. Wu, X. Zhang, J. You, Planar-Structure Perovskite Solar Cells with Efficiency beyond 21%, *Adv Mater.* 2017, 29, 1703852
- [42] E. Mosconi, D. Meggiolaro, H. J. Snaith, S. D. Stranks, F. De Angelis, Light-induced annihilation of Frenkel defects in organo-lead halide perovskites, *Energy Environ. Sci.* 2016, 9, 3180.
- [43] S. G. Motti, D. Meggiolaro, A. J. Barker, E. Mosconi, C. A. R. Perini, J. M. Ball, M. Gandini, M. Kim, F. De Angelis, A. Petrozza,

Controlling competing photochemical reactions stabilizes perovskite solar cells, *Nat. Photonics* 2019, 13, 532.

- [44] H. Tsai, R. Asadpour, J.-C. Blancon, C. C. Stoumpos, O. Durand, J. W. Strzalka, B. Chen, R. Verduzco, P. M. Ajayan, S. Tretiak, J. Even, M. A. Alam, M. G. Kanatzidis, W. Nie, A. D. Mohite, Light-induced lattice expansion leads to high-efficiency perovskite solar cells, *Science* 2018, 360, 67.
- [45] S. G. Motti, M. Gandini, A. J. Barker, J. M. Ball, A. R. Srimath Kandada, A. Petrozza, Photoinduced Emissive Trap States in Lead Halide Perovskite Semiconductors, *ACS Energy Lett.* 2016, 1, 726.
- [46] E. Aydin, M. De Bastiani, S. De Wolf, Defect and Contact Passivation for Perovskite Solar Cells, *Adv. Mater.* 2019, 31, e1900428.
- [47] A. Buin, P. Pietsch, J. Xu, O. Voznyy, A. H. Ip, R. Comin, E. H. Sargent, Materials Processing Routes to Trap-Free Halide Perovskites, *Nano Lett.* 2014, 14, 6281.
- [48] N. Liu, C. Yam, First-principles study of intrinsic defects in formamidinium lead triiodide perovskite solar cell absorbers, *Phys. Chem. Chem. Phys.* 2018, 20, 6800.
- [49] A. Buin, R. Comin, J. Xu, A. H. Ip, E. H. Sargent, Halide-Dependent Electronic Structure of Organolead Perovskite Materials, *Chem. Mater.* 2015, 27, 4405.
- [50] F. Ambrosio, D. Meggiolaro, E. Mosconi, F. De Angelis, Charge localization and trapping at surfaces in lead-iodide perovskites: the

- role of polarons and defects, *J. Mater. Chem. A* 2020, 8, 6882.
- [51] Y. Shao, Y. Fang, T. Li, Q. Wang, Q. Dong, Y. Deng, Y. Yuan, H. Wei, M. Wang, A. Gruverman, J. Shield, J. Huang, Grain boundary dominated ion migration in polycrystalline organic–inorganic halide perovskite films, *Energy Environ. Sci.* 2016, 9, 1752.
- [52] J. S. Yun, J. Seidel, J. Kim, A. M. Soufiani, S. Huang, J. Lau, N. J. Jeon, S. I. Seok, M. A. Green, A. Ho-Baillie, Critical Role of Grain Boundaries for Ion Migration in Formamidinium and Methylammonium Lead Halide Perovskite Solar Cells, *Adv. Energy Mater.* 2016, 6, 1600330
- [53] S. Khelifi, K. Decock, J. Lauwaert, H. Vrielinck, D. Spoltore, F. Piersimoni, J. Manca, A. Belghachi, M. Burgelman, Investigation of defects by admittance spectroscopy measurements in poly (3-hexylthiophene):(6,6)-phenyl C61-butyric acid methyl ester organic solar cells degraded under air exposure, *J. Appl. Phys.* 2011, 110, 094509
- [54] Y. Shao, Z. Xiao, C. Bi, Y. Yuan, J. Huang, Origin and elimination of photocurrent hysteresis by fullerene passivation in CH₃NH₃PbI₃ planar heterojunction solar cells, *Nat. Commun.* 2014, 5, 5784.
- [55] D. B. Khadka, Y. Shirai, M. Yanagida, K. Miyano, Degradation of encapsulated perovskite solar cells driven by deep trap states and interfacial deterioration, *J. Mater. Chem. C* 2018, 6, 162.
- [56] S. Heo, G. Seo, Y. Lee, M. Seol, S. H. Kim, D. J. Yun, Y. Kim, K.

- Kim, J. Lee, J. Lee, W. S. Jeon, J. K. Shin, J. Park, D. Lee, M. K. Nazeeruddin, *Adv. Mater. Origins of High Performance and Degradation in the Mixed Perovskite Solar Cells*, 2019, 31, e1805438.
- [57] D. Meggiolaro, S. G. Motti, E. Mosconi, A. J. Barker, J. Ball, C. Andrea Riccardo Perini, F. Deschler, A. Petrozza, F. De Angelis, Iodine chemistry determines the defect tolerance of lead-halide perovskites, *Energy Environ. Sci.* 2018, 11, 702.
- [58] J. Xu, A. Buin, A. H. Ip, W. Li, O. Voznyy, R. Comin, M. Yuan, S. Jeon, Z. Ning, J. J. McDowell, P. Kanjanaboos, J. P. Sun, X. Lan, L. N. Quan, D. H. Kim, I. G. Hill, P. Maksymovych, E. H. Sargent, Perovskite–fullerene hybrid materials suppress hysteresis in planar diodes, *Nat. Commun.* 2015, 6, 7081.
- [59] X. Zheng, B. Chen, J. Dai, Y. Fang, Y. Bai, Y. Lin, H. Wei, Xiao C. Zeng, J. Huang, Defect passivation in hybrid perovskite solar cells using quaternary ammonium halide anions and cations, *Nat. Energy* 2017, 2, 17102
- [60] R. Wang, J. Xue, K.-L. Wang, Z.-K. Wang, Y. Luo, D. Fenning, G. Xu, S. Nuryyeva, T. Huang, Y. Zhao, J. L. Yang, J. Zhu, M. Wang, S. Tan, I. Yavuz, K. N. Houk, Y. Yang, Constructive molecular configurations for surface-defect passivation of perovskite photovoltaics, *Science* 2019, 366, 1509.

Chapter 4. pulsatile therapy for perovskite solar cell

4.1 Introduction

As photovoltaics using hybrid perovskite material as light absorber have been updating world-records of power conversion efficiency (PCE), attention on commercialization of perovskite solar cells are rapidly soaring. [1-7] Perovskites can be employed for a various application such as flexible and wearable photovoltaics [8,9], tandem devices with Si solar cells [10], also other photo-electronic devices such as light emitting diodes [10,11] and photodetectors. [12,13] However, unfortunately, long-term stability issue that has greatly hampered the commercialization of perovskite solar cells has not been resolved yet. [14]. The current level on lifetime of the state-of-the-art device with N₂ filled encapsulation is just few thousands of hours under one sun light illumination [15-18], which is still limited when compared to that of commercialized inorganic thin film solar cell. Also, the understanding on fundamental mechanism of perovskite device degradation is still elusive.

As part of an effort to overcome this stability issue of perovskite solar cells (PSCs), many studies on degradation were reported, pointing out trapped charges and charge induced ion instabilities as the main source of device degradation. [19-22] Ionic defects are easily formed and migrated by electric field and light illumination, resulting in breakdown of materials. [23,24]

Although several reports showed a positive role of ion migration like defect annihilation [25], most of relevant studies verified instabilities induced by halide dominated migration and segregation. [26-29] Interestingly, degradation induced by ion instabilities occurred somewhat reversibly. Decreased performance which can be regarded as degradation was recovered back after storing the device in the dark chamber. But, such effects of temporary performance decrease and recovery took several hours (usually overnight) for spontaneous ion relaxation. [27,30]

Carrier charges trapped in perovskite films induce irreversible degradation in the presence of H₂O and/or O₂, leaving yellow lead iodide and lead hydroxide species as a product. [31-33] Recently, several studies investigated such accumulated charges play a critical role in irreversible device-level degradation. [21,22,34] Charge accumulation occurring in working device also caused irreversible degradation even with tight encapsulation, finally resulting in morphological breakdown and severe performance drop in device-level. [22,35] Ion instability was deeply involved with charge accumulation. [22] In this respect, better device stability was observed in device with efficient and balanced charge extraction. Excess charges also can interplay with ions (or vacancies), leading to phase segregation [22] and defect formation. These studies relevant to perovskite degradation implied the instability of perovskite device originates fundamentally from charge accumulation and ion movement, as well as their interplay. [22,34-36] Thus, the long-term stable perovskite solar cells will

require the mitigation of their negative effects on degradation.

Herein, we invented a new method (called pulsatile therapy) to revive the degraded device and lengthen its device lifetime by effectively extracting accumulated charges and regulating ion movement during maximum power point tracking (MPPT). In the therapy, a designed pulsatile reverse pulse (RP) bias is repeatedly applied in the working device for a very short time to eliminate accumulated charges as well as redistribute ionic defect reversely, leading to the stable operation of device. To systemize our pulsatile therapy (PT), we developed a pulsed-MPPT system that can apply desired pulse waves of bias voltage. The electrical parameters for period of both MPPT and RP were programmatically calculated from feedback information of actual I-V characteristics of the target cell. The system demonstrated that the PT improved total power harvested and device lifetime in comparison to the conventional MPPT case for various types of perovskite solar cells, though not fully optimized yet. Especially, effects of therapy were not only to make device degradation slower, but to restore degraded power again after a RP.

To understand the fundamental mechanism underlying our PT, we analyzed both dynamics of photoluminescence (PL) intensity and photocurrent (PC) tracking from the working device during the therapy. We confirmed charge extraction and ion redistribution from bi-exponential fitting of PL intensity and PC signals during the reverse bias step, which also accompanied steady rise of PL intensity indicating suppression of non-radiative recombination. In the following MPPT step, both PL intensity and

PC restored from their degraded values again. Based on all observations, we suggested a mechanism on degradation and recovery which is deeply involved with charges, ions, and defects. Compared to conventional MPPT operation, our PT led to improvement of total harvested energy by up to 11.3% for 500 h operation. It was reproducibly confirmed that all devices with different structures operated by PT showed better stability and energy generation than devices operated by conventional MPPT. This technical approach is the first strategy to recover the device without any pause during operation, as well as effectively enhanced total harvested energy regardless of device with different perovskite composition and charge selective layers.

4.2 Experimental Methods

4.2.1 Fabrication of perovskite solar cells

The indium-doped tin oxide (ITO) glass substrate were pre-patterned by 532nm pico-second laser to insulate 4 cells in the device. The laser power was 1.9W and the scribed line width was 300um. Patterned ITO glass substrates ($9.5\Omega\text{cm}^{-2}$) were cleaned by sonication sequentially using acetone, isopropanol, and deionized water. For the MAPbI_3 -based perovskite solar cells (PSCs) with C_{60} as the electron transporting layer (device 1), a C_{60} layer (35 nm) was deposited on the cleaned ITO glass substrate using the vacuum thermal evaporator at deposition rate of 0.2 \AA s^{-1} . For MAPbI_3 -PSCs with SnO_2 as the ETL (device 2), SnO_2 layer was fabricated on the ITO glass substrate by spin-coating 2.67wt% of SnO_2 colloid precursor (tin (IV) oxide, 15% in H_2O colloidal dispersion, Alfa Aesar) in DI water at 4000 rpm for 30 s. The SnO_2 layer was annealed at $150 \text{ }^\circ\text{C}$ for 30 min. The thickness of the SnO_2 layer was around 30 nm. A precursor solutions of MAPbI_3 were prepared by adding 461 mg of PbI_2 (Alfa Aesar) and 159 mg of MAI (Great solar) and 78 mg of mixed adducts dimethyl sulfoxide (DMSO; Sigma-Aldrich) with 5mol% urea in 0.55 mL of N,N-dimethylformamide (DMF; Sigma-Aldrich). The solution was spin-coated on the ETL layer at 4,000 rpm for 20 s with 0.5 mL of diethyl ether dripping treatment. The film was annealed at $115 \text{ }^\circ\text{C}$ for 20 min. For the Triple perovskite- based PSCs with

SnO₂ as ETLs (device 3), the triple perovskite was deposited by 2-step spin coating method. First, 1.25 M of PbI₂ with 5mol% of CsCl in 0.05ml of DMSO and 0.95ml of DMF was spin coated onto the ETL at 2,500 rpm for 30 s. The mixture solution of FAI:MABr:MACl (75 mg:7.5 mg: 7.5 mg in 1 ml isopropanol) was spin coated onto the CsCl/PbI₂ film at 5,000 rpm for 30 s, then annealed at 150 °C for 20 min. To prepare a solution for the hole-transporting layer (HTL), 72.3 mg of spiro-MeOTAD (Merck) was dissolved in 1 mL of chlorobenzene (Sigma-Aldrich). 28.8 μL of 4-tert-butyl pyridine and 17.5 μL of lithium bis(trifluoromethanesulfonyl)imide from a stock solution (520 mg of lithium bis(trifluoromethanesulfonyl)imide in 1 mL of acetonitrile, 99.8% purity, Sigma-Aldrich) were added to the mixture solution. The HTL was formed on the perovskite film by spin-coating mixture solution at 2,500 rpm for 30 s. A gold layer with a thickness of 50 nm was deposited on the HTL by using the vacuum thermal evaporator at deposition rate of 0.3 Å s⁻¹. All spin-coating processes were carried out in a dry room (<15% relative humidity, at room temperature). Fabricated solar cells were encapsulated with glass using UV curable resin (XNR5570, NAGASE) in N₂ filled glove box.

4.2.2 Characterization

I-V measurement

The current–voltage characteristics were measured by a solar simulator (Sol3A, Oriel) and Keithley 2400 source measure unit under AM 1.5G at 100 mW cm^{-2} without UV-filter at room temperature inside a glove box. The light intensity was calibrated by using a Si reference cell (Rc-1000-TC-KG5-N, VLSI Standards, USA). The aperture size of PSCs is 0.0729 cm^2 .

Long-term stability test with PT

The current–voltage characteristics for aging under 1-sun light illumination without UV-filter were measured by a solar simulator (Sol3A, Oriel) and Keithley 2400 source measure unit. Customized JIG was designed to contact cathode/anode of each cell on each independent section of etched ITO, independently. LAB View software was used to design pulsed MPPT tracking system by controlling source-meter via GPIB. The system was set to perform I-V sweep periodically (3hr or 5hr were selected), with scan rate of 0.06 V/s , scan range of $-0.1 \text{ V} \sim 1.1 \text{ V}$, voltage step of 0.04 V , and both reverse/forward direction. Recent parameters for feedback (I_{sc} , V_{oc} , R_{sh} , R_s , FF) were automatically updated and calculated based on averaged values of I-V curve for both reverse and forward direction. TMP and TP were set prior to system operation, while VRP ($-I_{sc} \cdot R_s$) and VMP were calculated by updated parameters from recently measured I-V sweep. The system also measured and stored steady-state power output (SPO), of which the sampling

rate was 0.2Hz during MPPT (record every 5sec), and 10Hz during pulse (record every 0.1sec). If a I-V sweep and a pulse overlap, I-V sweep was set as the highest hierarchy.

4.2.3. In situ photoluminescence and photocurrent system

Steady-state and kinetic photoluminescence (PL) measurements were conducted using a FluoroMax-4 spectrofluorometer (Horiba). Continuous irradiation of 150W Xe lamp with wavelength near 463 nm was used to excite our sample for PL detection. ($\sim 75 \text{ mW/cm}^2$ on a target sample). The resulting photoluminescence was measured using high-sensitivity photodetector targeting wavelength of 780 nm. Bias Voltage can be applied simultaneously by a Lab VIEW-controlled Keithley 2400. The photoluminescence by carrier recombination and photocurrent by carrier extraction flowing through the measured device will be recorded at the same time. Continuous irradiation of 150W Xe lamp was used to excite our sample for PL detection. ($\sim 75 \text{ mW/cm}^2$ on a target sample).

4.3 Results and discussion

4.3.1 effect of electrical operation conditions on device degradation

To begin with, we investigated photo-stability of three types of devices by measuring time evolution of normalized power under one sun illumination at three different electrical conditions (short-circuit (SC), maximum power point tracking (MPPT), and open-circuit (OC), respectively). (See **Figure. 4.1a**) Although configurations and photovoltaic parameters of each device were different, the fastest degradation among three conditions was observed always when the device was kept open-circuited. Detailed information about all three devices with different structure is described in **Figure 4.2**. In all three devices, the fastest degradation was observed when the device was kept open-circuited. The other two states, MPPT and SC, showed much slower degradation rates as compared to the OC cases. SC conditions led to a slightly better stability than MPPT conditions. Such bias dependency of the degradation speed was also reported in previous degradation studies [35,37].

We additionally performed photo-stability test at four different bias around initial maximum power (MP) point as shown in **Figure. 4.1b**. The result revealed that higher applied voltage led to faster device degradation. Interestingly, we observed extremely stable operation for total 100 hours under both 0.5 V and 0.65 V of applied biases (less than the initial MPP bias),

while devices working under higher voltage show significant drop of normalized power. All stable cases (SC, 0.5V and 0.65V) have current densities similar with short-circuit current (J_{sc}), which indicates that if current flows well in the device, a device can work very stably. On the contrary, when current extraction was impeded by potential barrier in all unstable cases (OC, 0.75V, and 0.8V), fast degradation of photocurrent occurred. These observations suggest that an optimal balance between charge build-up (photo-voltage) and extraction (photocurrent) will enable us to harvest maximal power from a device even more than MPPT. Also, such bias-dependent operational stability confirms again that both charge accumulation and bias-induced ion migration, which are more reinforced at higher biases, play decisive roles in causing severe degradation of perovskite solar cells [21,38] (see **Figure. 4.1c**).

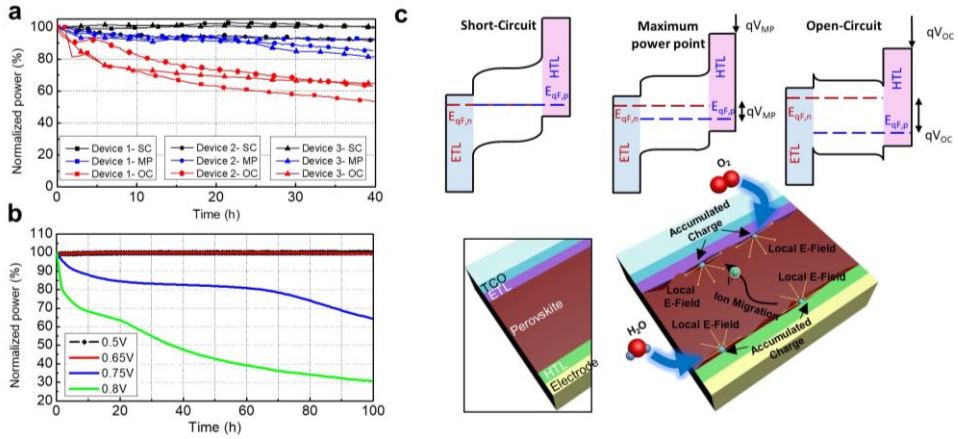


Figure 4.1. (a) Time evolution of the normalized power of three different types of encapsulated devices measured at SC (short circuit), MPPT (maximum power point tracking) and OC (open circuit) condition under one sun illumination in ambient condition (30% of Relative humidity). I-V scans were done every five hours. (b) Time evolution of the normalized power of the device type 3 measured at four different voltage biases around MPP (maximum power point). 0.5 V (black), 0.65 V (red), 0.75 V (blue), 0.8V (green). (c) A schematic illustration describing the effect of voltage bias on charge accumulation, ion migration, and the resulting degradation. All devices were glass-encapsulated in N₂-filled glove box

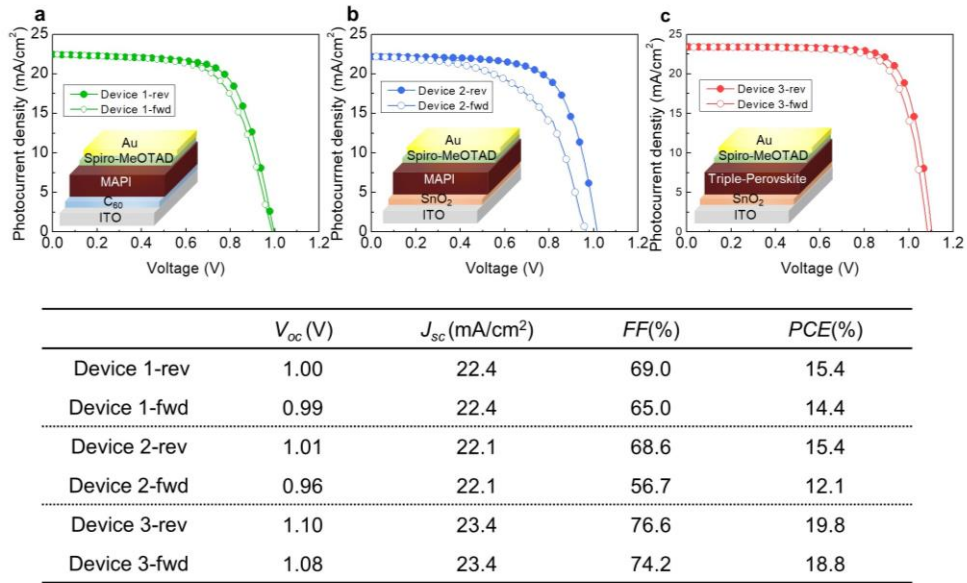


Figure 4.2 J-V characteristics of (a) device type 1 (ITO/C₆₀/MAPbI₃/HTL/Au), (b) device type 2 (ITO/SnO₂/MAPbI₃/HTL/Au), (b) device type 3 (ITO/SnO₂/Triple-perovskite/HTL/Au) measured under both reverse (full circle) and forward (hollow circle) scan. Spiro-MeOTAD was employed as hole transporting layers (HTLs) for all devices. Photovoltaic parameters are summarized in the bottom table.

4.3.2 Design of pulsatile therapy and its efficacies

Considering perovskite solar cells can be stabilized with appropriate electrical operation, we invented a pulsed-MPPT system to lengthen device lifespan and harvest more power, which is practically applicable without stopping operation. To extract the charges accumulated and re-distribute ions migrated during a period working at V_{MP} (MPPT operation), a short reverse pulse (RP) bias is applied periodically by our programmed algorithm in our pulsed-MPPT system. As illustrated **Figure 4.3** Based on a simple circuit model including a capacitance corresponding the accumulation of charges, the value of applied RP bias is designed to mitigate potential difference across a perovskite layer and updated periodically, thereby, we can obtain optimal pulse amplitude for our pulsatile tracking system (**Figure 4.4**). The value of $-I_{sc} \cdot R_s$ of three types of devices is very similar with reverse voltage bias (-0.2V), which means that the bias (reverse bias) applied in our pulsatile therapy could effectively neutralize the capacitor. In the system, an I-V scan is conducted with every 3 or 5 hours, followed by an automatic evaluation of device status. Through feedback signal from an updated I-V curve, bias amplitudes of MPPT and reverse pulse (RP) are calculated and updated to next power harvesting steps. In the harvesting stage, MPPT and short reverse pulsing steps alternately repeat until next I-V scan. **Figure 4.3a** illustrates the whole process of a pulsed-MPPT system.

In **Figure.4.3b** we show an actual operation of the system with an

applied bias voltage and corresponding photocurrent extracted from a device over time. An amplitude of MPP bias (V_{MP}) is updated based on a newly measured I-V curve. As mentioned earlier, this system uses recently-updated I-V characteristics to calculate MP and pulse bias. During power harvesting, applied bias over time will be a simple pulse wave (rectangular wave) that has an amplitude of maximum power voltage (V_{MP}) in a forward bias. In the RP process with an amplitude of V_{RP} , electrical power will be consumed to apply RP, but energy loss will be far lower than energy harvesting as weak reverse biases are applied for a much shorter time than energy harvesting process. Power losses occurred during RP are strictly included for precise comparison. We will call this novel operational method as pulsatile therapy (PT) and investigate efficacies of PT

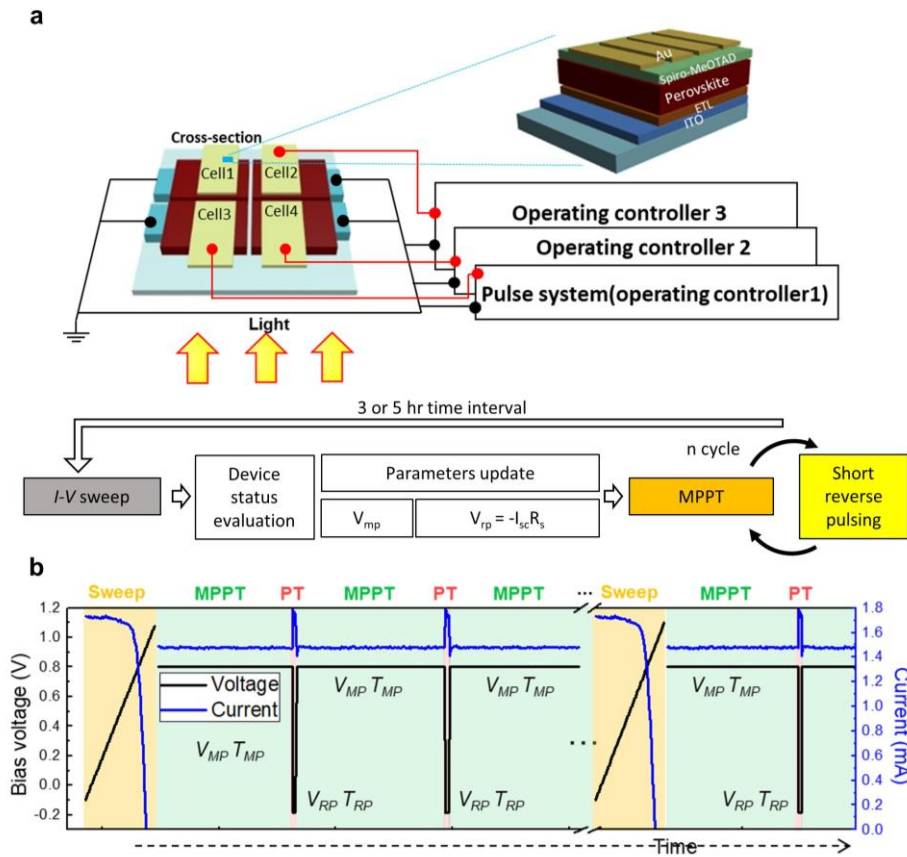
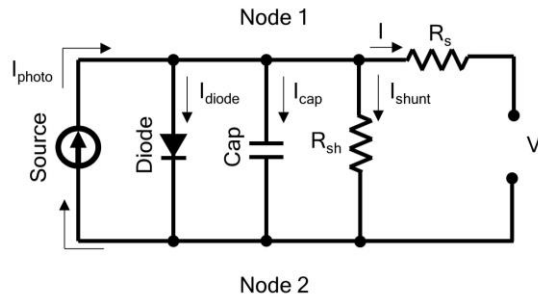


Figure 4.3. (a) A schematic illustration of our novel system for pulsatile therapy and its basic algorithm. Therapy consist of I-V scans, maximum power point tracking (MPPT), and short pulsatile therapy (PT). (b) The profile of applied bias voltage and corresponding photocurrent over time stored in our system. To heal a working device, the reverse pulses ($V_{RP} = -I_{sc} \cdot R_s$) were applied during the middle of MPPT. V_{MP} : Maximum power point voltage, T_{MP} : Time duration for maximum power point voltage, V_{RP} : Reverse pulse voltage, T_{RP} : Time duration for reverse pulse voltage. I_{sc} : short-circuit current, R_s : series resistance



- V_{RP} for zero electrical potential, assuming $I \sim I_{sc}$

$$\Delta V_{12} = I_{sc} R_s + V_{RP} = 0$$

$$V_{RP} = -I_{sc} R_s$$

Figure 4.4 A simple equivalent circuit including a parallel capacitor corresponding accumulation of charged ones

We tested the efficacy of PT for (Cs_{0.04}FA_{0.931}MA_{0.029})Pb(I_{2.91}Br_{0.09}) perovskite solar cells with 20% of PCE (device type 3). For the first PT test, its time duration for MPPT (T_{MP}) and RP (T_{RP}) was fixed at 30 minutes and 30 seconds, respectively. Standard MPPT was simultaneously performed for the other identical cell in the device. **Figure 4.5a** shows time evolution of normalized power for PT- and MPPT- tested cells. While normalized power of the cell with PT maintained 93% of the initial power in 40 hours, that of the MPPT-cell decrease by 89.5% of the initial power (will show later for a long-term operation). To verify RP effect on device performance, we observed kinetics of normalized power before and after a RP during 2-3 h and 16-17 h. **Figure 4.5b** shows that normalized power linearly decreased for both MPPT and PT cases, in which the decay speed of the PT (0.97 % h⁻¹) was slower than that of the MPPT case (1.31 % h⁻¹). Namely, the PT slows degradation down, which is the first efficacy of the PT. After some progression of degradation (16 h), we could observe another signal to show its efficacy. As can be seen in **Figure 4.5c**, degraded power during MP was dramatically restored shortly after a RP, whereas the recovery was not observed in MPPT operation. Performance recovery in degraded devices was observed when the device was stored in dark conditions for overnight, which would be in line with PT-induced recovery. [39-41] However, an intriguing point is that our PT can restore degraded performance in just 30 seconds without pause of operation. The recovery is shown to become pronounced with aging, which would be attributed to the recovery from ion defects

increased with time by the reverse biases. Interestingly, these short-term experimental results shown in **Figure 4.5b-c** reveal that the treatment of periodic reverse biases in our PT technique not only effectively slows down irreversible degradation caused by accumulated charges, but also recovers degraded performance back owing to defect healing.

As clinical trials on the PT, different device stacks were tested in the same way. Pure MAPbI₃ solar cell employing vapor-deposited C₆₀ as ETL (device type1) was also stabilized by PT as soon as the test started. (see **Figure 4.6a**) The kinetics of normalized power over time were similarly observed in terms of photocurrent recovery after RPs. (**Figure 4.6b**) The SnO₂/MAPbI₃/Spiro-MeOTAD device was also stabilized by PT. (**Figure 4.6c**)

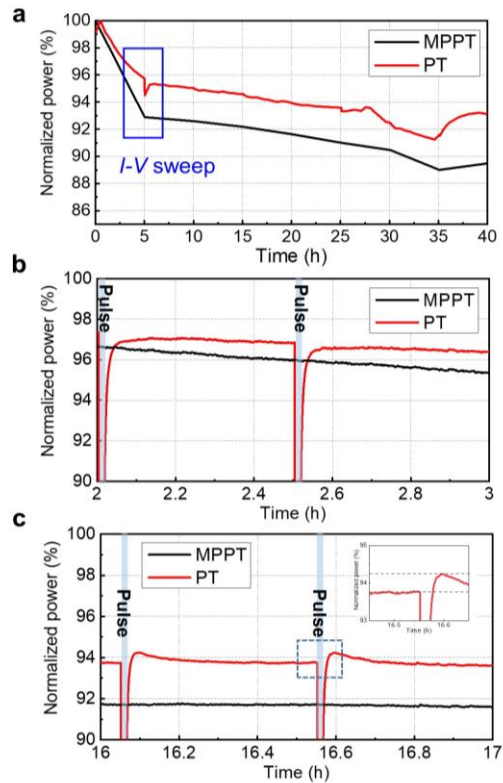


Figure. 4.5. (a) Time evolution of normalized power for MPPT- (black) and PT (red)-tested cells. Profiles of normalized power for PT- and MPPT- tested cells during (b) 2-3 h of operation time. and (c) 16-17 h of operation time. The inset image is the magnified profile of the selected region showing the effect of short pulse. In this test, the I-V sweep was done every 5 hours to update I-V characteristics of the target device. The sudden change of normalized power at around 5 h occurred due to the significant change in maximum power point of the target device.

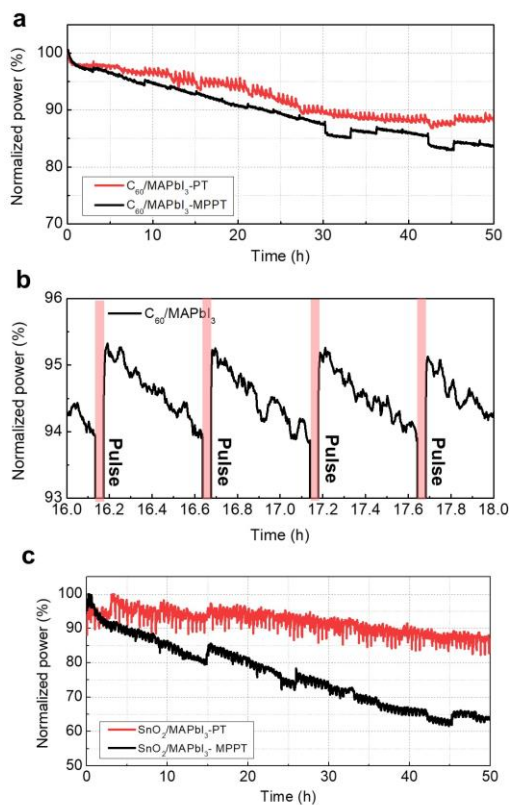


Figure 4.6 (a) Time-evolution of normalized power of the $C_{60}/MAPbI_3$ /Spiro-MeOTAD device (device type 1) tested under PT (red)- and MPPT (black)-conditions. (b) The profiles of normalized power of the $C_{60}/MAPbI_3$ /Spiro-MeOTAD device tested under PT-condition during 16-18 h of operation time. (c) Time-evolution of normalized power the $SnO_2/MAPbI_3$ /Spiro-MeOTAD device (device type 2) under PT (red)- and MPPT (black)-condition.

To reveal the mechanism underlying PT efficacies, we customized photoluminescence (PL) setup to detect time evolution of PL emission from the device controlled by PT as illustrated in **Figure 4.7a**. The desired voltage bias can be applied by a Lab VIEW-controlled Keithley 2400 source measure unit (SMU) and photo-current (PC) flowing through the measured device will be recorded at the same time. Continuous irradiation of 150 W Xenon lamp was used to excite our sample for PL detection. ($\sim 75 \text{ mW/cm}^2$ on a target sample). Using the new setup, we investigated the kinetics of PL and PC during MPPT operation in hour-scale (see **Figure 4.7b**). We observed the extremely steep decay of PL and PC signals appearing at the beginning of the measurement, which was due to transient change of applied bias and light excitation. After the fast transient decay, continuous decreases of both PL intensity and PC were observed until the end of the measurement. It literally indicates a degradation of the perovskite device during MPPT operation. The reduction of PL intensities over time could be explained by the augmentation of deep-level defects where non-radiative recombination occurs. [36,42] In the early stage before 1000 seconds, PC dynamics has a sharp decay, which could be attributed to ion accumulation to form a Coulombic barrier preventing charge extraction. [43] We also detected time-evolving PL intensity and PC for 30 seconds during a RP applied after 30 minutes of MPPT operation (see **Figure 4.7c**). The dynamics of both PC and PL intensity induced by a short RP are well fitted by bi-exponential functions with similar time-constants (see **Table.4.1**), of which the fast and slow ones result from

capacitive current due to discharging of accumulated charges and field-induced ion movement, respectively. [44] The increase of PL intensity during the RP in **Figure. 4.7c** indicates that non-radiative recombination is reduced during 30 sec of RP (see the black and blue arrows in **Figure. 4.7d**), which is indicative of defect healing. Clear evidence of defect healing by RPs is shown in overall kinetics of PL intensity and PC during one cycle of PT (MP→RP→MP). (see **Figure. 4.7d**) It was confirmed that both PL intensity and PC were saturated at higher values than the values at the last minute of the previous MP process, which is consistent with recovery of normalized power after RPs shown in **Figure. 4.5c**. These results reveal that the RP effectively extracts carrier charges and releases ion accumulation without any pause of operation, finally leading to the defect annihilation and the reduction of non-radiative recombination. Therefore, the PT stabilized the damaged device again after every RPs, thereby device degradation was delayed and performance recovery occurred. Note that photocurrent recovery after RPs could be almost invisible during the measurements depending on device status (**Figure 4.5b-c**), as the magnitude of photocurrent recovery depends on the level of ion defects. Even in the case, defect healing may always take place during the PT, which was evidenced from the discernible recovery of PL intensity.

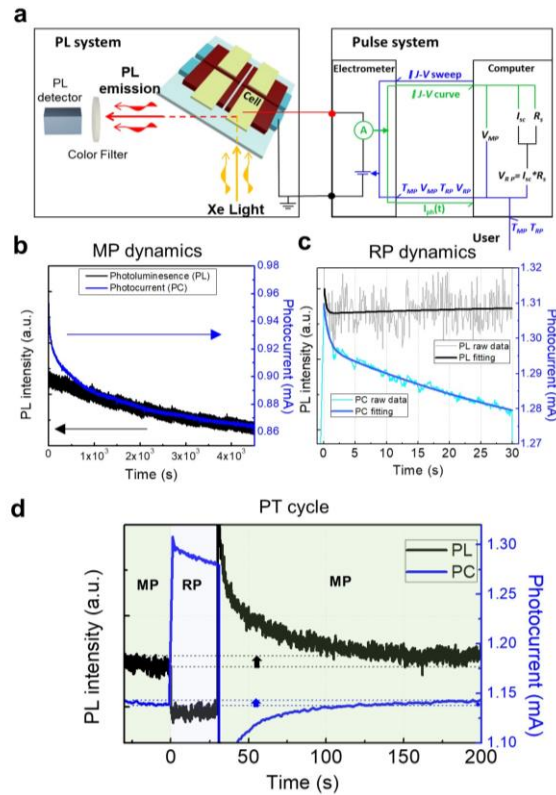


Figure 4.7 (a) A schematic illustration of in-situ photoluminescence (PL) and photocurrent (PC) measurements combined with the PT system. (b) Dynamics of PL intensity (black) and PC (blue) of the device operating under MPPT condition for over 4000 seconds. (c) Dynamics of PL intensity (grey) and PC (cyan) of the PT-tested device during 30 seconds of pulsatile therapy after 30 minutes of MPPT operation. Both profiles for PL intensity (black) and PC (blue) were fitted by bi-exponential components with similar time-constants. (d) Overall kinetics of PL intensity and PC during the pulsatile therapy (V_{MP} - V_{RP} - V_{MP}). Black and blue arrows point out restoration of PL intensity and PC, respectively, indicating device healing induced by short reverse pulses.

	Reverse pulse		MP after reverse pulse	
	T1 (s)	T2 (s)	T1 (s)	T2 (s)
Photocurrent (PC)	0.775	47.57	0.700	17.24
Photoluminescence(PL)	0.101	52.32	0.422	18.37

Table S4.1 Time constant extracted from kinetics of PL intensity and PC during RP (30 sec) and MP (30 min) operation after RP, respectively. During the RP step, both PL intensity and PC were fitted by bi-exponential function, in which the fast one resulted from capacitive current and the slow one resulted from field-induced ion movement

4.3.3 Long term effect of pulsatile therapy

Clear efficacies of PT were demonstrated for the 40 h tests in **Figure 4.5**. However, it is required to confirm efficacies of PT for long term scale up to 500 hr. Therefore, we additionally conducted a total of six sets of the long-term stability tests for up to 500 h under continuous illumination to prove technical values of PT and its reproducibility. (3 sets for 100 h, 3 sets for 500 h). **Figure 4.8a** presents one of representative profiles of normalized power as a function of time for MPPT, PT. Device in PT condition show better stability compared to device in MPPT condition and the effect became pronounced. At 500 h, both device in PT condition maintained 72.3% of their initial power, while only 62% of the initial power was retained in the device operated by MPPT condition. To evaluate technical value of our PT, we estimate total gain that corresponds to how much total energy harvested by PT operation relatively improve over MPPT operation (See calculation of total energy gain in Note 1). Total gain is time-dependent because efficiency continuously changes and power consumption during RPs should be considered together. Thus, if total gain finally exceeds 0%, PT is technically meaningful PT achieved total energy gain of 11.3% at 500 h as shown in **Figure 4.8a**

Using total of six sets of the long-term stability tests, can quantitatively evaluate relative improvements between their initial performance (operational stability) and total harvested energy when devices

is tested with PT. **Figure 4.8b** shows statistical results for a relative improvement of operational stability, which is calculated by following equation.

$$\text{Rel. Imp (RI)} = (\eta_{PT} / \eta_{MPPT} - 1) \times 100 (\%)$$

η_{PT} and η_{MPPT} are normalized power of the PT-tested and the MPPT-tested device, respectively. All six sets showed positive RI values at the 100hr and 500 h respectively, representing that the operational stability was always improved with PT in the long-term. The improvements of the operational stability are directly related to additional gains of total harvested energy. We estimate total energy gain (%) over time of all tested sets as shown in **Figure 4.8c**. (See **Note 1**). Due to energy loss during RPs, the total energy gain shows negative values at the early stage of the long-term test. However, by benefitting from high efficacy of PT, the total energy gain exceeded 0% from a certain time and increased until the end of the test. The total energy gain will increase even after 500 h due to a widening efficiency-gap between MPPT and PT.

We additionally investigated time evolution of I-V curves for MPPT, PT, respectively (**Figure 4.8d** and **4.8e**). In **Figure 4.8d**, we exhibited the I-V curves (solid lines) of the device at the beginning and the end of the MPPT test together with simulated curves (dashed lines) using the circuit modeling. As degradation continued, a peculiar shape of I-V curves (twice-deflected) started to appear only in the case of MPPT. The corresponding conductance-voltage curves were shown together in the bottom to certify two clear

deflections. In the peculiar I-V curves, there exist two clear deflections points at around 0.5 V and 0.9 V. This could be interpreted as a result of an activation of an additional diode from the viewpoint of electrical circuit (**Figure 4.9a** and **Table 4.2**). [45,46] the peculiar shape likely originates from the emergence of a trap-assisted recombination pathway as modeled by secondary non-radiative diode and resistance. [45,46] An increase of traps during MPPT operation lets trap-assisted recombination happen more and easier, leading to lowering the resistance and increasing carrier losses at secondary diode. **Figure 4.8e** displays the measured I-V curves with simulation results (top) and the corresponding conductance-voltage (S-V) curves (bottom) of the device tested by the PT method. Interestingly, compared to MPPT case, I-V curves for PT continuously keep their typical diode shapes until 500 hr. Thus, the I-V curve at 500 h was well fitted by using a single diode circuit modeling (**Figure 4.9b** and **Table 4.3**). Based on observation and simulation results. An increase of traps during MPPT operation lets trap-assisted recombination happen more and easier, leading to lowering the resistance and increasing carrier losses at secondary diode. That is, the modeling suggests that continuous MPPT operation induced the formation of defect acting as trap-site, leading to twice-deflecting I-V curve. On the other hand, PT can not only suppress charge trapping but also mitigate the formation of defects through charge extraction and ion redistribution, which would be why we observed the normal shape of I-V curves even at 500 h of operation in the case of PT

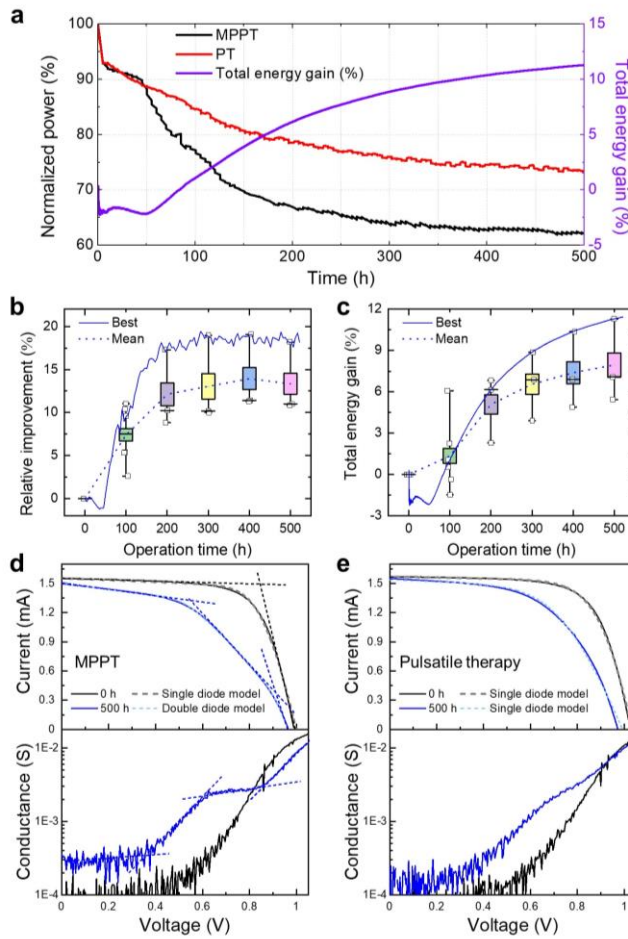


Figure 4.8 (a) Time evolution of normalized power and total gain(violet) of the representative test set of total test sets working for 500 h under MPPT (black)-, PT (red)- condition under one sun illumination. (b) A statistical plot of total test sets for relative improvements (RI) of operational stability by pulsatile therapy. A blue dashed line indicates the best-performing PT. (c) A statistical plot for total energy gain of the PT. Total energy gain is defined as a relative improvement of total harvested energy of the PT as compared to the MPPT case. The PT acquires technical values where its total energy gain exceeds 0%. Measured I-V curves (solid lined) and simulated I-V curves of

the devices tested under the MPPT operation (d) and the PT operation (e) at 0 h (black) and 500 h (blue), together with corresponding conductance-voltage(S-V) curves to certify a peculiar I-V shape with two deflections. I-V simulation was conducted based on our equivalent circuit modeling. The I-V curve with two deflections (500 h, MPPT) requires double diodes for its simulation, while the other curves are simulated with a single diode.

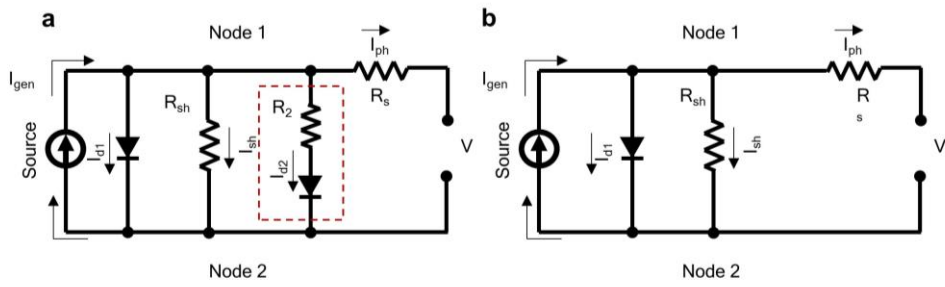


Figure 4.9 Equivalent circuit based on (a) double diode and (b) single diode modeling. I_{gen} , R_s , I_{ph} , R_{sh} , I_{sh} , and I_{d1} indicate source current, series resistance, photocurrent, shunt resistance, shunt current and diode current, respectively.

Fitting parameter	I_{gen} (mA)	R_s (Ω)	$V_{on,1}$ (V)	R_{sh} ($k\Omega$)	$V_{on,2}$ (V)	R_2 ($k\Omega$)	RMSE
100 h	1.579	67	0.9074	3.009	0.6824	0.3405	0.0144
200 h	1.537	68	0.9144	3.002	0.6376	0.3109	0.0077
500 h	1.536	69	0.9366	3.001	0.6205	0.3076	0.0057

Table S4.2 Fitting parameters of double diode modeling for MPPT case at 100 h, 200 h and 500 h operation.

Fitting parameter		I_{gen} (mA)	R_s (Ω)	$V_{on,1}$ (V)	R_{sh} ($k\Omega$)	$V_{on,2}$ (V)	R_2 ($k\Omega$)	RMSE
MPPT	0 h (Single)	1.565	64.22	0.8644	10.00			0.0126
	500 h (Double)	1.536	69.00	0.9366	3.002	0.6205	0.3076	0.0053
PT	0 h (Single)	1.575	42.45	0.8356	20.00			0.0106
	500 h (Single)	1.557	122.4	0.7649	9.974			0.0175

Table S4.3 Fitting parameters of simulated I-V curves for fresh (0hr) and 500-hour-aged PSCs under MPPT- and PT-condition.

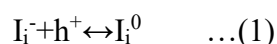
Efficacies of the PT were also confirmed in X-ray diffraction (XRD) patterns of PT-tested and MPPT-tested devices (device 3). **Figure 4.10a** shows XRD patterns of the 300 h MPPT-tested device (top, red), the 300 h PT-tested device (middle, blue), and the fresh device (bottom, black), respectively. In the fresh device, the FA-based perovskite has a cubic Pm-3m phase of which peaks are indexed according to the previous studies. [16,24] Although the cubic phase remained after 300 h of continuous operation for both cases due to better structural stability of FA-based perovskites, significant changes in the position of (100) peak at 14° were observed in the MPPT-tested device (see **Figure 4.10b**). This shift originates from a distortion of crystal structure due to an additional strain, indicating increased defects during degradation process. On the other hand, the PT-tested device showed a slight change of the peak position despite the same time operation. This is clear evidence of effective suppression of defect formation in our PT treatment. It was also observed that a relative intensity of the PbI_2 peak appearing at 12.5° was increased by a lot only in the case of the MPPT operation, which is indicative of additional formation of PbI_2 species during the MPPT operation. This suggests an increased number of defects may trigger further production of PbI_2 .

Morphological changes of the perovskite surfaces were examined and compared between operational conditions (See **Figure 4.10c-e**) We observed much more voids and white region in a surface scanning electron microscopy (SEM) image of the 300 h MPPT-tested perovskite film

compared to the PT-tested perovskite, implying a considerable amount of produced PbI_2 (white region) and gas I_2 (voids), whereas the PT effectively mitigate the morphological changes. This is well consistent with above XRD results.

4.3.4. Defect healing mechanism underlying pulsatile therapy

We propose a possible mechanism underlying the PT based on dynamics of lead and iodine interstitial defects, as shown in **Figure 4.10f**. When a perovskite device operates at MPPT under light illumination, charge carriers, ions, and defects in a perovskite film will move by diffusion-drift model [47,48]. As a result, both carriers and ions could be localized at both interfaces, leading to device degradation. The localization can be more severe due to Coulombic interaction between carriers/ions. In this condition, the defect formation energies (DFEs) of I_i^0 become lower than those of I_i^{-1} , which means that charge-state transition can be energetically favorable as the following reactions [36,49-52];



Such reactions happen slowly, but steadily during MP operation. The neutral interstitial defects (I_i^0) occupy deep-level states within bandgap, which supply sources of non-radiative recombination. [53] As a result, both PL intensity and PC decrease as shown in **Figure. 4.7b**. The degradation continues as the MP operation is maintained. However, the PT has special

steps to apply reverse pulses periodically. If a RP is instantaneously applied during our PT, ions will reversely move from the previous MP step together with efficient extraction of charge carriers. As a result, the charge-state transition will occur oppositely because the neutral interstitial defects are no longer energetically favorable when electrons or holes vanish out by the RP. Therefore, deep-level defects could return to shallow defects like I_i^{-1} again, which well explains our observation of defect healing in our PT. Similarly, neutral interstitial iodide (I_i^0) by halide oxidation with holes was suggested as a main mechanism of reverse bias induced degradation and healing process in dark. [52,53] The reaction produces neutral interstitial iodide (I_i^0), triiodide (I_3^-) and iodine (I_2). [36,54-57] It was verified that our PT can stabilize devices by delaying halide-involved reactions.

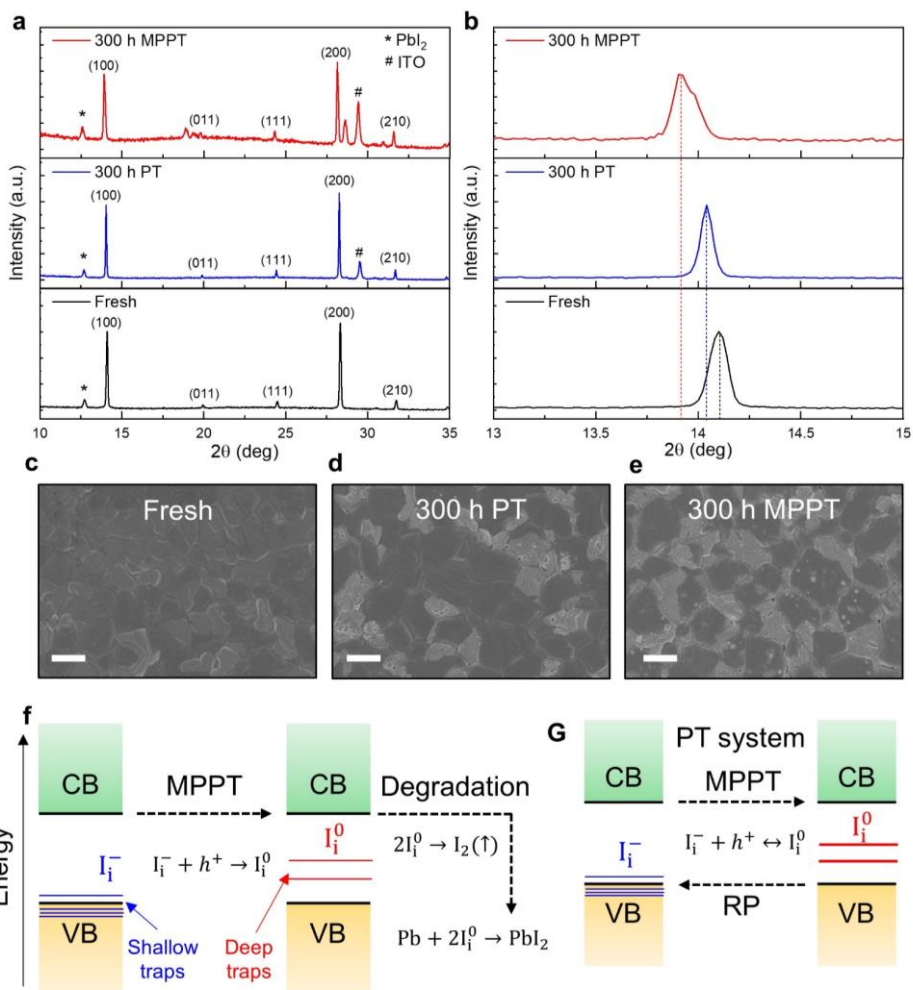


Figure 4.10 (a) X-ray diffraction (XRD) patterns of the fresh (black), the 300 h PT-tested (red), and the 300 h MPPT-tested devices, respectively. Intensities are normalized to the maximal peak. (b) Magnified XRD patterns at angles corresponding to the (100) and (200) lattices of the cubic phase of the fresh (black), the 300 h PT-tested (red), and the 300 h MPPT-tested devices, respectively. Surface scanning electron microscopy (SEM) images of (c) the fresh, (d) the 300 h PT-tested, and (d) the 300 h MPPT-tested. (f) An illustration for an irreversible degradation process based on a charge-state

transition of halide defects occurring during continuous MPPT operation. The neutral interstitial defects are main sources to produce stable chemical compounds, meaning permanent material degradation. (g) An illustration to describe reversible recoveries based on healing of deep-level neutral defects toward shallow-level defects in the PT system. Periodic relaxations of localized charges and ions by reverse pulses trigger reverse charge-state transition, suppressing accumulation of deep-level defects.

4.4 Conclusion

Our PT is the first technique to recover degraded perovskite solar cells by applying a short electrical pulse of RP without any pause of operation. We confirmed that the therapy can not only delay trapped charge driven irreversible degradation, but also effectively heal damaged devices in a reversible way by extracting charges and redistributing ions. Both MA- and FA- based perovskites were clinically tested, showing similar efficacies that led to slowing down their degradation speed as well as recovering degraded power reversibly. Our PT shares its special efficacies with those by self-healing in dark, but appears rapidly just in a few seconds, which makes itself energy-friendly. We elucidated that the PT suppressed the formation of harmful defects and even induced defect healing by mitigating accumulation of charges and ions using in situ PL and PC dynamics. Through this novel operational method, we finally clear gain of harvested energy after 500 h of operation. Its efficacy was also reproducibly confirmed in 500 h long-term test even for different PT conditions. Based on our I-V modeling, trap-assisted recombination could be possibly suppressed by the pulsatile therapy for 500 h of continuous operation, which is well consistent with our PL dynamics experiments. This study proposes unprecedented approach to revive perovskite solar cell devices quickly and lengthen their lifetime with no pause therefore, opens up the possibility of perovskite solar cell commercialization

4.5 References

- [1] A. Kojima, K. Teshima, Y. Shirai, T. Miyasaka, Organometal Halide Perovskites as Visible-Light Sensitizers for Photovoltaic Cells, *J. Am. Chem. Soc.*, 2009, 131, 6050-6051
- [2] M. M. Lee, J. Teuscher, T. Miyasaka, T. N. Murakami, H. J. Snaith, Efficient Hybrid Solar Cells Based on Meso-Superstructured Organometal Halide Perovskites, *Science*, 2012, 338, 643-647.
- [3] H. S. Kim, C. R. Lee, J. H. Im, K. B. Lee, T. Moehl, A. Marchioro, S. J. Moon, R. Humphry-Baker, J. H. Yum, J. E. Moser, M. Gratzel and N. G. Park, Lead Iodide Perovskite Sensitized All-Solid-State Submicron Thin Film Mesoscopic Solar Cell with Efficiency Exceeding 9%, *Sci. Rep.*, 2012, 2, 591.
- [4] J. Burschka, N. Pellet, S. J. Moon, R. Humphry-Baker, P. Gao, M. K. Nazeeruddin and M. Gratzel, Sequential deposition as a route to high-performance perovskite-sensitized solar cells, *Nature*, 2013, 499, 316-319.
- [5] N. J. Jeon, J. H. Noh, Y. C. Kim, W. S. Yang, S. Ryu and S. I. Seok, Solvent engineering for high-performance inorganic–organic hybrid perovskite solar cells, *Nat. Mater.*, 2014, 13, 897-903.
- [6] N. Ahn, D. Y. Son, I. H. Jang, S. M. Kang, M. Choi and N. G. Park, Highly Reproducible Perovskite Solar Cells with Average Efficiency of 18.3% and Best Efficiency of 19.7% Fabricated via Lewis Base

- Adduct of Lead(II) Iodide, *J. Am. Chem. Soc.*, 2015, 137, 8696-8699.
- [7] J. Jeong, M. Kim, J. Seo, H. Lu, P. Ahlawat, A. Mishra, Y. Yang, M. A. Hope, F. T. Eickemeyer, M. Kim, Y. J. Yoon, I. W. Choi, B. P. Darwich, S. J. Choi, Y. Jo, J. H. Lee, B. Walker, S. M. Zakeeruddin, L. Emsley, U. Rothlisberger, A. Hagfeldt, D. S. Kim, M. Gratzel and J. Y. Kim, Pseudo-halide anion engineering for α -FAPbI₃ perovskite solar cells, *Nature*, 2021, 592, 381-385
- [8] J. Yoon, H. Sung, G. Lee, W. Cho, N. Ahn, H. S. Jung and M. Choi, Superflexible, high-efficiency perovskite solar cells utilizing graphene electrodes: towards future foldable power sources, *Energy Environ. Sci.*, 2017, 10, 337-345.
- [9] G. Lee, M.-c. Kim, Y. W. Choi, N. Ahn, J. Jang, J. Yoon, S. M. Kim, J.-G. Lee, D. Kang, H. S. Jung and M. Choi, Ultra-flexible perovskite solar cells with crumpling durability: toward a wearable power source, *Energy Environ. Sci.*, 2019, 12, 3182-3191.
- [10] T. Leijtens, K. A. Bush, R. Prasanna, M. D. McGehee, Opportunities and challenges for tandem solar cells using metal halide perovskite semiconductors, *Nat. Energy*, 2018, 3, 828-838.
- [11] T. H. Han, J. W. Lee, Y. J. Choi, C. Choi, S. Tan, S. J. Lee, Y. Zhao, Y. Huang, D. Kim and Y. Yang, Surface-2D/Bulk-3D Heterophased Perovskite Nanograins for Long-Term-Stable Light-Emitting Diodes, *Adv. Mater.*, 2020, 32, 1905674.
- [12] L. Shen, Y. Fang, D. Wang, Y. Bai, Y. Deng, M. Wang, Y. Lu and J.

- Huang, A Self-Powered, Sub-nanosecond-Response Solution-Processed Hybrid Perovskite Photodetector for Time-Resolved Photoluminescence-Lifetime Detection, *Adv. Mater.*, 2016, 28, 10794-10800.
- [13] L. Dou, Y. M. Yang, J. You, Z. Hong, W. H. Chang, G. Li and Y. Yang, Solution-processed hybrid perovskite photodetectors with high detectivity, *Nat. Commun.*, 2014, 5, 5404.
- [14] J.-P. Correa-Baena, M. Saliba, T. Buonassisi, M. Grätzel, A. Abate, W. Tress and A. Hagfeldt, Promises and challenges of perovskite solar cells, *Science*, 2017, 358, 739-744.
- [15] S. Ma, Y. Bai, H. Wang, H. Zai, J. Wu, L. Li, S. Xiang, N. Liu, L. Liu, C. Zhu, G. Liu, X. Niu, H. Chen, H. Zhou, Y. Li and Q. Chen, *Adv. Energy Mater.*, 2020, 10, 4344-4352
- [16] E. H. Jung, N. J. Jeon, E. Y. Park, C. S. Moon, T. J. Shin, T. Y. Yang, J. H. Noh and J. Seo, Efficient, stable and scalable perovskite solar cells using poly(3-hexylthiophene), *Nature*, 2019, 567, 511-515.
- [17] M. B. Islam, M. Yanagida, Y. Shirai, Y. Nabetani and K. Miyano, Highly stable semi-transparent MAPbI₃ perovskite solar cells with operational output for 4000 h, *Sol. Energy Mater. Solar. Cells*, 2019, 195, 323-329.
- [18] Z. Zhou, Z. Qiang, T. Sakamaki, I. Takei, R. Shang and E. Nakamura, Organic/Inorganic Hybrid p-Type Semiconductor Doping Affords Hole Transporting Layer Free Thin-Film Perovskite Solar Cells with

- High Stability, *ACS Appl. Mater. Interfaces*, 2019, 11, 22603-22611.
- [19] B. Kim, S. I. Seok, Molecular aspects of organic cations affecting the humidity stability of perovskites, *Energy Environ. Sci.*, 2020, 13, 805-820.
- [20] R. Wang, M. Mujahid, Y. Duan, Z. K. Wang, J. Xue and Y. Yang, A Review of Perovskites Solar Cell Stability, *Adv. Funct. Mater.*, 2019, 29, 1808843
- [21] N. Ahn, K. Kwak, M. S. Jang, H. Yoon, B. Y. Lee, J. K. Lee, P. V. Pikhitsa, J. Byun and M. Choi, Trapped charge-driven degradation of perovskite solar cells, *Nat. Commun.*, 2016, 7, 13422.
- [22] Y. Lin, B. Chen, Y. Fang, J. Zhao, C. Bao, Z. Yu, Y. Deng, P. N. Rudd, Y. Yan, Y. Yuan and J. Huang, Excess charge-carrier induced instability of hybrid perovskites, *Nat. Commun.*, 2018, 9, 4981.23.
- [22] Y. Yuan, J. Huang, Ion Migration in Organometal Trihalide Perovskite and Its Impact on Photovoltaic Efficiency and Stability, *Acc. Chem. Res.*, 2016, 49, 286-293.
- [24] D. Di Girolamo, N. Phung, F. U. Kosasih, F. Di Giacomo, F. Matteocci, J. A. Smith, M. A. Flatken, H. Köbler, S. H. Turren Cruz, A. Mattoni, L. Cinà, B. Rech, A. Latini, G. Divitini, C. Ducati, A. Di Carlo, D. Dini and A. Abate, Ion Migration-Induced Amorphization and Phase Segregation as a Degradation Mechanism in Planar Perovskite Solar Cells, *Adv. Energy Mater.*, 2020, 10, 2000310
- [25] S. Ghosh, S. K. Pal, K. J. Karki, T. Pullerits, Ion Migration Heals

- Trapping Centers in CH₃NH₃PbBr₃ Perovskite, *ACS Energy Lett.*, 2017, 2, 2133-2139.
- [26] A. J. Barker, A. Sadhanala, F. Deschler, M. Gandini, S. P. Senanayak, P. M. Pearce, E. Mosconi, A. J. Pearson, Y. Wu, A. R. Srimath Kandada, T. Leijtens, F. De Angelis, S. E. Dutton, A. Petrozza and R. H. Friend, Defect-Assisted Photoinduced Halide Segregation in Mixed-Halide Perovskite Thin Films, *ACS Energy Lett.*, 2017, 2, 1416-1424.
- [27] K. Domanski, B. Roose, T. Matsui, M. Saliba, S.-H. Turren-Cruz, J.-P. Correa-Baena, C. R. Carmona, G. Richardson, J. M. Foster, F. De Angelis, J. M. Ball, A. Petrozza, N. Mine, M. K. Nazeeruddin, W. Tress, M. Grätzel, U. Steiner, A. Hagfeldt and A. Abate, Migration of cations induces reversible performance losses over day/night cycling in perovskite solar cells, *Energy Environ. Sci.*, 2017, 10, 604-613.
- [28] D. J. Slotcavage, H. I. Karunadasa, M. D. McGehee, Light-Induced Phase Segregation in Halide-Perovskite Absorbers, *ACS Energy Lett.*, 2016, 1, 1199-1205.
- [29] S. Tan, I. Yavuz, N. De Marco, T. Huang, S. J. Lee, C. S. Choi, M. Wang, S. Nuryyeva, R. Wang, Y. Zhao, H. C. Wang, T. H. Han, B. Dunn, Y. Huang, J. W. Lee and Y. Yang, Steric Impediment of Ion Migration Contributes to Improved Operational Stability of Perovskite Solar Cells, *Adv. Mater.*, 2020, 32, 1906995.
- [30]. F. Huang, L. Jiang, A. R. Pascoe, Y. Yan, U. Bach, L. Spiccia and Y.-

- B. Cheng, Fatigue behavior of planar CH₃NH₃PbI₃ perovskite solar cells revealed by light on/off diurnal cycling, *Nano Energy*, 2016, 27, 509-514.31.
- [31]. M.-c. Kim, N. Ahn, E. Lim, Y. U. Jin, Peter V. Pikhitsa, J. Heo, S. K. Kim, H. S. Jung and M. Choi, Degradation of CH₃NH₃PbI₃ perovskite materials by localized charges and its polarity dependency, *J. Mater. Chem. A*, 2019, 7, 12075-12085.
- [32] K. Kwak, E. Lim, N. Ahn, J. Heo, K. Bang, S. K. Kim and M. Choi, An atomistic mechanism for the degradation of perovskite solar cells by trapped charge, *Nanoscale*, 2019, 11, 11369-11378.
- [33] N. Aristidou, C. Eames, I. Sanchez-Molina, X. Bu, J. Kosco, M. S. Islam and S. A. Haque, Fast oxygen diffusion and iodide defects mediate oxygen-induced degradation of perovskite solar cells, *Nat. Commun.*, 2017, 8, 15218.
- [34] J. Byeon, J. Kim, J.-Y. Kim, G. Lee, K. Bang, N. Ahn and M. Choi, Charge Transport Layer-Dependent Electronic Band Bending in Perovskite Solar Cells and Its Correlation to Light-Induced Device Degradation, *ACS Energy Lett.*, 2020, 5, 2580-2589.
- [35] W. Nie, J. C. Blancon, A. J. Neukirch, K. Appavoo, H. Tsai, M. Chhowalla, M. A. Alam, M. Y. Sfeir, C. Katan, J. Even, S. Tretiak, J. J. Crochet, G. Gupta and A. D. Mohite, Light-activated photocurrent degradation and self-healing in perovskite solar cells, *Nat. Commun.*, 2016, 7, 11574.

- [36] S. G. Motti, D. Meggiolaro, A. J. Barker, E. Mosconi, C. A. R. Perini, J. M. Ball, M. Gandini, M. Kim, F. De Angelis and A. Petrozza, Controlling competing photochemical reactions stabilizes perovskite solar cells, *Nat. Photonics*, 2019, 13, 532-539.
- [37] T. Duong, H. K. Mulmudi, Y. Wu, X. Fu, H. Shen, J. Peng, N. Wu, H. T. Nguyen, D. Macdonald, M. Lockrey, T. P. White, K. Weber and K. Catchpole, Light and Electrically Induced Phase Segregation and Its Impact on the Stability of Quadruple Cation High Bandgap Perovskite Solar Cells, *ACS. Appl. Mater. Interfaces*, 2017, 9, 26859-26866.
- [38] L. Bertoluzzi, C. C. Boyd, N. Rolston, J. Xu, R. Prasanna, B. C. O'Regan and M. D. McGehee, Mobile Ion Concentration Measurement and Open-Access Band Diagram Simulation Platform for Halide Perovskite Solar Cells, *Joule*, 2020, 4, 109-127
- [39] P. Yadav, D. Prochowicz, E. A. Alharbi, S. M. Zakeeruddin, M. Grätzel, Intrinsic and interfacial kinetics of perovskite solar cells under photo and bias-induced degradation and recovery, *J. Mater. Chem. C.*, 2017, 5, 7799-7805.
- [40] R. G. Balakrishna, S. M. Kobosko, P. V. Kamat, Mixed Halide Perovskite Solar Cells. Consequence of Iodide Treatment on Phase Segregation Recovery, *ACS Energy Lett.*, 2018, 3, 2267-2272.
- [41] M. V. Khenkin, A. K. M, I. Visoly-Fisher, S. Kolusheva, Y. Galagan, F. Di Giacomo, O. Vukovic, B. R. Patil, G. Sherafatipour, V. Turkovic,

- H.-G. Rubahn, M. Madsen, A. V. Mazanik and E. A. Katz, Dynamics of Photoinduced Degradation of Perovskite Photovoltaics: From Reversible to Irreversible Processes, *ACS Appl. Energy Mater.*, 2018, 1, 799-806.
- [42] S. G. Motti, M. Gandini, A. J. Barker, J. M. Ball, A. R. Srimath Kandada and A. Petrozza, Photoinduced Emissive Trap States in Lead Halide Perovskite Semiconductors, *ACS Energy Lett.*, 2016, 1, 726-730.
- [43] D. A. Jacobs, Y. Wu, H. Shen, C. Barugkin, F. J. Beck, T. P. White, K. Weber and K. R. Catchpole, Hysteresis phenomena in perovskite solar cells: the many and varied effects of ionic accumulation, *Phys. Chem. Chem. Phys.*, 2017, 19, 3094-3103.
- [44] C. Eames, J. M. Frost, P. R. Barnes, B. C. O'Regan, A. Walsh and M. S. Islam, Ionic transport in hybrid lead iodide perovskite solar cells, *Nat. Commun.*, 2015, 6, 7497.
- [45] Khanna, V., Das, B. K., Bisht, D., Vandana & Singh, P. K. A three diode model for industrial solar cells and estimation of solar cell parameters using PSO algorithm, *Renew. Energy*, 2015, 78, 105-113.
- [46] Nishioka, K., Sakitani, N., Uraoka, Y. & Fuyuki, Analysis of multicrystalline silicon solar cells by modified 3-diode equivalent circuit model taking leakage current through periphery into consideration, *Sol. Energy Mater. Sol. Cells*, 2007, 91, 1222-1227.
- [47] S. van Reenen, M. Kemerink, H. J. Snaith, Modeling Anomalous

- Hysteresis in Perovskite Solar Cells., *J. Phys. Chem. Lett.*, 2015, 6, 3808-3814.
- [48] C. Li, A. Guerrero, S. Huettner and J. Bisquert, Unravelling the role of vacancies in lead halide perovskite through electrical switching of photoluminescence, *Nat. Commun.*, 2018, 9, 5113.
- [49] D. Meggiolaro, S. G. Motti, E. Mosconi, A. J. Barker, J. Ball, C. Andrea Riccardo Perini, F. Deschler, A. Petrozza and F. De Angelis, Iodine chemistry determines the defect tolerance of lead-halide perovskites, *Energy Environ. Sci.*, 2018, 11, 702-713.
- [50] X. Zhang, M. E. Turiansky, J.-X. Shen, C. G. Van de Walle, Iodine interstitials as a cause of nonradiative recombination in hybrid perovskites, *Phys. Rev. B.*, 2020, 101, 140101.
- [51] L. D. Whalley, R. Crespo-Otero, A. Walsh, H-Center and V-Center Defects in Hybrid Halide Perovskites, *ACS Energy Lett.* 2017, 2, 2713-2714.
- [52] E. Mosconi, D. Meggiolaro, H. J. Snaith, S. D. Stranks, F. De Angelis, Light-induced annihilation of Frenkel defects in organo-lead halide perovskites, *Energy Environ. Sci.*, 2016, 9, 3180-3187.
- [53] A. Buin, P. Pietsch, J. Xu, O. Voznyy, A. H. Ip, R. Comin and E. H. Sargent, Materials Processing Routes to Trap-Free Halide Perovskites, *Nano Lett.*, 2014, 14, 6281-6286.
- [54] A. R. Bowring, L. Bertoluzzi, B. C. O'Regan and M. D. McGehee, Reverse Bias Behavior of Halide Perovskite Solar Cells, *Adv. Energy*

Mater., 2018, 8,1702365

- [55] L. Bertoluzzi, J. B. Patel, K. A. Bush, C. C. Boyd, R. A. Kerner, B. C. O'Regan and M. D. McGehee, Incorporating Electrochemical Halide Oxidation into Drift-Diffusion Models to Explain Performance Losses in Perovskite Solar Cells under Prolonged Reverse Bias, *Adv. Energy Mater.*, 2021, 11, 2002614
- [56] S. Wang, Y. Jiang, Emilio J. Juarez-Perez, Luis K. Ono and Y. Qi, Accelerated degradation of methylammonium lead iodide perovskites induced by exposure to iodine vapour, *Nat. Energy* 2016, 2,16195
- [57] F. Fu, S. Pisoni, Q. Jeangros, J. Sastre-Pellicer, M. Kawecki, A. Paracchino, T. Moser, J. Werner, C. Andres, L. Duchêne, P. Fiala, M. Rawlence, S. Nicolay, C. Ballif, A. N. Tiwari and S. Buecheler, I₂ vapor-induced degradation of formamidinium lead iodide based perovskite solar cells under heat–light soaking conditions, *Energy Environ. Sci.*, 2019, 12, 3074-3088.

Appendix A.

NOTE 1. Calculation of total gain

Each cell has slightly different initial power conversion efficiency. To fairly evaluate improvement of total energy harvested from each cell, normalized power of each cell is used. The normalized power P_{norm} is calculated by

$$P_{\text{norm}}(t) = \frac{P(t)}{P(0)}$$

where $P(t)$ is an electrical power harvested by a device at operation time t and $P(0)$ is an initial electrical power.

We calculated integration of normalized power over time to estimate normalized total energy during total operation time (including pulse period) as the following equation.

$$E_{\text{norm}}(T) = \int_0^T P_{\text{norm}}(t) dt$$

To calculate how much the normalized total energy of the cell working by pulsatile therapy has improved over the normalized total energy of the MPPT case, we defined total gain (G) as the following equation.

$$G(\%) = 100 * (E_{\text{norm,PT}} - E_{\text{norm,MPPT}}) / E_{\text{norm,MPPT}}$$

When $G(\%)$ is equal to zero, normalized total energy of the therapy is said to be the same as that of the MPPT. The time dependent total gain

should be negative at early times due to the power consumptions needed to apply reverse biases in our PT, but later become positive since our PT stabilizes the device and even restores the degraded performance causing the normalized powers to become larger than those of MPPT.

In addition to evaluate stability enhancement in terms of normalized power (P_{norm}), relative increase of normalized power (η) is calculated by

$$\eta = 100 * \left(\frac{P_{\text{norm}}(t)_{PT}}{P_{\text{norm}}(t)_{MPPT}} - 1 \right)$$

Acknowledgement

This work was supported by the Global Frontier R&D Program of the Center for Multiscale Energy Systems funded by the National Research Foundation under the Ministry of Education, Science and Technology, Korea.

The research data of chapter 2 are the result on the collaboration with Jutae Kim. In addition, the research data have been reported in *ACS Energy Letters* (*ACS Energy Lett.* 2020, 5, 8, 2580-2589). The research data of Chapter 3 are the result on the collaboration with Seongho Cho (Seoul National University), therefore it can include similar contents in dissertation of Seongho Cho. The results of chapter 3 have been published in *Advance Energy Materials* (*Adv. Energy Mater.* 2021, 11, 2100555). The research data of chapter 4 are the results on the collaboration with Kiwan Jeong and Dr. Namyong Ahn. In addition, the research results in this chapter will be published in the academic journals.

I would like to thank my supervisor Prof. Mansoo Choi, co-advisor Prof. Yunseog Lee, for their warm encouragement and helpful advices. I would like to especially thank Mincheol Park, Kiwan jeong and Unsoo Kim. I am also grateful to Dr. Jun Xi and Namyong Ahn. I also appreciate all of my laboratory members for their kind support, assistance and many helps.

초 록

유기-무기 할로겐화 납 페로브스카이트 태양전지는 10년이라는 짧은 시간에 25% 이상의 전력 변환 효율에 도달했으며 차세대 태양전지로 전 세계의 주목을 받고 있다. 그러나 페로브스카이트 태양전지는 장기적인 구동 안정성과 관련하여 많은 문제점이 있다. 이온 결정으로 알려진 할로겐화납 페로브스카이트는 유기물과 무기물의 결합이 약해 빛과 함께 수분, 산소에 취약하다. 수분과 산소가 태양전지 소자에 노출되는 것을 방지하기 위해 다양한 봉지 기술이 사용되었다. 하지만 빛이 조사되는 조건에서 높은 농도의 전하들이 발생하고, 봉지 기술이 적용된 소자도 빛을 조사하는 조건에서 급속한 열화 현상을 보인다. 이는 전하 축적과 전하에 의한 결함 변이와 같은 내부 열화 원인들에 의한 비가역적인 열화를 나타낸다. 페로브스카이트 태양전지의 안정적인 구동을 위해서는 내부 열화 요인에 의한 열화 메커니즘의 기본 원리를 이해하고, 열화 원리에 대한 이해를 바탕으로 페로브스카이트 태양전지의 안정성을 높이는 방안을 고안해야 한다. 본 학위 논문은 페로브스카이트 태양전지 내부에 발생하는 전하에 의한 열화 메커니즘을 규명하고, 전하 축적 및 깊은 준위 결함 형성을 억제하여 페로브스카이트 태양전지의 안정성을 향상시키는 새로운 작동 기술에 관하여 기술하는 것을 목적으로 한다.

첫째, 전하 축적과 태양전지 소자 열화 사이의 상관관계를 조사했다. 상관관계를 조사하기 위해 서로 다른 전자수송층을 갖는 페로브스카이트 태양전지를 사용하였다. 페로브스카이트 태양전지는 전자 수송층에 따라 특정 계면에서 우세한 p-n 접합 현상(높은 정도의 밴드 굽힘)이 발생하고, 전하 축적은 우세 접합에서 위치하면서 해당 우세 접합에서 소자 열화가 시작되었다. 전자 빔 유도 전류 측정 및 켈빈 프로브 힘 현미경을 사용하여 전자 수송층에 따라 달라지는 진공 준위의 형태, 전기장 및 전하 밀도 분포의 위치를 확인했다. 태양전지 소자에 축적된 전하량을 측정한 결과, 전하 축적이 가장 적은 소자가 더

좋은 안정성을 보였다. 성능 저하가 일어난 페로브스카이트 태양전지에서 시간에 따른 분해 과정의 확인한 결과, 우세 p-n 접합에 존재하는 높은 농도의 단일 부호를 가진 전하가 분해를 유도한다는 것을 보여주었다. 이 연구를 통해서 우세 p-n 접합에 위치한 축적된 전하가 태양전지 소자 성능 저하에 중요한 역할을 한다는 것을 최초로 밝혀냈다.

둘째, 페로브스카이트 격자에서의 약한 이온 결합 특성은 낮은 결합 형성 에너지를 유도해 페로브스카이트에서 결합의 형성 가능성을 높인다. 이온성 결합의 전자 상태는 높은 전하 농도 조건(빛 조사)에서 전하 상태 변이를 통해서 변할 수 있다. 하지만, 전하의 유도 결합 변이로 인한 페로브스카이트 분해 메커니즘 여전히 파악되지 않고 있다. 이 파트에서는 외부적 요인(물, 산소)가 없는 조건에서, 서로 다른 내부 고유 결합을 가지는 페로브스카이트 태양전지의 빛에 의한 성능 저하 패턴을 연구하였다. 자체 도핑 효과를 조절하기 위해 요오드화납(PbI_2)의 농도가 다른 전구체를 이용하여 제작되었고 이로 인해 서로 다른 페르미 준위를 갖는 페로브스카이트 필름을 생성하였다. 빛에 오랜 시간 노출된 납(Pb)이 풍부한 페로브스카이트 필름에서 페로브스카이트 격자에서의 변형을 완화와 새로운 결합 형성을 의미하는 비방사 재결합의 증가가 확인되었고, 이는 납(Pb)이 많은 소자에서 새로운 결합 상태의 형성을 의미한다. 열 어드미턴스 분광법 측정을 통해서 납(Pb)이 많은 태양전지 소자에서 깊은 에너지 준위를 갖는 트랩으로의 변이가 비가역적인 열화를 초래하고 서로 다른 조건에서 제작된 페로브스카이트 태양전지 간의 빛에 의한 노화 패턴의 차이와 관련될 수 있음을 보여주었다. 이 연구를 통해서 결정립계와 계면 근처에서 비화학량론에 의해 발생하는 깊은 준위 결합의 패시베이션이 장기적 안정성을 갖는 페로브스카이트 태양전지에 중요하다는 것을 시사하였다.

셋째, 축적된 전하와 이온 결합은 모두 페로브스카이트 태양전지의 열화의 원인으로 보고되었다. 펄스 치료 요법은 최대전력점 추적 동안 전하와 이온 결합의 축적을 모두 해결하여 태양전지 소자의 구동 수명을 늘리기 위해 개발되었다. 이 기술을 통해서 소자 구동에 있어 중단 없이

매우 짧은 시간 동안 주기적으로 역 바이어스가 소자에 인가되어 태양전지 소자를 안정하게 구동하도록 만든다. 펄스 치료 요법의 효능은 최대전력점 추적 구동 중에 비가역적 성능 저하를 지연시킬 뿐만 아니라 저하된 광 전류를 복구하는 것이다. 최대전력점 추적 구동 중에 태양전지 소자에서의 결함 형성과 펄스 치료 요법을 통한 결함 치유에 관하여 정확한 메커니즘 분석을 위해 태양전지 소자에서의 광 발광 및 광 전류를 동시 측정을 하였다. 우리는 유해한 깊은 에너지 준위를 갖는 결함이 역으로의 결함 상태 변이를 통해 치료될 수 있는 펄스 치료 요법의 통합 메커니즘을 제시하였다. 500시간의 장기 테스트에서 우리는 소자안정성과 총수확에너지의 뚜렷한 향상을 확인하였다. 페로브스카이트 태양전지 장치를 신속하게 치유하고, 작동을 중지하지 않고도 태양전지의 소자 수명을 연장할 수 있는 전례 없는 기술적 접근 방식을 제안하였다. 이 기술을 통해 페로브스카이트 태양전지 상용화 가능성을 최대한 높일 수 있을 것이라 전망한다.

주요어 : 페로브스카이트 태양전지, 열화, 전하 축적, 결함, 펄스 치료 요법, 결함 치료,

학 번 : 2015-22699

LIST of Publication.

- [1] Namyoung Ahn†, Kwisung Kwak†, Min Seok Jang, Heetae Yoon, Byung Yang Lee, Jong-Kwon Lee, Peter V. Pikhitsa, **Junseop Byun** and Mansoo Choi “Trapped charge-driven degradation of perovskite solar cells” *Nature Communications* (2016)
- [2] Il Jeon†, Jungjin Yoon†, Unsoo Kim†, Changsoo Lee, Rong Xiang, Ahmed Shawky, Jun Xi, **Junseop Byeon**, Hyuck Mo Lee, Mansoo Choi*, Shigeo Maruyam* and Yutaka Matsuo* “High-Performance Solution-Processed Double-Walled Carbon Nanotube Transparent Electrode for Perovskite Solar Cells” *Advanced Energy Materials* (2019)
- [3] Jun Xi, Chengcheng Piao, **Junseop Byeon**, Jungjin Yoon, Zhaoxin Wu*, Mansoo Choi* “Rational Core–Shell Design of Open Air Low Temperature In Situ Processable CsPbI₃ Quasi-Nanocrystals for Stabilized p-i-n Solar Cells” *Advanced Energy Materials* (2019)
- [4] **Junseop Byeon**†, Jutae Kim†, Ji-Young Kim, Gunhee Lee, Kijoon Bang, Namyoung Ahn*, and Mansoo Choi* Charge Transport Layer-Dependent Electronic Band Bending in Perovskite Solar Cells and Its Correlation to Light-Induced Device Degradation, *ACS Energy Letters* (2020)
- [5] Jungjin Yoon†, Unsoo Kim, Yongseok Yoo, **Junseop Byeon**, Seoung-Ki Lee, Jeong-Seok Nam, Kyusun Kim, Qiang Zhang, Esko I. Kauppinen, Shigeo Maruyama*, Phillip Lee*, Il Jeon* “Foldable Perovskite Solar Cells Using Carbon Nanotube-Embedded Ultrathin Polyimide

Conductor” *Advanced Science* (2021)

[6] Seong Ho Cho†, **Junseop Byeon**†, Kiwan Jeong, Jiseon Hwang, Hyunjoon Lee, Jihun Jang, Jieun Lee, Taehoon Kim, Kihwan Kim, Mansoo* Choi and Yun Seog Lee* “Investigation of Defect-Tolerant Perovskite Solar Cells with Long-Term Stability via Controlling the Self-Doping Effect” *Advanced Energy Materials* (2021)

[7] Jun Xi†, **Junseop Byeon**†, Unsoo Kim†, Kijoon Bang†, Gi Rim Han, Ji-Young Kim, Jungjin Yoon, Hua Dong, Zhaoxin Wu, Giorgio Divitini, Kai Xi, Jinwoo Park, Tae-Woo Lee, Seong Keun Kim, Mansoo Choi and Jong Woo Lee. Abnormal spatial heterogeneity governing the charge-carrier mechanism in efficient Ruddlesden–Popper perovskite solar cells” *Energy Environmental Science* (2021)

[8] Kiwan jeong†, **Junseop Byeon**†, Jihun Jang, Namyung Ahn*, and Mansoo Choi*. Pulsatile therapy for perovskite solar cells” (will be published in academic journal)